UC Davis

UC Davis Electronic Theses and Dissertations

Title

NMR and NQR Studies of the Normal and Superconducting States of LaNiGa2

Permalink

https://escholarship.org/uc/item/52c1k9kx

ISBN

9798193265450

Author

Sherpa, Phurba

Publication Date

2026-09-08

Peer reviewed|Thesis/dissertation

eScholarship.org Powered by the California Digital Library
University of California

NMR and NQR Studies of the Normal and Superconducting States of $LaNiGa_2$

By

PHURBA T. SHERPA
DISSERTATION

Submitted in partial satisfaction of the requirements for the degree of

DOCTOR OF PHILOSOPHY

in

Physics

in the

OFFICE OF GRADUATE STUDIES

of the

UNIVERSITY OF CALIFORNIA

DAVIS

Approved:

Nicholas Curro, Chair

Valentin Taufour

Marina Radulaski

Committee in Charge 2026

© Phurba T. Sherpa, 2026. All rights reserved.

This work is dedicated to my parents Danu and Nima,
my brother Namgyal,
my wife Lakpa,
and to the rest of my family.

Contents

1 Introduction **1**

2 NMR Fundamentals **3**

2.1 Nuclear Spins in a Magnetic Field 3

2.2 Interactions 6

2.2.1 Hyperfine interactions between Nuclear spins and electrons 6

2.2.2 Magnetic interactions between Nuclear Spins 9

2.2.3 Electric quadrupole interactions 10

2.2.4 Nuclear Quadrupole Resonance (NQR) 12

2.2.5 Nuclear Magnetic Resonance (NMR) 13

2.3 Relaxation 16

2.3.1 Spin-Lattice Relaxation in Metals 20

2.3.2 Spin-Lattice Relaxation Due to Fluctuating Fields 23

2.3.3 Spin-Spin Relaxation 24

2.4 Measurements 25

2.4.1 Free Induction Decay (FID) 25

2.4.2 Spin-Echo 28

2.4.3 Measuring T_2 29

2.4.4 Measuring T_1 30

3 Techniques and Instrumentation **32**

3.1 NMR Resonance circuit . . . 32

3.2 Magnets . . . 35

3.3 Cryogenics . . . 36

3.3.1 Liquid Helium Cryostats . . . 36

3.3.2 Oxford Liquid Dilution Refrigerator . . . 38

3.4 Samples . . . 42

3.4.1 $LaNiGa_2$ . . . 42

3.5 Challenges and Solutions . . . 43

3.5.1 Temperature . . . 43

3.5.2 Signal Loss . . . 45

4 Triplet Superconductors **48**

4.1 General Background . . . 48

4.2 Introduction to $LaNiGa_2$ . . . 50

5 NMR in the Superconducting State **52**

5.1 Knight Shift . . . 52

5.1.1 Diamagnetic Shielding . . . 55

5.2 Spin-Lattice Relaxation Rate . . . 56

5.2.1 BCS model . . . 56

5.2.2 non-BCS superconductors . . . 60

5.2.3 INT Triplet Model . . . 61

5.2.4 Two-Gap Singlet Model . . . 64

6 NMR and NQR in the Normal State of $LaNiGa_2$ **65**

6.1 ^{139}La NMR Spectrum . . . 66

6.2 ^{69}Ga NMR Spectrum . . . 67
6.3 NQR Spectrum . . . 69
6.4 Electric Field Gradient . . . 70
6.5 Stoner enhancement factor . . . 73
6.6 Knight Shift and T_1 . . . 75
6.7 Korringa Relation . . . 76
6.8 Summary . . . 78

7 NQR in the Superconducting State of $LaNiGa_2$ **80**
7.1 T_1 . . . 81
7.2 Hebel-Slichter Peak Discussion . . . 84
7.3 Summary . . . 87

8 Conclusions **89**

A Appendix A **92**

B Appendix B **94**

C Appendix C **96**
C.1 Coherence Factors . . . 96
C.1.1 $\boldsymbol{j = z}$ . . . 101
C.1.2 $\boldsymbol{j = x}$ . . . 102
C.1.3 **Relaxation Rate** . . . 104
C.2 Variation with nuclear frequency . . . 105
C.3 **d**-vector of form $(r, i, 0)$ . . . 107

Abstract

$LaNiGa_2$ presents an intriguing case of superconductivity in which the symmetry of the superconducting state remains under debate. It is an intermetallic superconductor with a relatively low transition temperature of $T_c \approx 2.1$ K. muon spin resonance (μSR) measurements have reported evidence for spontaneous internal magnetic fields below T_c, suggesting possible time-reversal symmetry breaking (TRSB) in the superconducting state [25]. An unconventional fully gapped triplet pairing state was subsequently proposed [80].

In this work, we present comprehensive nuclear magnetic resonance (NMR) and nuclear quadrupole resonance (NQR) measurements of $LaNiGa_2$ in both the normal and superconducting states. NMR and NQR measurements of $LaNiGa_2$ reveal no evidence for strong electronic correlations or magnetic fluctuations in the normal state. The Korringa ratios at both the ^{139}La and ^{69}Ga sites remain nearly temperature independent and close to the uncorrelated value of unity, indicating weak magnetic fluctuations. The experimentally determined electric field gradient (EFG) also agrees closely with density functional theory (DFT) calculations performed without explicitly including Coulomb interactions, suggesting that the electronic structure is well described without strong electronic correlations. Together, the nearly temperature-independent susceptibility, Korringa ratios near unity, and agreement between experimental and calculated EFGs provide no evidence for significant Stoner enhancement or strong low-energy spin fluctuations. These results suggest that superconductivity in $LaNiGa_2$ is unlikely to originate from the correlation driven mechanisms commonly invoked in unconventional superconductors.

Zero-field NQR T_1^{-1} measurements place strong constraints on the superconducting pairing state of $LaNiGa_2$. The proposed internally antisymmetric, non-unitary, triplet (INT) model can only reproduce the observed temperature dependence of T_1^{-1} when the two triplet gaps have the same magnitude. In this limiting case, however, the state becomes unitary and does

not break time reversal symmetry. Therefore, the INT model cannot simultaneously account for the NQR data and the proposed non-unitary TRSB state. In contrast, the data are well described by a two-band Bardeen–Cooper–Schrieffer (BCS) model with spin singlet pairing and different gap magnitudes. This provides a natural description of the observed relaxation behavior without requiring a triplet order parameter. While the NQR measurements do not exclude more complex unconventional pairing states, they indicate that the experimental T_1^{-1} data are more naturally consistent with a multiband singlet state and challenge the proposed interpretation of $LaNiGa_2$ as a non-unitary TRSB triplet superconductor.

Acknowledgments

I would first and foremost like to thank my advisor at UC Davis Nick Curro for his unyielding patience, guidance, and all of the opportunities he provided during my PhD. I will forever be grateful to you for believing in me and having me in your group.

Secondly, I would like to thank my advisor at Los Alamos National Laboratory Michihiro Hirata for supporting me and teaching me the best practices as an experimentalist. Thank you for broadening my understanding of NMR and how it fits in the wider context of condensed matter physics.

I would also like to thank Igor Vinograd whose guidance was essential when I first joined the group. Thank you for getting me started in the lab and all of your jokes that brightened my day during the pandemic.

A special thanks to Peter Klavins whose tireless effort keeps our and many other labs at UC Davis working. Thank you for always being there when we needed you.

Thank you to Adam Dioguardi and Riku Yamamoto for sharing their expertise and helping me run and plan my experiments at LANL.

I would also like to thank Stuart Brown for teaching me how to run and operate the dilution refrigerator. I also really enjoyed our trip to the NHMFL in Tallahassee and am very thankful for the guidance you provided there.

I would also like to thank Filip Ronning for giving me the opportunity to work at LANL and for his patience and persistence in pushing my experiments forward during my time there.

Thank you to the rest of the MPA-Q group at LANL, Priscilla, Sean, Roman, Joe, Mike, Ajeesh, Mitchell, Clemont, and Matthew. It was a pleasure working with all of you and I hope our paths will cross again soon.

Thank you to Valentin Taufour and his lab group for providing us with the samples we

used in my measurements. Especially, Yunshu Shi and Jackson Badger who grew all of the samples I used.

Thank you to Rahul Hingorani and Professor Rajiv Singh who helped with the theoretical support for my research. I will always be thankful to Rahul for the extra time he took to walk me through his theoretical work.

To my lab mates, Cameron, Chris, Rashad, Walter, Zepplin, Yu-Hsuan, Victoria, Alba, and Charlie: Thank you all for your help and company during my years at Davis. You were the best group mates I could have asked for. I really enjoyed our time together and you will be dearly missed. Also, thank you to our undergraduates in the group, especially Liz who was so helpful during my final months at Davis. Thank you also to Emi who brought a bright spark to the lab during my final summer.

To my professors at UC Davis, Rena Zeive, Rajiv Singh, Warren Pickett, Gergely Zimanyi, Nemanja Kaloper, Veronika Hubeny, Daniel Cebra, Daniel Cox and Mukund Rangamani: Thank you for deepening my understanding of physics and teaching us through the pandemic.

To my fellow grad students not yet mentioned: Bob, Jamie, Spiegel, Fiona, Hyun-Soo, Jean, Joe, Rodrigo (Brazil and Peru), Zack, Matt, Priti, Bobby, Erin, Arsalan, Lotte, Ian, Samantha, and Can: Thank you for making Davis and the physics department feel like home. I will never forget all of the fun we had together and I'll look forward to more when we see each other again. And to my best friends from childhood, Christian, Nate, and Chancey: You guys are always there for me and I am eternally grateful that life brought us together.

To my Mom and Dad: Thank you for your unrelenting love and support throughout the years. Thank you for teaching me not only what to do but how to be. I love you both so much. I owe everything I am today to you and I will do my best to carry on your good will. To my little brother Namgyal, I rest easy knowing our parents have such a good son at home and I love you dearly.

To my loving wife Lakpa: Thank you for your love and support. I didn't know I was

looking, but I'm so glad I found you and I thank God every day that we met. I love you so much and I can't wait to see where life takes us.

Chapter 1

Introduction

Unconventional superconductivity is generally associated with electronic interactions that extend beyond the conventional electron-phonon mechanism described by BCS theory. In many unconventional superconductors, strong electronic interactions are present, and a magnetically ordered phase in the normal state competes with the superconducting phase [44, 52, 56, 60]. Spin fluctuations associated with these interactions are therefore widely considered to play an important role in determining the pairing symmetry and superconducting gap structure in a number of strongly correlated materials. As a result of these interactions, the superconducting state can exhibit unconventional pairing symmetries such as spin-triplet pairing, multicomponent order parameters, and broken time-reversal symmetry.

$LaNiGa_2$ presents an interesting case in which the origin and symmetry of the superconducting state remain under debate. $LaNiGa_2$ is an intermetallic superconductor with a relatively low transition temperature ($T_c \approx 2.1$ K). muon spin resonance (μSR) measurements have reported evidence for spontaneous internal magnetic fields below superconducting transition temperature T_c, suggesting possible time-reversal symmetry breaking in the superconducting state [25]. This observation is particularly notable because the conventional spin-singlet s-wave state is time-reversal symmetric and does not naturally produce spontaneous internal

fields. Motivated by the μSR results and the multiband electronic structure of $LaNiGa_2$, an unconventional fully gapped triplet state was subsequently proposed [80]. The interband non-unitary triplet (INT) state involves pairing between electrons residing on different electronic bands, where the superconducting order parameter can be antisymmetric in the band degree of freedom while remaining consistent with the required fermionic antisymmetry. The resulting non-unitary triplet state can support broken time-reversal symmetry while remaining fully-gapped. The proposed INT state is made possible by the multiband and topological characteristics of the electronic structure of $LaNiGa_2$. Band structure calculations indicate the presence of band degeneracies near the Fermi level which provide the electronic structure necessary for the proposed interband pairing mechanism [2, 80].

Establishing whether this proposed pairing state is realized in $LaNiGa_2$ requires experimental probes that are sensitive to magnetic fluctuations and the spin structure of the Cooper pairs. Nuclear magnetic resonance (NMR) and nuclear quadrupole resonance (NQR) experiments are perfectly suited for this as they are local probes of the electronic environment which use low-energy excitations that do not significantly perturb the electronic state.

In this work, we report NMR and NQR measurements of $LaNiGa_2$ in both the normal and superconducting states. Measurements of the normal state Knight shift, spin-lattice relaxation rate, and Korringa ratio allow us to investigate the strength of the electronic correlations and magnetic fluctuations. The NQR measurements in the superconducting state provide information about the temperature dependence of the quasiparticle excitation spectrum and allow us to test the proposed INT pairing state against the experimental relaxation data. Using these measurements, we assess both the normal state electronic correlations and the superconducting pairing state of $LaNiGa_2$. Our results provide important constraints on the proposed triplet TRSB state and lay the foundation for possible future work to better understand the superconducting state.

Chapter 2

NMR Fundamentals

2.1 Nuclear Spins in a Magnetic Field

Isotopes of elements on the periodic table, typically ones with an odd number of nucleons, will have some net spin $\vec{I}$ which results in a nuclear magnetic moment $\vec{\mu}$ given by:

$$\vec{\mu} = \frac{g\mu_N}{\hbar}\vec{I} = \gamma\hbar\vec{I} \tag{2.1}$$

Here g is the effective g-factor of the nucleus [18], $\mu_N = 5.05 \times 10^{-27} A \cdot m^2$ is the nuclear magneton, and $\hbar$ is the Planck constant. These prefactors are combined to give the gyromagnetic ratio γ which is specific to a given nucleus.

The nuclear magnetic moment $\vec{\mu}$ couples to an external field $\vec{H_0}$ via the Zeeman interaction:

$$H_Z = -\vec{\mu} \cdot \vec{H_0} \tag{2.2}$$

We assume the z-direction for the external field so $\vec{H_0} = H_0\hat{z}$. For quantum mechanics, we then replace $\vec{I}$ with the operator $\hat{I}$ with eigenvalues of $\hbar m$. Combining these results in the

following:

$$H_Z = -\gamma \vec{H}_0 \cdot \hat{I} = -\gamma H_0 \hat{I}_z \tag{2.3}$$

giving $(2I + 1)$ evenly spaced nuclear spin energy levels:

$$E_m = -\gamma H_0 \langle I, m| \hat{I}_z |I, m\rangle = -\gamma \hbar m H_o \tag{2.4}$$

where

$$m = -I, -I + 1, ..., I - 1, I \tag{2.5}$$

The matrix elements for the operator $\hat{I}_z$ are nonzero between states $|I, m\rangle$ and $|I, m'\rangle$ only when m' = m $\pm$ 1. The quantization of the energy levels means that the only transitions allowed between states are ones where $\Delta m = \pm 1$. The difference in energy between these adjacent states is $\Delta E = \gamma \hbar H_0$, more commonly written as $\hbar \omega_L$ with

$$\omega_L = \gamma H_0 \tag{2.6}$$

being the Larmor frequency at which the nucleus precesses about the external field H_0.
So far we have seen the interaction of a single nuclear spin with a magnetic field. However, in typical NMR experiments we are dealing with on the order of 10^{16} nuclear spins to have sufficient signal to noise. We therefore need a thermodynamic treatment of our nuclear spin system. At equilibrium, the populations of the nuclear spin states are given by the Boltz-

mann distribution.

$$P(m) \propto \exp\left(\frac{-E_m}{k_B T}\right) \tag{2.7}$$

The unequal population of nuclear spin states results in the system having some net magnetization M_Z. The magnetization will be proportional to the expectation value of $\left\langle \hat{I}_z \middle| \hat{I}_z \right\rangle$ for our population of spins:

$$M_Z = N\gamma \langle I_z | I_z \rangle = N\gamma \frac{\sum_{m=-I}^{m=I} \hbar m P(m)}{\sum_{m=-I}^{m=I} P(m)} = N\gamma \frac{\sum_{m=-I}^{m=I} \hbar m \exp\left(\frac{-E_m}{k_B T}\right)}{\sum_{m=-I}^{m=I} \exp\left(\frac{-E_m}{k_B T}\right)} \tag{2.8}$$

$E_m/k_B T$ is very small so the Boltzmann exponential can be expanded and approximated to linear order giving us:

$$M_Z \approx \frac{N\gamma^2 \hbar^2 I(I+1)}{3k_B T} H_0 = \chi_n H_0 \tag{2.9}$$

where N is the density of the nuclear spins and χ_n is the static nuclear spin susceptibility. Since the signal measured is directly proportional to the magnetization, equation 2.9 reveals some critical aspects to running good NMR experiments. Namely, the increase in magnetization M_Z with the increase in the number of nuclear spins N, the strength of the external field H_0, and decrease in temperature. The inclusion of gyromagnetic ratio γ also gives an indication that some nuclei are easier to detect than others. Furthermore, γ contains the nuclear magneton which is much smaller than the Bohr magneton for an electron, meaning the static spin susceptibility χ_n of the nucleus is much smaller than that of an electron χ_e. The nuclear spin states therefore, can be manipulated without disturbing the electronic spin

states which we are trying to study making NMR an excellent probe of electronic states.

2.2 Interactions

Changes in nuclear magnetization M_Z measured in NMR experiments are determined by the interactions of the nuclear spin system with its local environment. In addition to the coupling with the external magnetic field discussed so far we need to consider the interactions with other nuclei and electrons in the system. The combined Hamiltonian has the following form:

$$H = H_z + H_{nn} + H_{ne} + H_q \tag{2.10}$$

H_z is the Zeeman interaction with the external field. H_{nn} describes the dipolar interactions between nuclei in the system. H_{ne} gives the hyperfine interaction between the nuclei and electrons. Finally, H_q is the interaction between the quadrupole moment of the nuclei and the local electric field gradient.

2.2.1 Hyperfine interactions between Nuclear spins and electrons

In condensed matter research we are primarily concerned with the behavior of electrons, making the hyperfine interaction between nuclei and electrons of particular interest in solid-state NMR experiments. The hyperfine interaction typically leads the nuclei in the system to see a slightly different field compared to the static external field H_0. We can write the Zeeman and hyperfine Hamiltonian together as:

$$H_Z + H_{ne} = -\hbar\gamma\vec{I}(1 + \mathbf{K})\vec{H}_0 \tag{2.11}$$

where **K** is the Knight shift tensor which gives the deviation from the expected Larmor resonance frequency for a given nucleus in the field H_0 without hyperfine interactions. The Knight shift consists of three nuclear electron interactions:

$$K = K_{dia} + K_o + K_s \tag{2.12}$$

K_{dia} is given by the interaction of the nuclei with the diamagnetism of the inner electron shells and Landau diamagnetism of the conduction electrons, but the effect is very small and is neglected in typical solid-state NMR experiments where such small shifts are masked by the other two components K_o and K_s. K_o is the shift due to the interaction of the nuclei and the orbital moment of the electrons, and K_s is the shift due to the spins of the electrons. In practice, these are difficult to separate and are treated together as the K_{hf} which is the hyperfine interaction between the nuclei and the electrons. The hyperfine Hamiltonian is given by the following:

$$H_{hf} = \gamma_n \gamma_e \hbar^2 \vec{I} \cdot \left[\left(3\frac{(\vec{S}\cdot\vec{r})\cdot\vec{r}}{r^5} - \frac{\vec{S}}{r^3} \right) + \frac{8\pi}{3}\vec{S}\delta(\vec{r}) + \frac{\vec{L}}{r^3} \right] \tag{2.13}$$

where $\vec{I}$ is the nuclear spin and $\vec{S}$ and $\vec{L}$ are the spin and orbital angular momentum of the electron with $\vec{r}$ being the distance vector between them. The final term in equation 2.13 gives the interaction between the spin of the nucleus and the orbital moment of the electron, giving us the orbital component of the Knight shift which comes from the angular momentum of the electrons creating a loop of moving charge, resulting in an orbital moment. The net angular momentum for electrons in the inner orbitals as well as for conduction electrons in transition metals is zero. However, application of an external field can cause a mixing of some of the electrons into higher states, allowing for a net moment that results in the orbital

component of the Knight shift. This effect is known as Van Vleck paramagnetism where:

$$K_{orb} = 2\left\langle r^{-3}\right\rangle \chi_V \tag{2.14}$$

where χ_V is the Van Vleck paramagnetic susceptibility and typically temperature-independent. Therefore, the K_{orb} is also generally temperature-independent.

The first of the two remaining terms in equation 2.13 describes the spin component of the Knight shift. The first term in parentheses is the dipolar interaction between the nuclear and electron spins. Electrons in filled s orbitals do not contribute to this because their wavefunctions are spherically symmetric. Unpaired electrons in s orbitals, however, can have a dipolar coupling with the nucleus, giving us the second term which is known as the Fermi-contact interaction because it is proportional to the probability of finding the electron at the nuclear site. If the orbitals in the material hybridize, a nucleus can have a hyperfine coupling to an electron in a distant orbital with strength comparable to the Fermi contact interaction [51]. The interaction of the nucleus and electrons in distant orbitals mediated by the hybridization of orbitals is also known as the transferred hyperfine coupling and is essential for analyzing heavy fermion systems. Unpaired electrons can also cause a polarization of electrons in filled inner shells which also couples to the nuclear moment. The contributions from the Fermi contact and polarization of inner orbitals are not distinguishable and isotropic, while the dipolar interaction depends on the orientation of the external field. These interactions can be combined to give us the spin component of the Hamiltonian:

$$H_s = -\vec{I}^i A^{ij} \vec{S}^j \tag{2.15}$$

where $\vec{I}^i$ is a nuclear spin at site i and $\vec{S}^j$ is an electron spin at site j and A^{ij} is the hyperfine coupling tensor between them accounting for all of the spin interactions described. The spin

component of the Knight Shift is proportional to the static spin susceptibility of the electrons:

$$K_s = \frac{A^{ij}}{g_e \mu_B \gamma \hbar} \chi_s \tag{2.16}$$

where χ_s is the static spin susceptibility of the electrons and g_e is the g-factor of the electron. χ_s includes the Pauli spin susceptibility of the conduction electrons χ_P and the paramagnetic susceptibility of the localized electrons χ_{para} given by

$$\chi_P = \frac{M}{H_0} = \frac{3N\mu_B^2}{2k_B T_f} \tag{2.17}$$

$$\chi_{para} = \frac{C}{T} = \frac{N'\mu_B^2 p^2}{3k_b T} \tag{2.18}$$

2.2.2 Magnetic interactions between Nuclear Spins

Interactions between nuclear spins in a system H_{nn} consist of the direct dipolar coupling between nuclei and indirect coupling between nuclei mediated by electrons. The direct component can be described by summing over dipolar coupling between N dipoles or spins:

$$H_{nn}^{direct} = \sum_{i<j}^{N} \frac{\hbar^2 \gamma^2}{r_{ij}^3} \left[\vec{I_i} \cdot \vec{I_j} - 3 \frac{(\vec{I_i} \cdot \vec{r_{ij}}) \cdot (\vec{I_j} \cdot \vec{r_{ij}})}{r_{ij}^2} \right] \tag{2.19}$$

where $\vec{I_i}$ and $\vec{I_j}$ are nuclear spins at different sites and $\vec{r_{ij}}$ is the vector between them. In experiments, this interaction leads to a broadening of the resonance spectrum of the nuclear spins on the order of the field felt at a particular nucleus from the other nuclei. The field is typically on the order of a few gauss, producing a linewidth on the order of a few kilohertz, depending on the gyromagnetic ratio.

The indirect coupling is more difficult to describe as it depends on the behavior of the electrons in the material. The Hamiltonian is written as:

$$H_{nn}^{indirect} = \sum_{ij} \vec{I}_i a_{ij} \vec{I}_j \tag{2.20}$$

where a_{ij} is the coupling tensor between the nuclear spins which is determined based on the details of the coupling mechanism between the nuclei and electrons in the system. The basic mechanism is described by the hyperfine interaction between the nucleus and an electron, which subsequently interacts with another nucleus mediating the interaction between the nuclei. The effects of these interactions in experiments depend on details of the hyperfine coupling in the system and can lead to either a narrowing or broadening of the resonance spectrum [55]. In metals this indirect coupling is known as the RKKY when the interactions are mediated by conduction electrons [59].

2.2.3 Electric quadrupole interactions

The quadrupolar Hamiltonian H_Q describes the interaction between the nuclear quadrupole moment Q and its local electric field gradient (EFG) $V_{\alpha\beta}$. The EFG tensor $V_{\alpha\beta}$ is created by the charge distribution around the nucleus.

$$V_{\alpha\beta} = \frac{\delta^2 V}{\delta x_\alpha \delta x_\beta}(r = 0) \tag{2.21}$$

where V is the electrostatic potential and x_α and x_β are x,y,z. The trace of the EFG tensor must be zero giving us:

$$V_{XX} + V_{YY} + V_{ZZ} = 0 \tag{2.22}$$

V_{ZZ} is chosen as the largest component by convention. We then define our asymmetry parameter:

$$\eta = \frac{V_{XX} - V_{YY}}{V_{ZZ}} \tag{2.23}$$

with $0 \leq \eta \leq 1$. The EFG can then be described by just two parameters V_{ZZ} and η, allowing us to write the quadrupolar Hamiltonian H_Q as:

$$H_Q = \frac{h\nu_q}{2}\left(I_Z^2 - \frac{I(I+1)}{3} + \frac{\eta}{6}(I_+^2 + I_-^2)\right) \tag{2.24}$$

where Z is the principal axis of the EFG and I is the nuclear spin. It can be shown that the quadrupole moment Q vanishes for $I = 0, \frac{1}{2}$ therefore $I \geq 1$. I_+ and I_- are the raising and lowering operators and ν_q is the nuclear quadrupole frequency given by:

$$\nu_q = \frac{3eQV_{ZZ}}{2I(2I-1)h} = \frac{3e^2Q}{2I(2I-1)h} \tag{2.25}$$

The quadrupolar interaction is the basis for nuclear quadrupole resonance (NQR) experiments. Because the quadrupolar splitting of the nuclear magnetic energy levels does not require the application of an external field, it can be used to study electronic states that are sensitive to the strong magnetic fields required for NMR experiments.

The quadrupolar interaction is usually much weaker than the Zeeman interaction and is treated as a perturbation of the Zeeman Hamiltonian when $\nu_q \ll \nu_L$. The first order correction to the mth Zeeman energy levels is given by the following:

$$E_m^{(1)} = \frac{3eQV_{zz}}{4I(2I-1)}[3m^2 - I(I+1)] \tag{2.26}$$

where

$$V_{zz} = V_{XX}\sin^2\theta\cos\phi + V_{YY}\sin^2\theta\sin\phi + V_{ZZ}\cos^2\theta \tag{2.27}$$

Where θ is the angle between the EFG V_{ZZ} and the external field $H_0\hat{z}$ and ϕ is a rotation around the $\hat{z}$ direction.

2.2.4 Nuclear Quadrupole Resonance (NQR)

The quadrupolar splitting of the nuclear energy levels is present without applying an external field, allowing us to manipulate the Nuclear Quadrupole Resonance (NQR) at zero field. The ability to perform experiments without applying an external field can be a powerful tool for the case where the electronic state is sensitive to the strong field required in typical NMR experiments. The nuclear quadrupolar frequency for a spin 3/2 nucleus is given by:

$$\nu_{NQR} = \nu_q\sqrt{1+\frac{\eta^2}{3}} = \frac{3eQV_{ZZ}}{2I(2I-1)h}\sqrt{1+\frac{\eta^2}{3}} \tag{2.28}$$

where η is the asymmetry parameter in Eq. (2.23). For the case of $\eta = 0$ we get $\nu_{NQR} = \nu_q$ giving the following energy splittings of a spin 3/2 nucleus:

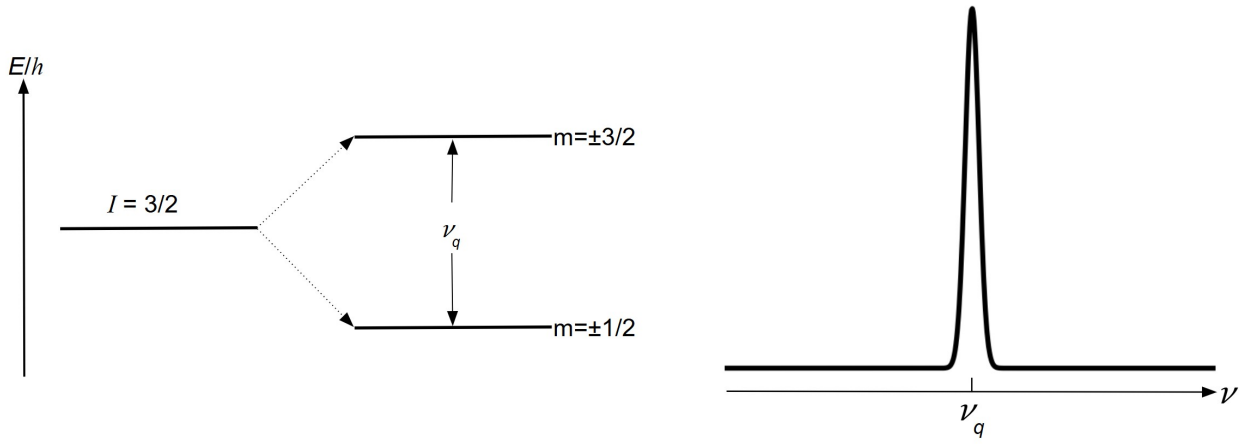


Figure 2.1: The diagram shows an example of the energy splitting in a spin 3/2 nucleus with uniaxial symmetry. The resulting NQR spectrum is a peak in frequency at ν_q.

NQR was the primary measurement performed in the superconducting state of $LaNiGa_2$ and the results will be discussed in Chapter 7.

2.2.5 Nuclear Magnetic Resonance (NMR)

In the presence of a strong magnetic field the Zeeman interaction dominates the splitting of the nuclear spin energy levels given in Eq. (2.4). The quadrupolar and hyperfine interactions can be treated as perturbations to the Zeeman Hamiltonian.

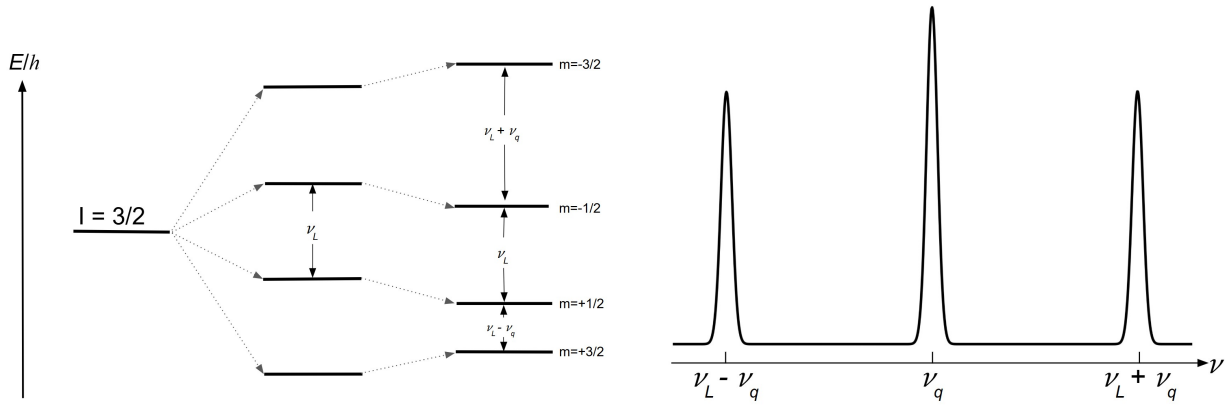
The first-order shifts of the nuclear magnetic energy levels E_m due to the electric quadrupolar interaction in a system with uniaxial symmetry are given by the following:

$$E_m^{(1)}(\theta, \phi, \eta) = \frac{1}{4} h\nu_q (3cos^2\theta - 1)[m^2 - \frac{1}{3} I(I+1)] \tag{2.29}$$

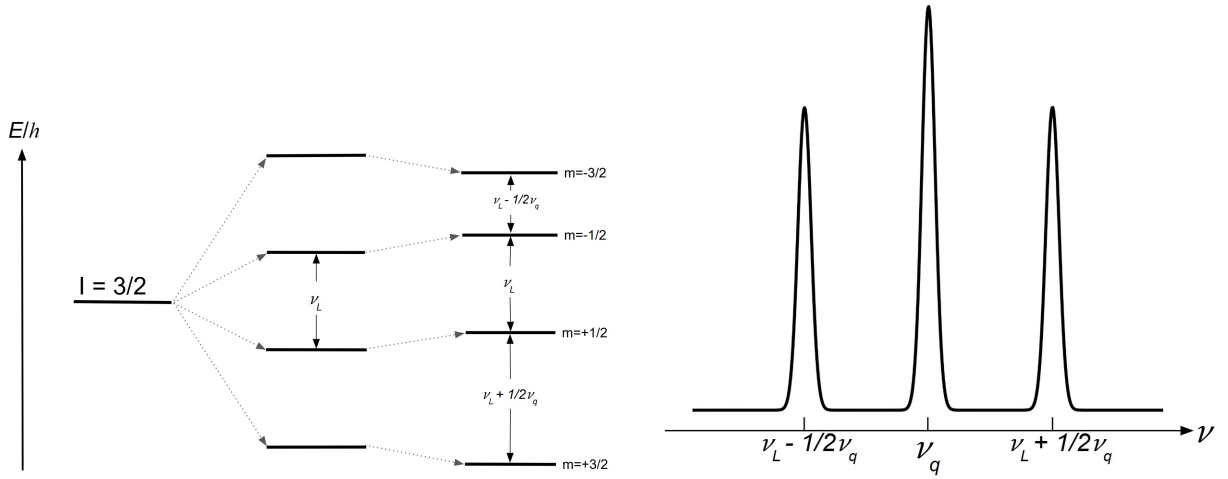
The resulting shift of the spectrum relative to the unshifted central -1/2 to +1/2 transition to first order is:

$$\Delta^{(1)}\nu_m(\theta) = -\frac{\nu_q}{2}(3cos^2\theta - 1)(m - 1/2) \tag{2.30}$$

Below are diagrams reflecting the changes to the nuclear magnetic energy levels of a spin 3/2 nucleus with the external field parallel and perpendicular to the principal axis of the EFG, respectively.



a) Energy level splitting and NMR spectrum with field parallel to the principal axis of the EFG ($\theta = 0°$)



b) Energy level splitting and NMR spectrum with field perpendicular to the principal axis of the EFG ($\theta = 90°$)

Figure 2.2: The figures above show how the nuclear spin energy level splitting and resulting NMR spectrum of an $I = 3/2$ nucleus in a strong magnetic field taking into account the first-order quadrupolar effects. The $\eta = 0$ and two different orientations of the external field relative to the principal axis of the electric field gradient (EFG) are shown.

The magnetic field evenly divides the nuclear spin energy levels of an $I = 3/2$ nucleus, resulting in 3 degenerate transitions at $\nu_L = \gamma H_0$. The first-order shifts due to the quadrupolar interaction are dependent on the orientation of the applied field to the principal axis of the electric field gradient EFG given by equation (2.29). When $\theta = 0$ the $m = \pm 3/2$ levels are shifted by $E^{(1)}_{\pm 3/2}(\theta = 0°) = +1/2\nu_q$ and the $m = \pm 1/2$ levels are shifted by

$E^{(1)}_{\pm 1/2}(\theta = 0°) = -1/2\nu_q$. These shifts result in three resonance lines with a central line and two satellites separated by $2\nu_q$ as shown in Figure 2.2 (a). When $\theta = 90°$ the levels of $m = \pm 3/2$ are shifted by $E^{(1)}_{\pm 3/2}(\theta = 90°) = -1/4\nu_q$ and the levels of $m = \pm 1/2$ are changed by $E^{(1)}_{\pm 1/2}(\theta = 90°) = +1/4\nu_q$. The resulting spectrum consists of three resonance lines with a central line and two satellites separated by ν_q as shown in Figure 2.2 (b). The best measure of the quadrupolar shift in both cases comes from measuring the separation between the satellites as opposed to the distance between the central and satellites as the central line can be shifted by a second-order quadrupolar effect. The second-order shift for a spin $I = 3/2$ nucleus with $\eta = 0$ is given by [68] [48]:

$$\Delta^{(2)}\nu_m(\theta, \phi, \eta) = -\frac{\nu_q^2}{6\nu_L}\big[I(I+1) - 3/4\big]\big[A(\phi,\eta)cos^4\theta + B(\phi,\eta)cos^2\theta + C(\phi,\eta)\big] \tag{2.31}$$

where

$$\begin{aligned} A(\phi,\eta) &= -\frac{27}{8} - \frac{9}{4}\eta cos2\phi - \frac{3}{8}\eta^2 cos^2 2\phi \\ B(\phi,\eta) &= \frac{30}{8} - \frac{1}{2}\eta^2 + 2\eta cos2\phi - \frac{3}{4}\eta^2 cos^2 2\phi \\ C(\phi,\eta) &= -\frac{3}{8} + \frac{1}{3}\eta^2 + \frac{1}{4}\eta cos2\phi - \frac{3}{8}\eta^2 cos^2 2\phi \end{aligned}$$

2.3 Relaxation

The dynamical process of relaxation is the key to performing measurements in NMR. Magnetic moments in the presence of a magnetic field $\vec{H}_o$ will experience a torque $\vec{T}$:

$$\vec{T} = \frac{d\vec{I}}{dt} = \vec{\mu} \times \vec{H}_0 \tag{2.32}$$

For the nuclear magnetization $\vec{M}$ resulting from a collection of nuclear magnetic moments $\vec{\mu}$, the equation of motion is:

$$\frac{d\vec{M}(t)}{dt} = \gamma(\vec{M}(t) \times \vec{H}_0) \tag{2.33}$$

The solution is the precession of the magnetization $\vec{M}$ around the external field with the frequency $\omega_L = \gamma H_0$. According to Boltzmann statistics, at thermodynamic equilibrium with the magnetic field $\vec{H}_0$ pointed along the z-axis the resulting components of the magnetization are $M_z = M_0$ and $M_x = M_y = 0$. The magnetization can be changed by applying an additional circularly polarized magnetic field $\vec{H}_1$ perpendicular to $\vec{H}_0$ that is oscillating at a frequency ω. The combined magnetic field experienced by the magnetization is $\vec{H} = \vec{H}_0 + \vec{H}_1$ with the component given by:

$$\begin{aligned} H_x &= H_1 cos\omega t \\ H_y &= H_1 cos\omega t \\ H_z &= H_0 \end{aligned} \tag{2.34}$$

For further analysis it is useful to go from the fixed frame S to a new rotating reference frame S' rotating at the same frequency ω as $\vec{H}_1$ around the direction of the external magnetic field $\vec{H}_o$ and replacing x,y and z in the rotating frame with x',y' and z'. In the rotating frame $\vec{H}_1(t)$ becomes a static field because the frequency of the oscillation and the frame are chosen to be exactly matched. The direction of $\vec{H}_1$ can be chosen to be anywhere in the plane perpendicular to $\vec{H}_0$ since the phase is arbitrary. Therefore, we will fix the $\vec{H}_1$ direction to be fixed along $\hat{x}'$. During the application of the radio frequency field, the effective magnetic field is given by the following:

$$\vec{H}_{eff} = (H_0 + \frac{\omega}{\gamma})\hat{z}' + H_1\hat{x}' \tag{2.35}$$

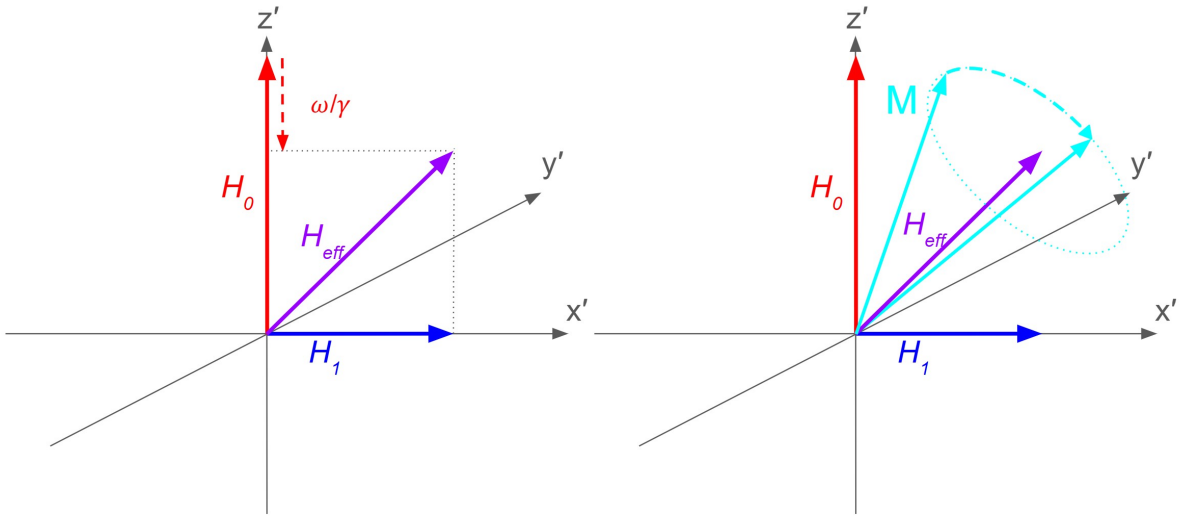


Figure 2.3: Above on the left is the sketch of the effective magnetic field in the rotating S' frame when not at resonance $\omega \neq \frac{-\omega_L}{\gamma}$. The right shows the precession of the magnetization around the effective field.

While the radio frequency field is active, the magnetization will precess around the new effective field. When resonance occurs meaning $\omega = -\omega_L = -\gamma H_0$, the $\hat{z}'$ component of the effective field vanishes. The result is the magnetization only precessing around $\vec{H}_1$. The precession around $\vec{H}_1$ is what allows us to control the orientation of the magnetization by changing the duration that $\vec{H}_1$ is applied. The change in angle of the magnetization relative to $\hat{z}'$ is given by:

$$\alpha = -\gamma H_1 t_p \tag{2.36}$$

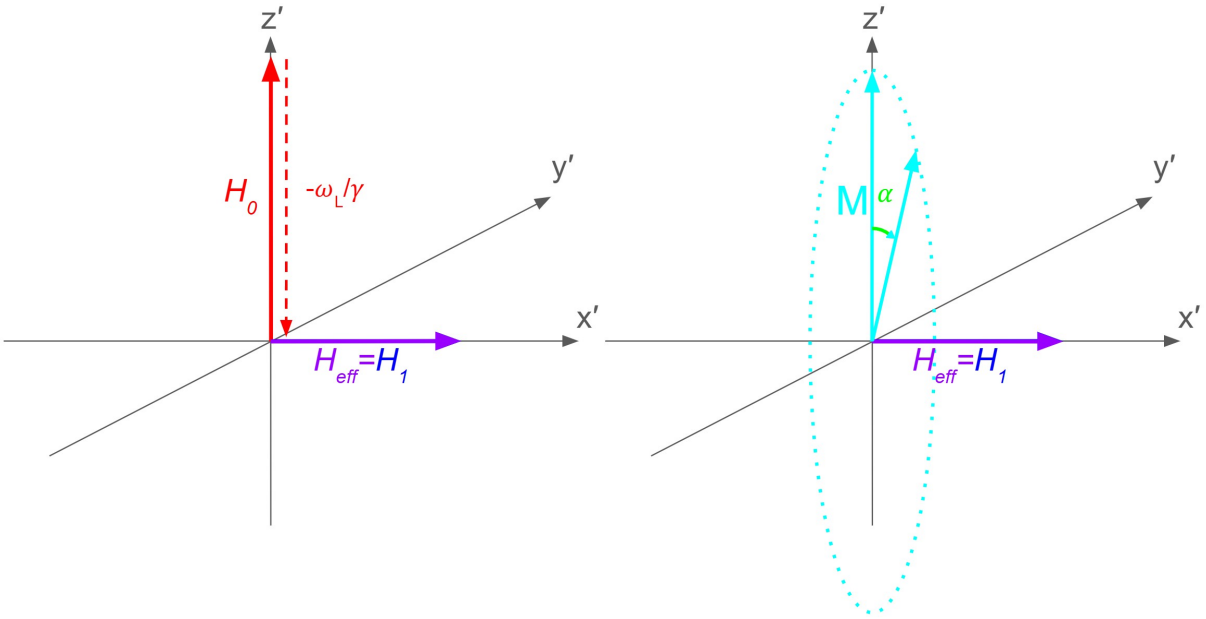


Figure 2.4: Above on the left is the sketch of the effective magnetic field in the rotating S' frame when at resonance $\omega = \frac{-\omega_L}{\gamma}$ resulting in $H_{eff} = H_1$. The right shows the precession of the magnetization around this H_1 and what the α angle represents.

where t_p is the duration of the pulse of the applied radio frequency field with strength H_1. Carefully varying these two parameters allows us to perform the two primary types of pulses used in NMR. The $\alpha = 90^o$ pulse flips the magnetization into the $\hat{y}'$ direction and the $\alpha = 180^o$ pulse which flips the magnetization to the $-\hat{z}$ direction. The application of any pulse that results in an $\alpha \neq 180n$ where n is any integer, results in a finite magnetization in the x or y direction resulting in a reduction of M_z. Once the pulse is stopped, the system will return to thermodynamic equilibrium with $M_z = M_0$ and $M_x = M_y = 0$. The recovery of the magnetization of the system back to equilibrium is different for the different components of the magnetization. The transverse component of the relaxation or the in-plane relaxation is T_2, while the longitudinal component of the relaxation is T_1. The relaxation equations in

the laboratory frame $\boldsymbol{S}$ are as follows:

$$\begin{aligned}\frac{dM_x(t)}{dt} &= -\frac{dM_x(t)}{T_2} \\ \frac{dM_y(t)}{dt} &= -\frac{dM_y(t)}{T_2} \\ \frac{dM_z(t)}{dt} &= \frac{M_0 - M_z(t)}{T_1}\end{aligned} \tag{2.37}$$

The longitudinal relaxation time T_1 is also referred to as the spin-lattice relaxation time because changes to M_z require changes in the populations of the nuclear spin energy levels in the system, which can only occur through energy exchanges with the lattice. The transverse relaxation time T_2, also called the spin-spin relaxation time, is different because changes to M_x and M_y do not require any energy transfers. T_2 is the timescale of the dephasing of the nuclear spins in the xy-plane as a result of interactions between nuclear spins, with local electron spins, and inhomogeneities in the external field. Combining the equation of motion 2.33 with the relaxation equations 2.37 results in the Bloch equations in the lab frame [7]:

$$\begin{aligned}\frac{dM_x(t)}{dt} &= \gamma(\vec{M}(t) \times \vec{H})_x - \frac{dM_x(t)}{T_2} \\ \frac{dM_y(t)}{dt} &= \gamma(\vec{M}(t) \times \vec{H})_y - \frac{dM_y(t)}{T_2} \\ \frac{dM_z(t)}{dt} &= \gamma(\vec{M}(t) \times \vec{H})_z + \frac{M_0 - M_z(t)}{T_1}\end{aligned} \tag{2.38}$$

These equations describe the relaxation of the magnetization to equilibrium while precessing around the z direction.

2.3.1 Spin-Lattice Relaxation in Metals

The primary relaxation of interest in NMR experiments is the spin-lattice relaxation or T_1. The spin-lattice relaxation requires a transfer of energy making it a powerful technique for

indirectly observing the electronic states around a given nucleus in metallic solids. The spin-lattice relaxation process is dominated by the conduction electrons in metals where a nucleus returns to the ground state by flipping the spin of a conduction electron to an excited state. Since the energy for flipping a nuclear spin is very small, only electrons close to the Fermi energy are able to help mediate this process. Therefore, the spin-lattice relaxation rate in metals is directly proportional to the density of states close to the Fermi level and can be calculated for a single nucleus using Fermi's golden rule resulting in the following equation:

$$W_{1,single} = \frac{2\pi}{\hbar} |\langle \psi_{m\mathbf{k}s} | V | \psi_{m\mathbf{k}'s'} \rangle|^2 \delta(E_m + E_{\mathbf{k}s} - E_n - E_{\mathbf{k}'s'}) \tag{2.39}$$

m and n denote the initial and final spin states of the nucleus while $\mathbf{k}s$ and $\mathbf{k}'s'$ are the initial and final momentum and spin of the electron mediating the transition. The remaining terms $\langle \psi_{m\mathbf{k}s} | V | \psi_{m\mathbf{k}'s'} \rangle$ are the elements of the scattering matrix between the nucleus and electron which can be expanded to include all of the nuclear spins in the system by integrating over the entire density of states. We can substitute the free electron approximation of the electronic states according to the Fermi function $f(E) = \frac{1}{e^{((E-E_F)/k_BT)}+1}$ into the electronic component of equation (2.38) to derive the complete nuclear relaxation rate of the system:

$$W_1 \propto \int_0^\infty |\langle \psi_{m\mathbf{k}s} | V | \psi_{m\mathbf{k}'s'} \rangle|^2 f(E)(1-f(E))N^2(E)dE \propto TN^2(E_F) \tag{2.40}$$

$f(E)(1-f(E))$ denotes the occupation probabilities of the initial and final states, E_F is the Fermi energy, and $N(E)$ is the density of states of the free electrons. The approximation $f(E)(1-f(E)) \approx k_BT\delta(E-E_F)$ gives the final result showing that the spin-lattice relaxation rate is proportional to the temperature and the square of the density of states at the Fermi level.

If we assume that the electrons in our metal are non-interacting forming a Fermi gas, the Fermi contact is the dominant source of the interactions between the nuclear spin and electrons. We can then relate the temperature dependence of the spin-lattice relaxation rate T_1 to the Knight shift described in section (2.2.2) according to the Korringa relation [37]:

$$K_s^2 T_1 T = \frac{\hbar}{4\pi k_B}\left(\frac{\gamma_e}{\gamma_n}\right)^2 = S_0 \tag{2.41}$$

where K_s is the Knight shift and γ_e and γ_n are the gyromagnetic ratios of the electron and nucleus respectively. Equation 2.41 only holds in the case of fully non-interacting electrons and therefore needs to be slightly modified to account for electronic correlations. The modified Korringa ratio is given by the following [22, 34, 63]:

$$K_s^2 T_1 T = \alpha S_0 \tag{2.42}$$

the additional term α can be used to determine the types of electronic correlations present in our system. $\alpha = 1$ indicates that there are no electronic correlations in our system. $\alpha > 1$ indicates the presence of ferromagnetic correlations between electrons [63]. While $\alpha < 1$ indicates possible antiferromagnetic correlations [63]. Interpretations of a non-constant α have to be made carefully as both the Knight Shift and spin-lattice relaxation rate depend on the temperature, density of states of the electrons, and field [37]. A constant value of α, however, is usually proof of a Fermi liquid. The exact value of α is heavily influenced by the form of the hyperfine coupling and the potential disorder of the system and therefore should also be carefully analyzed [63].

2.3.2 Spin-Lattice Relaxation Due to Fluctuating Fields

The spin-lattice relaxation can also be driven by the presence of a fluctuating magnetic field which is given by:

$$T_1^{-1} = \gamma^2 \int_0^\infty \left\langle h_\perp(t) h_\perp(0) \right\rangle e^{i\omega_L t} dt \tag{2.43}$$

where $\left\langle h_\perp(t) h_\perp(0) \right\rangle$ is the autocorrelation function of the field $\vec{h}(t)$ perpendicular to the external field in $\hat{z}$. Equation (2.43) is the Fourier transform of the correlation function with only fields fluctuating close to the Larmor frequency ω_L contributing to the relaxation of the nuclei. In the case of random fluctuations in $\vec{h}(t)$ perpendicular to $\vec{H}_0$, the autocorrelation function can be rewritten as:

$$\left\langle h_\perp(t) h_\perp(0) \right\rangle = h_\perp^2 e^{-t/\tau_c} \tag{2.44}$$

with τ_c being the correlation time. We can then substitute this into equation (2.43) and evaluate the integral to get the following:

$$T_1^{-1} = \gamma^2 h_\perp^2 \int_0^\infty e^{-t/\tau_c} e^{i\omega_L t} dt \tag{2.45}$$

$$T_1^{-1} = \frac{\gamma^2 h_\perp^2 \tau_c}{1 + \omega_L^2 \tau_c^2} \tag{2.46}$$

Although these equations describe relaxation for any randomly fluctuating local fields, the fluctuations are typically ascribed to the Brownian motion in liquids and gases and spin fluctuations in magnetic materials. In these cases, the following form of the correlation time

can be derived [8]:

$$\tau_c = \tau_0 e^{E_a/k_B T} \tag{2.47}$$

where E_a is the energy required to activate the fluctuation source (electron spins or molecular motion) and τ_0 is the maximum fluctuation at high temperatures.

When the source of the fluctuating fields is the hyperfine interaction with the electrons equation (2.43) can be rewritten in terms of the dynamical susceptibility of the electrons χ'' [45]. The spin-lattice relaxation rate then becomes:

$$T_1^{-1} = \frac{2\gamma^2 k_B T}{g^2 \mu_B^2} \lim_{\omega \to 0} \sum_{\mathbf{q}} |A(\mathbf{q})|^2 \frac{\chi_{\perp}''(\mathbf{q}, \omega_L)}{\omega_L} \tag{2.48}$$

where g is the Landé factor, $A(\mathbf{q})$ are the transverse components of the hyperfine coupling and $\chi_{\perp}''(\mathbf{q}, \omega_L)$ is the imaginary component of the dynamic susceptibility of the electrons at wave vector $\mathbf{q}$ and with the Larmor frequency ω_L. The dependence of the hyperfine coupling on the wave vector $\mathbf{q}$ means that the ability of the electrons to mediate spin flips of the nuclei depends on the location of the nucleus in the Brillouin Zone (B.Z.). T_1 is therefore also $\mathbf{q}$ dependent and can be a powerful tool in filtering and observing only specific regions of the B.Z. of interest in NMR experiments.

2.3.3 Spin-Spin Relaxation

The spin-spin relaxation rate or the relaxation of the magnetization in the plane perpendicular to $\hat{z}$ is more commonly called T_2. T_2 is the timescale for the decoherence and loss of magnetization M_x and M_y and is brought on by indirect and direct interactions between nuclear spins which is why it is referred to as spin-spin relaxation. T_2 can also generally be

caused by inhomogeneities in the external field. Furthermore, relaxation of the magnetization back to the $\hat{z}$ direction or spin-lattice relaxation also contributes to T_2 since it must also cause a decrease in the magnetization in the plane [58]. The relaxation rate $\frac{1}{T_2^*}$ is given by the sum of the causes resulting in the following:

$$\frac{1}{T_2^*} = \frac{1}{T_2^{direct}} + \frac{1}{T_2^{indirect}} + \frac{1}{T_2^{Redfield}} + \frac{1}{T_2^{inhomogeneities}} \tag{2.49}$$

with the first two terms coming from spin-spin interactions, the third term coming from the contribution due to spin-lattice relaxation, and the final term coming from distributions of Larmor frequencies caused by inhomogeneities in the external field. The term coming from the field inhomogeneities is usually left out as it is canceled out during the typical Hahn spin echo pulse sequence used in NMR measurements which will be further explored in the next chapter. The spin-spin relaxation rate in general is very difficult to discuss as there are many factors that contribute to it. However, it is a very important measure experimentally for determining the proper timing of pulse sequences. Although T_2 can also be used in other ways for example as an indication of quantum fluctuations, the work presented in this thesis will only be giving a limited description relevant to performing proper NMR measurements.

2.4 Measurements

2.4.1 Free Induction Decay (FID)

The time-dependent magnetization changes the magnetic flux through the coil containing the sample, resulting in an induced voltage that can be detected.

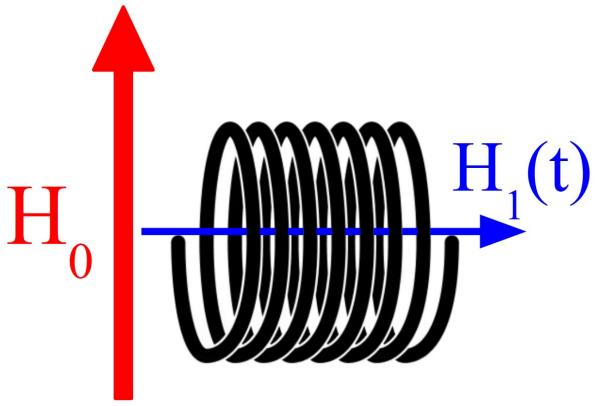


Figure 2.5: In a typical NMR experiment a sample is placed in a coil with its loops oriented perpendicular to the external field $\vec{H}_o$. The same coil is used to apply the radio frequency field pulses $\vec{H}_1(t)$ and measure the resulting signal through Faraday induction.

The simplest measurement that can be performed in NMR is free induction decay (FID). The FID is measured by applying a 90^o or $\frac{\pi}{2}$ pulse and observing the subsequent induced voltage through the coil as the magnetization fluctuates within the coil resulting in a time-dependent magnetic flux through the coil. The FID signal comes from the fluctuation of magnetization between M_x and M_y and varies slightly with inhomogeneities in the local magnetic fields of the nuclei, resulting in a distribution of Larmor frequencies of nuclear spins.

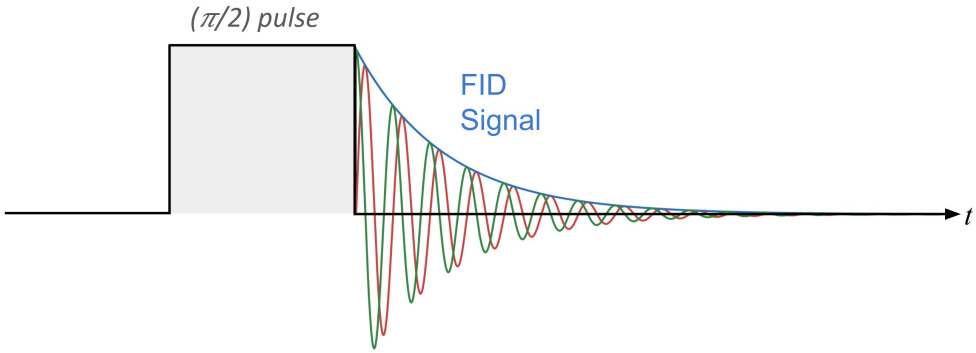


Figure 2.6: Above is a drawing of a $\pi/2$ pulse followed by the resulting oscillation between the magnetization in the plane M_x and M_y which gives the FID signal.

The signal is reduced exponentially after the pulse is applied due to the loss of coherence for the in-plane magnetization given by T_2. The Fourier transform of the FID signal reveals the

response of the fraction of the NMR spectrum within the excitation window centered around the frequency of the applied pulse ν_r. The Fourier transform of a square pulse is given by:

$$F(\nu) = F_o \frac{sin[\pi(\nu - \nu_{applied})t_p]}{\pi(\nu - \nu_{applied})t_p} \tag{2.50}$$

Depending on the size of the excitation window and the width of the NMR spectrum, one measurement frequency may be enough to capture the whole spectrum. Otherwise, a frequency sweep or field sweep may be required to capture the whole spectrum.

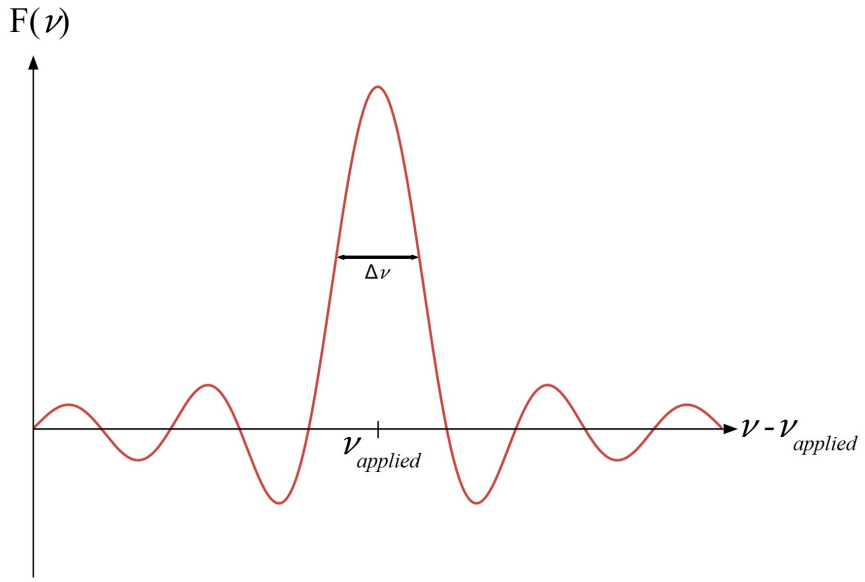


Figure 2.7: This is the plot of the Fourier Transform of a square pulse which is a sinc function centered around the applied frequency. $\Delta\nu$ shows the excitation window of the pulse in the frequency domain.

The duration of the NMR pulse is inversely proportional to the frequency window that the pulse can excite. In the Fourier transform of the square pulse in Fig. 2.7 we can see the FWHM or excitation window in the frequency domain:

$$\Delta\nu \approx \frac{1}{t_p} \tag{2.51}$$

where t_p is the duration of the pulse. $\Delta\nu$ is typically on the order of 100kHz, which is usually well within the resonance window of the NMR circuit described in 3.1.

2.4.2 Spin-Echo

The Hahn spin echo is the primary pulse sequence used in NMR experiments as it can be used to mitigate the shortcomings of an FID measurement. The sequence consists of a 90^o or $\pi/2$ pulse followed by a 180^o or π pulse as shown in the figure below.

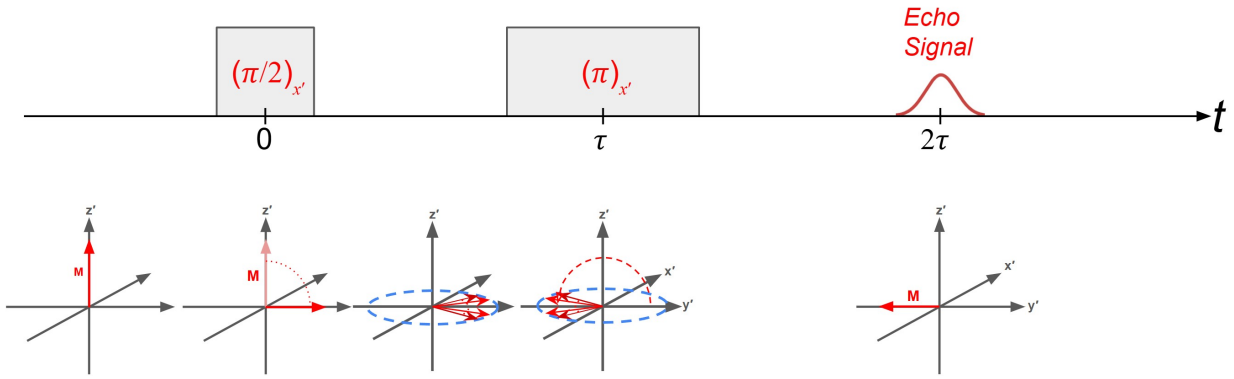


Figure 2.8: A diagram of a Hahn spin echo sequence along with a visual representation of the effects of the sequence on the magnetization in the rotating frame S'.

Before the first pulse, the magnetization points in the direction of the externally applied field $z' = z$. When the $\pi/2$ pulse is applied, the magnetization is rotated into the transverse plane. The resulting magnetization points in either x' or y' depending on the type of pulse applied. In the chosen example, an x' pulse is applied resulting in the magnetization rotating about the x' axis and pointing in the y' direction after the $\pi/2$ pulse. The magnetization is then allowed to decohere in the plane for a time τ. As a result of the variation in the local fields experienced by the different nuclear spins in the sample, there is a variation in the speeds of the precession of the spins in the plane. The next π pulse flips the spins around the x' axis resulting in the spins precessing in the opposite direction. The spins will then reverse the precession that occurred during the first time τ and refocus after another time

τ, resulting in an echo signal at time 2τ.

The time between the pulse and the echo allows us to separate our signal from the high voltage pulses used to manipulate the magnetization. In contrast, an FID measurement is always coupled with strong noise from the $\pi/2$ pulse since it is measured immediately after the pulse.

The echo signal comes from the induced voltage in the coil when the magnetization is refocused. The integral of the echo in the time domain is therefore proportional to the number of spins that were manipulated by the pulse sequence. The Fourier transform of the echo allows us to see the portion of the NMR spectrum within the excitation window of our pulse sequence. If the full spectrum is larger than the excitation window of the pulses, multiple measurements can be performed and combined to give a smooth complete spectrum.

2.4.3 Measuring T_2

The time scale of τ used in the Hahn echo pulse sequence described in the previous section is set by the duration over which the spins can still refocus. The π pulse is only able to refocus the spins that de-cohere in the plane due to field inhomogeneities. Therefore, the other terms contributing to the decoherence given in Eq.2.49 will decrease the number of spins participating in the echo sequence and a reduced signal. The rate at which the signal is lost can be measured to determine spin-spin relaxation rate T_2^{-1}. The measurement of T_2 is done by performing a sequence of Hahn echo measurements as shown in Fig. 2.8 with increasing τ and looking at the resulting decay curve of the signal as a function of time. Since the echo appears at τ after the π pulse the total time the spins have had for the in plane relaxation after the initial $\pi/2$ pulse is 2τ. Therefore, the signal is plotted versus 2τ in T_2 measurements.

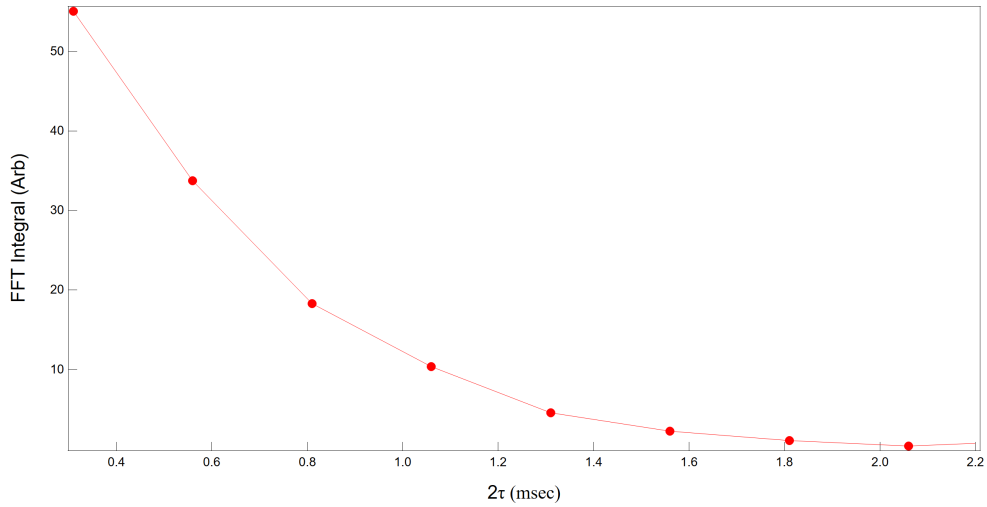


Figure 2.9: Above is an example of a T_2 measurement performed on ^{69}Ga in $LaNiGa_2$ at 4K. The integral of the Fourier Transform of the echo is used to measure the signal and plotted as a function of 2τ

The decay of the signal corresponding to the in plane magnetization M_{xy} is fitted to the following exponential function to determine the spin-spin relaxation rate T_2^{-1}.

$$M_{xy}(2\tau) = M_0 e^{(\frac{-2\tau}{T_2})} \tag{2.52}$$

The fitting function can be generalized to extract different contributions to the relaxation rate, but is not relevant to this work. [9]

2.4.4 Measuring T_1

Measuring the spin-lattice relaxation T_1^{-1} is one of the keys to gaining insight into the electronic system as mentioned in 2.3.1 and 2.3.2. The key is to manipulate the populations of the nuclear spin states to change the magnetization and then performing a Hahn-echo sequence to observe the magnetization as the spin populations relax. The pulse sequence for the measurement is given by the following:

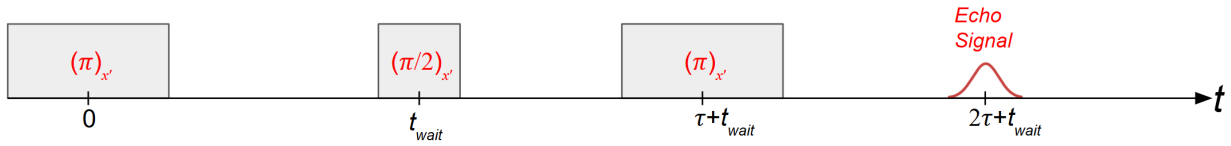


Figure 2.10: The diagram shows the inversion recovery spin echo pulse sequence where a π pulse is used to fully invert the magnetization then allowed to relax for a duration t_{wait} after which a Hahn echo sequence is used to measure the state.

The diagram uses a π pulse to initially invert the nuclear magnetization M_z but different pulse lengths and sequences can be used to initialize the nuclear magnetization in order to measure the relaxation rate. Since the intensity of the Hahn echo sequence depends on the orientation of the nuclear magnetization along $\hat{z}$, varying t_{wait} allows us to observe M_z until it is fully relaxed.

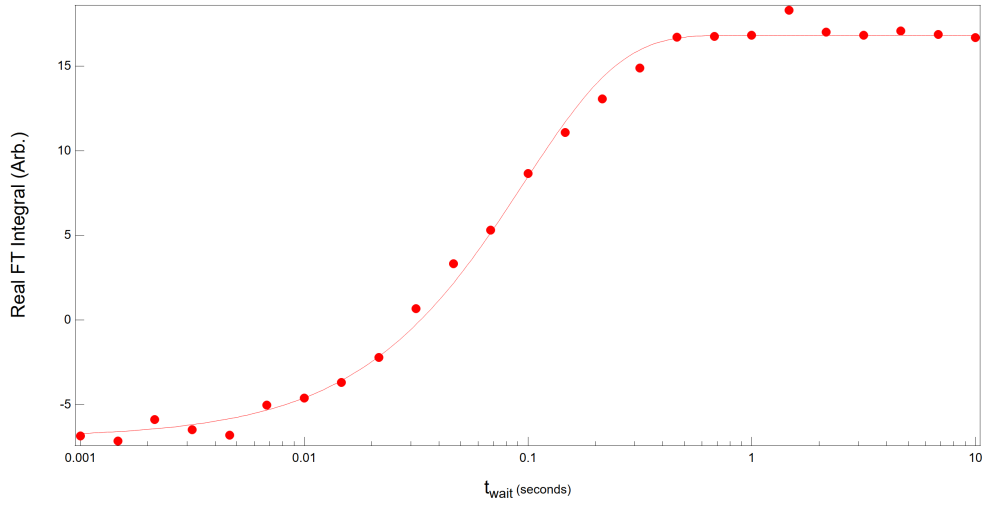


Figure 2.11: An example of a T_1 measurement performed on ^{139}La. The signal is plotted versus t_{wait} and fitted to an exponential to determine T_1.

Chapter 3

Techniques and Instrumentation

3.1 NMR Resonance circuit

The signal from the induced voltage due to the change in magnetization of a sample within the NMR coil shown in Fig.2.5 is very small, often as small as one μV. The Johnson-Nyquist noise (thermal noise) of the circuit is approximately on the same order. For example, a 50Ω circuit at room temperature and 1MHz the noise is approximately $0.895\mu V$. Therefore, the NMR resonance circuit (tank circuit) needs to be fine-tuned very closely to maximize the sensitivity at the measured frequency because the voltage across the coil is QV_{coil} with Q being the quality factor of the circuit. The matching of the resonance is achieved by creating a tunable circuit which can be changed precisely to a desired frequency.

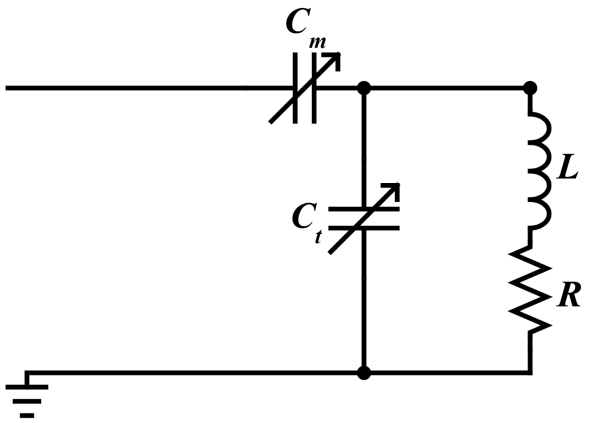


Figure 3.1: A diagram of the NMR tank circuit.

The tank circuit shown in figure 3.1 consists of a tuning capacitor C_t in parallel with the coil L, which has resistance R. Both are in series an impedance matching capacitor C_m. The circuit is wired at the end of the probe on a 50Ω semi-rigid coaxial cable which is placed within the cryostat. Once the probe is placed into the cryostat, the two variable capacitors are the only way to tune the resonance frequency of the circuit and are controlled by two long rods extending from the top of the probe.

The resonance of the tank circuit can be determined by solving the equation for the total complex impedance Z of all the components in the circuit for the case where the real part of the impedance is matched to $\mathrm{Re}[Z] = 50\Omega$ and the imaginary part $\mathrm{Im}[Z] = 0\Omega$. We begin with the total impedance

$$Z = \frac{1}{i\omega C_t + (i\omega L + R)} + \frac{1}{i\omega C_m} \tag{3.1}$$

The equation can then be expanded to separate the real and imaginary parts

$$\mathrm{Re}[Z] = \frac{R}{(R^2 + L^2\omega^2)(\frac{R^2}{(R^2+L^2\omega^2)^2} + (C_t\omega - \frac{L\omega}{R^2+L^2\omega^2})^2)} \tag{3.2}$$

$$\mathrm{Im}[Z] = \frac{L\omega}{(R^2 + L^2\omega^2)(\frac{R^2}{(R^2+L^2\omega^2)^2} + (C_t\omega - \frac{L\omega}{R^2+L^2\omega^2})^2)} - \frac{1}{C_m\omega} - \frac{C_t\omega}{\frac{R^2}{(R^2+L^2\omega^2)^2} + (C_t\omega - \frac{L\omega}{R^2+L^2\omega^2})^2} \tag{3.3}$$

By setting $\mathrm{Re}[Z] = 50\Omega$ and $\mathrm{Im}[Z] = 0\Omega$ at a given frequency ω the tuning capacitance must be

$$C_t = \frac{50L\omega^2 - \sqrt{50(R^3\omega^2 + L^2R\omega^4 - 50R^2\omega^2)}}{50(R^2\omega^2 + L^2\omega^4)} \tag{3.4}$$

with the matching capacitance being

$$C_m = \frac{R}{5\sqrt{2}\sqrt{R\omega^2(-50R + R^2 + L^2\omega^2)}} \tag{3.5}$$

Proper matching is essential to ensure the maximum efficiency of the power absorbed when applying pulses and gaining the best signal. The quality of the matching is indicated by the reflection coefficient

$$\rho = \frac{Z - 50\Omega}{Z + 50\Omega}. \tag{3.6}$$

We can see that when the circuit is properly matched with $Z = 50\Omega$ the reflection coefficient

goes to zero and the voltage is perfectly dropped across the tank circuit. With the voltage across the tank circuit given by:

$$V_{tank} = QV_{coil} \tag{3.7}$$

where Q is the quality factor of the circuit measured by $Q = f_0/FWHM$ with f_0 being the minimum reflection frequency and FWHM being the full width at half the minimum of the reflection as a function of frequency.

The variable capacitors in the probe C_t and C_m have a range from 3pF to 120pF. The resistance and inductance depend on the diameter of the wire used and the number of turns in the coil. Before beginning any NMR experiment it is very important to note the maximum and minimum tuning frequency of the tank circuit to ensure the desired measurement frequency falls well within the tuning range. The decrease in the resistance of the circuit as the probe cools down shifts up the tuning range slightly as the temperature decreases.

There are some physical limitations in the geometry of the probe which create a parasitic capacitance limiting the minimum possible capacitance and in turn the maximum tunable frequency of the probe.

3.2 Magnets

Superconducting magnets are at the core of conventional NMR experiments. In our group at UC Davis we maintained and operated two magnets: (1) a fixed field Oxford Instruments AS500 11.7285T magnet and (2) a variable field Quantum Design PPMS magnet. NMR experiments require very good field homogeneity, typically on the order of 10 parts per million (ppm) in the sample space (about $1cm^3$), as such these magnets require a great deal of material and electrical engineering. The basic structure of a NMR magnet is a large solenoid of superconducting wire which generates the primary field and depending on the desired field homogeneity various field correcting superconducting shim coils are used around

the primary magnet.

The Quantum Design PPMS magnet is kept connected to the power supply and can be operated anywhere from 0T to 9T. It does not use shimming coils and has a field homogeneity of 15 ppm at the sample space.

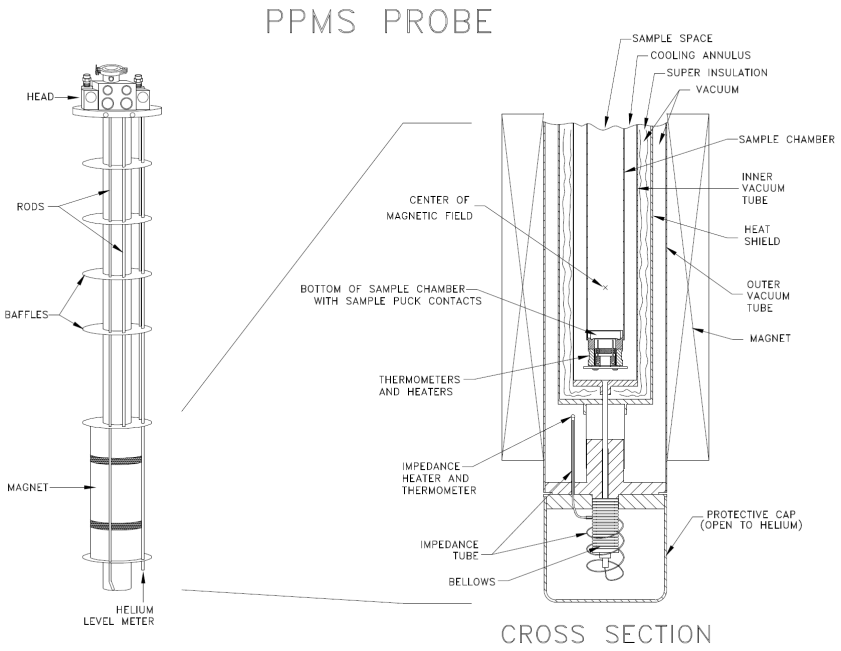


Figure 3.2: A diagram of the PPMS probe and magnet.

The Oxford AS500 is disconnected from any external power and is perpetually operated at 11.7285T. It has nine superconducting shimming coils which greatly increase its field homogeneity to around 0.70 ppm.

3.3 Cryogenics

3.3.1 Liquid Helium Cryostats

The superconducting magnets described in the previous section require very low temperatures in order to stay superconducting. Furthermore, signal to noise in NMR is typically

inversely proportional to temperature. Therefore, cryogenics are an essential part of NMR experiments. The superconducting magnets are kept cold by staying immersed in a liquid helium bath (4K).

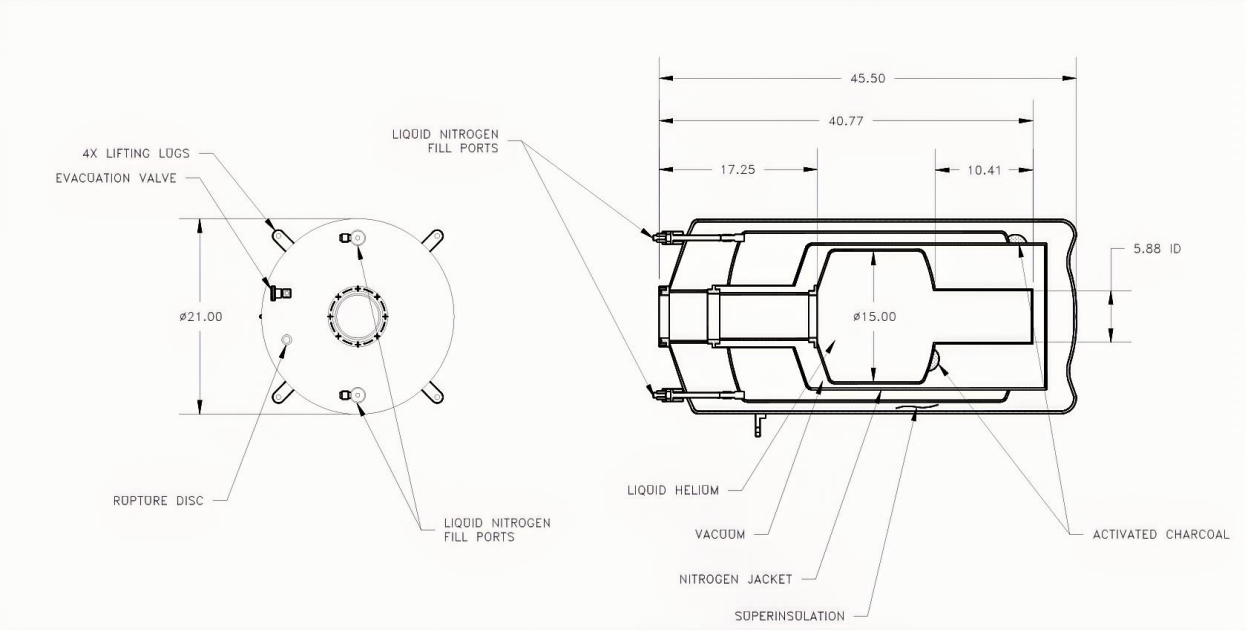


Figure 3.3: Schematic of the PPMS liquid Helium Dewar.

As helium is very expensive and transfers are time consuming it is best to maximize the insulation around the liquid helium space. Figure 3.3 shows how this is typically achieved. The liquid helium bath is in the center where the magnet in Figure 3.2 would be placed. Surrounding the bath is a vacuum space which is then surrounded by a liquid nitrogen jacket. The liquid nitrogen (LNe) at 77K acts as an important buffer layer between room temperature and 4K within the liquid helium bath as such, it is important to regularly fill the LNe. The last layer is another vacuum space with super insulation around the liquid nitrogen jacket. Activated charcoal is placed within both vacuum spaces to absorb contaminants. Even with all of the layers properly in place the boil-off of the liquid helium is unavoidable as there is still a slight thermal contact with the room. Furthermore, operating the magnet introduces a heat load through the leads to the magnet. In our lab group at UC Davis and at

Los Alamos National Lab (LANL), the boil-off is captured and liquefied to minimize costs. The re-liquefication for the whole MPA-Q group at LANL is handled by trained research technologists. In Davis, this process is done within the lab, where the boil-off is all collected into five large tanks and then liquefied using a Quantum Design ATL160 Helium Liquefier. The temperature in the sample space in the PPMS is controlled by a heater, pump, and a valve allowing some of the helium into the sample space. In the Oxford system a Sumitomo cold head and heater are used to control the temperature. In both systems, liquid helium can be allowed to build up in the sample space and then pumped out to maximize the cooling power and achieve temperatures well below liquid helium of around 1.7K. Here we are limited by the strength of the pump available as lower temperatures can be achieved with a more powerful pump [6].

3.3.2 Oxford Liquid Dilution Refrigerator

Although 1.7K is low enough for most NMR experiments, some measurements require even lower temperatures. One option is to use ^3He instead of ^4He which after pumping can get down to as low as 300mK. However, there is a much more effective usage of ^3He to achieve even lower temperatures in the form of a dilution refrigerator. Conventional pumping reduces the temperature of a liquid by continuously removing the highest energy atoms from the system, but there is a minimum temperature for the liquid when the vapor pressure is so low that very few atoms are being pumped. For helium there is a further complication in that it enters a superfluid phase at 2.17K greatly increasing the heat capacity and creating containment problems. These are overcome in a dilution refrigerator by taking advantage of a different phase that can go to much lower temperatures.

When liquid ^3He and ^4He are mixed and cooled, there is a natural separation of the two due to the higher density of ^4He. When ^4He undergoes a superfluid transition the ^3He floats above. Due to their smaller size, higher energy ^3He atoms are able to mix into the superfluid

^4He resulting in a concentrated ^3He phase on top of a dilute ^3He phase (the leftmost phase in figure 3.4). The phase separation and the percentage of ^3He in the dilute phase (ideally 6.6%) are critical to the operation of a dilution refrigerator. ^3He are spin 1/2 particles and therefore fermions which obey Fermi statistics to form a Fermi liquid within the superfluid ^4He. The highest energy ^3He atoms can then be removed in a process similar to pumping on a liquid to continuously reduce the temperature in the dilute phase.

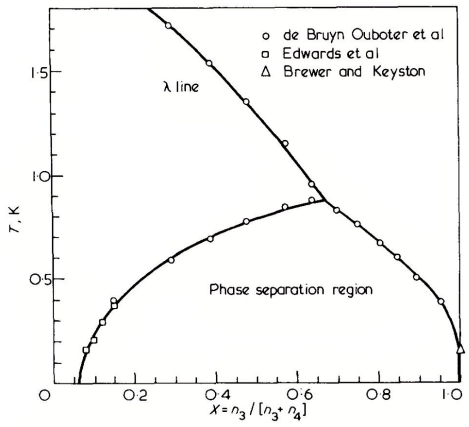


Figure 3.4: Phase diagram of ^3He and ^4He mixture from [13] with the temperature on the vertical axis and the percentage of ^3He on the horizontal axis.

Precise control of the ratio of ^3He and ^4He and the phase separation is very difficult to achieve in a real physical system. The Oxford Instruments Wet Dilution Refrigerator was used for this work.

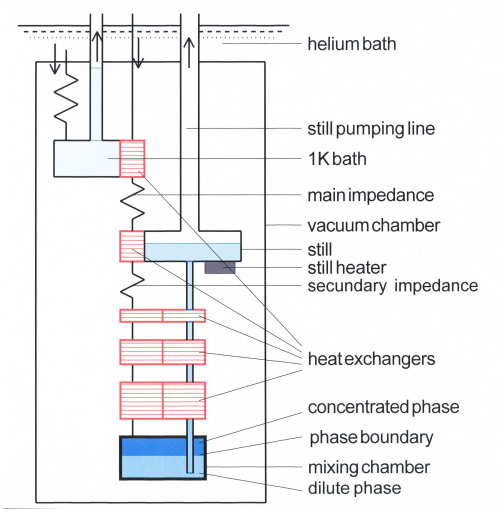


Figure 3.5: Schematic of a wet dilution refrigerator

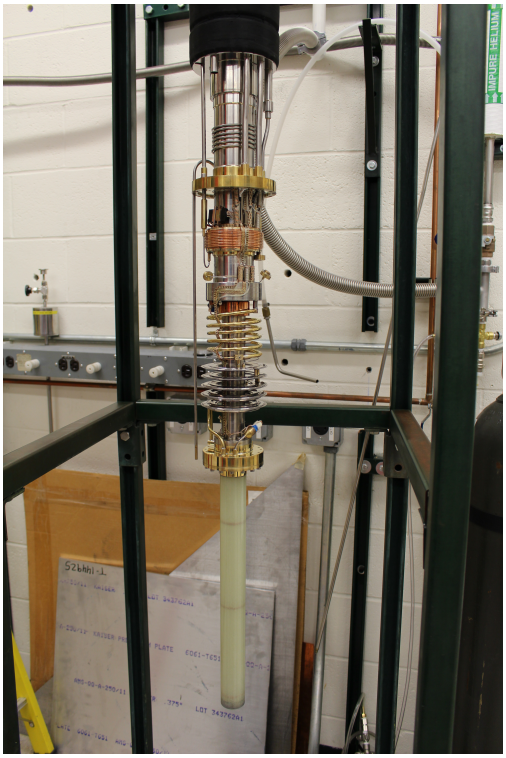


Figure 3.6: Photo of the inside of the insert in the Oxford Instruments wet dilution refrigerator taken by Adam Dioguardi.

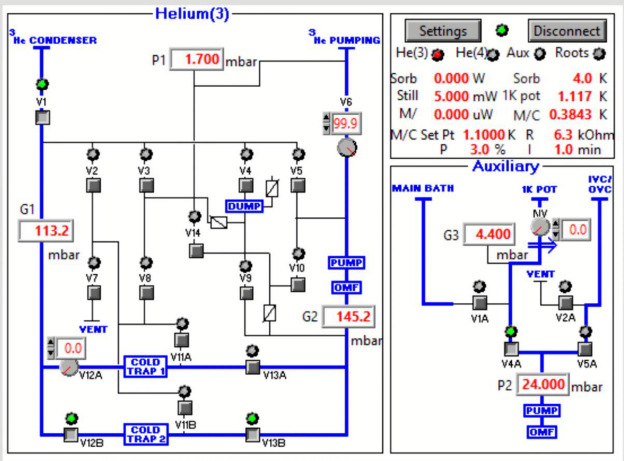


Figure 3.7: The digital control panel used to control the pumps and valves in the system.

The whole dilution refrigerator is placed within a liquid helium Dewar similar to the one described in figure 3.3. The system is started by opening a small valve connecting the main liquid helium bath to the 1K bath. This space is pumped with a strong pump to keep the temperature of the bath close to 1K. The next part of the operation is to slowly introduce the mixed gas of ^3He and ^4He through heat exchangers connected to the 1K bath. This process liquefies the mixed gas which collects in the mixing chamber. An outlet is present at the bottom of the mixing chamber which connects to the still. Once all of the mixture is liquefied, a pump connected to the still is used to further reduce the temperature in the mixing chamber. Once the temperature reaches about 870mK, the phase separation occurs with the concentrated ^3He floating above a dilute ^3He phase within superfluid ^4He. Since the outlet to the still is at the bottom of the mixing chamber and ^3He is lighter than ^4He, the highest energy ^3He atoms are selectively pumped out of the still which continuously decreases the temperature in the mixing chamber. The concentrated ^3He gas from the still is fed back into the system, forming a closed loop. This closed loop allows ^3He and ^4He to be conserved in the system and their ratios to be maintained. The proper use of heat exchangers in the system requires very narrow and high impedance lines; therefore, it is very important to continuously filter the gas through cold traps during operation to remove any

contaminants that may clog the system.

3.4 Samples

3.4.1 $LaNiGa_2$

Samples of $LaNiGa_2$ were grown by the Taufour group at UC Davis primarily by Jackson Badger and also by Yunshu Shi. They were able to grow high-quality single crystals which were essential to the work in this thesis. Many small single crystals were used with one example shown below.

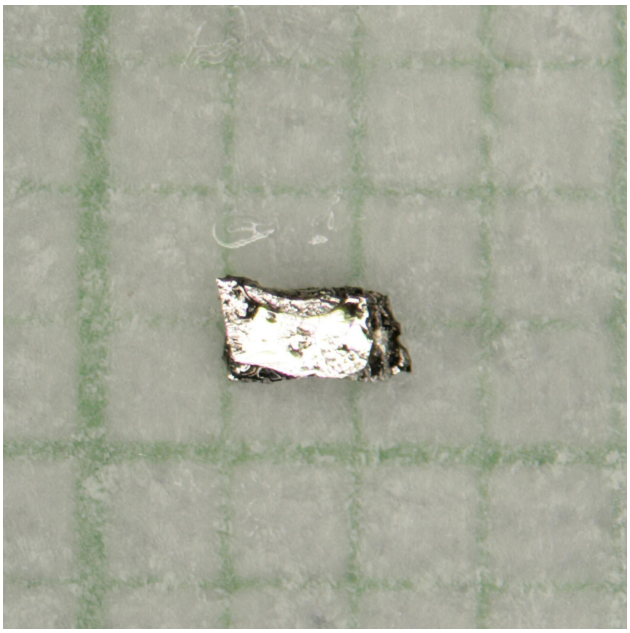


Figure 3.8: Picture of the first sample of $LaNiGa_2$ used to measure the normal state. The photo is taken under a microscope while looking down the b-axis and each grid line corresponds to 1mm.

Single crystals from the same batch were gathered and ground down to perform NQR experiments in the superconducting state.

3.5 Challenges and Solutions

3.5.1 Temperature

Two major challenges presented themselves with respect to the temperature in the NMR measurements of $LaNiGa_2$. The first was the limitation of the minimum temperature in the Curro lab at UC Davis. Since the superconducting transition is close to 2K and the minimum temperature in the lab was around 1.7K, it was impossible to look deeper into the superconducting state. Furthermore, because the measurements were performed near the base temperature, the system was susceptible to the heat load caused by power being transferred into the system during a measurement. Even the small power input into the circuit by the network analyzer was enough to heat up the sample and suppress the superconducting state.

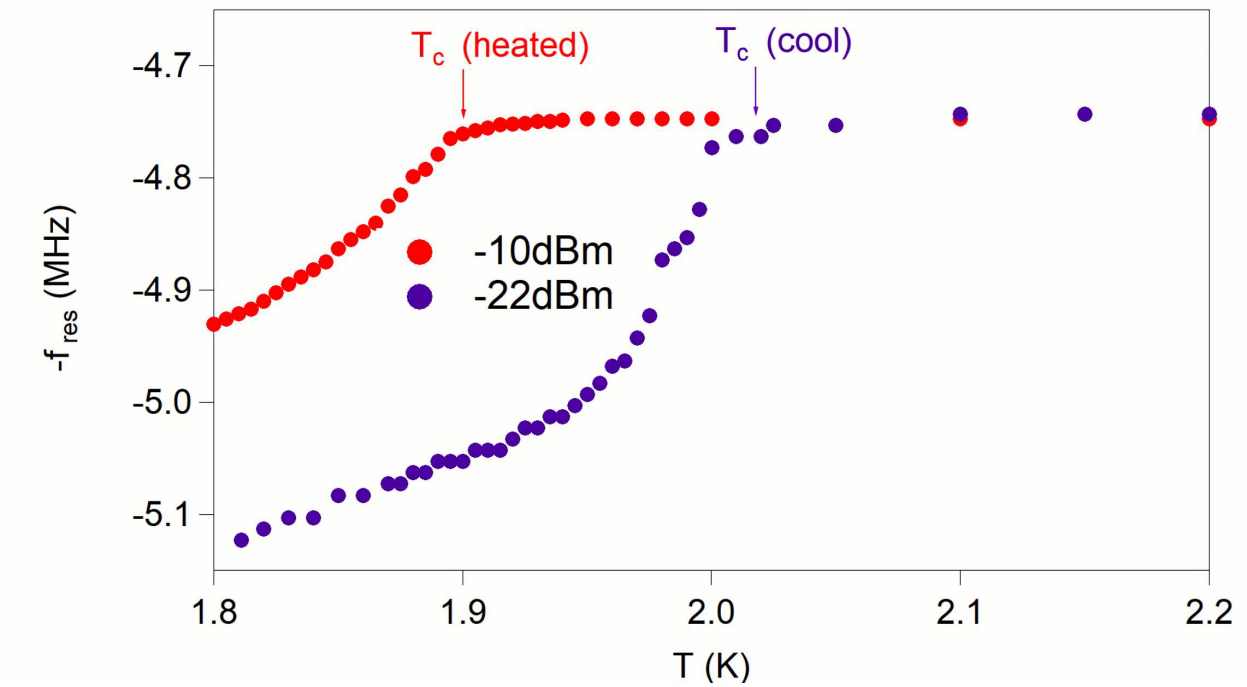


Figure 3.9: The plot shows the negative of the measured resonance frequency as a function of the temperature on the PPMS for two different power settings on the network analyzer.

Figure 3.9 shows the change in the resonance frequency of the tank circuit that occurs when

the sample becomes superconducting due to the resulting drop in the inductance of the coil. We can see that just -10dBm corresponding to 0.1mW at 50Ω is enough to significantly heat the sample, as seen from the suppression of the transition. The temperature axis is the set temperature of the PPMS, rather than the sample, and the sample was in a helium gas environment which is not the best thermal coupling, limiting the thermalization rate. The increase in temperature caused by the Eddy currents formed when the RF pulses are applied is therefore difficult to manage.

Two solutions were used to overcome this issue. The first was to use much longer pulses with very small power when running. The wider pulses greatly reduced the excitation window (2.7) and created a limitation in completely measuring the spectrum, but the relaxation rate was still able to be measured. The temperature dependence was measured while reducing the power until the results were stable.

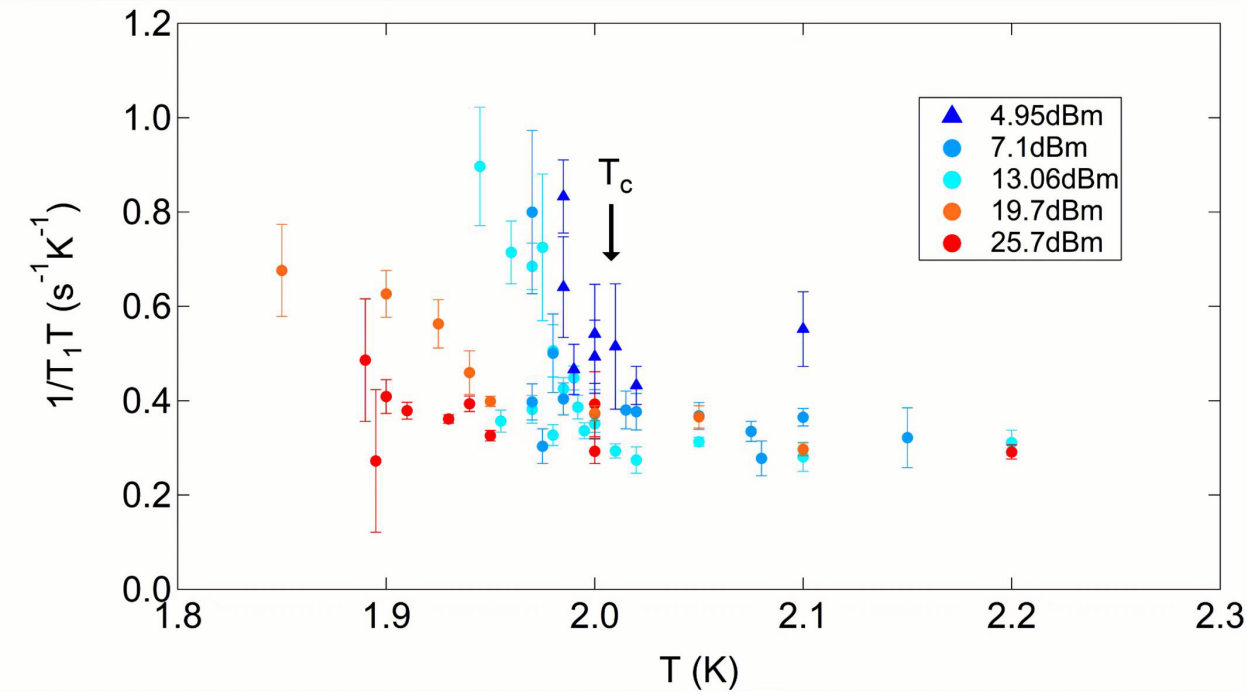


Figure 3.10: The plot shows the temperature dependence of $1/T_1T$ for five different power levels in the RF-pulses

The plot shows that once the RF power is below 13.06dBm the temperature dependence of $1/T_1T$ is consistent indicating that the effects of heating are mitigated. It is important to note that the network analyzer in figure 3.9 applies power continuously while the RF pulses are only applied for a small fraction of a second which is why there is a discrepancy in their dBm values.

The second solution was to move the experiments from UC Davis to Los Alamos National Lab where a dilution refrigerator was available. The lower temperature allowed for measurements deep into the superconducting state. Furthermore, the system is a wet dilution refrigerator meaning the sample was submerged in the liquid ^3He and ^4He in the mixing chamber greatly increasing the thermal coupling and thermalization rate of the sample. The increased cooling power allowed for much shorter and more powerful pulses to be used in order to capture the spectrum in addition to the relaxation rate.

3.5.2 Signal Loss

As we proceeded with measurements in the dilution refrigerator, a new challenge presented itself in the loss of signal in the superconducting state. The signal intensity dropped by 95 percent below T_c. Although the measurements were still possible by averaging more scans, this was not practical with respect to time as T_1 grows exponentially deeper in the superconducting state greatly increasing the time per scan.

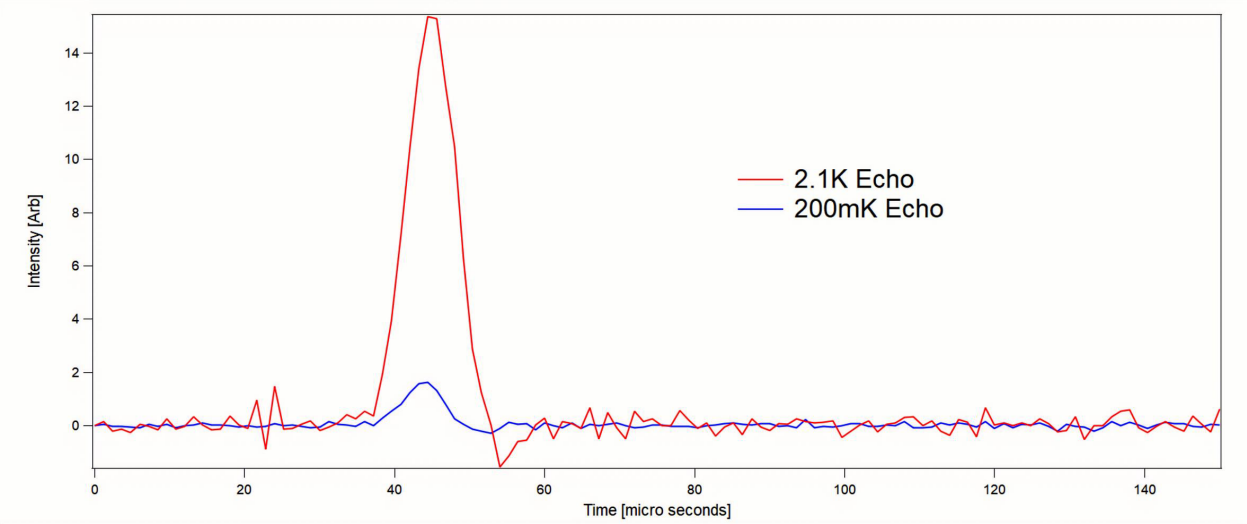


Figure 3.11: The plot shows the echo from two measurements, one at 200mK and the other at 2.1K, with the same pulse conditioned and normalized by the number of scans for a direct comparison.

The dramatic loss of signal intensity is due to the Meissner effect which limits how far the H_1 field can penetrate a superconductor meaning nuclei in the sample below the penetration depth were no longer participating. The limit is described the London penetration depth [39] as follows:

$$B(x) = B_0 e^{-x/\lambda_L} \tag{3.8}$$

$$\lambda_L = \sqrt{\frac{m}{\mu_0 n_s e^2}}$$

Where $B(x)$ describes the exponential decaying field of the field B_0 as it enters a distance x into the superconductor. m is the effective mass of the Cooper pairs, μ_0 is the permeability of free space, n_s is the superfluid density and e is the charge of an electron. This value is for a conventional BCS superconductor and can vary significantly, especially for type 2 superconductors where vortices allow for the penetration of the field well into the sample. The penetration depth $\lambda(0)$ in $LaNiGa_2$ was measured through μSR experiments to be around 150nm [72]. The average grain size in the initial experiment of 150-300 microns was

therefore far too large. The solution came from further grinding the samples and filtering through a 10 micron sieve until the average grain size was well below 10 microns. The grinding process introduced strain into the system so the NQR spectrum of the ^{71}Ga(1) was measured before and after grinding to make sure the change was not too drastic. The results of these studies can be found in Appendix A.

Chapter 4

Triplet Superconductors

4.1 General Background

Electrons are fermions and therefore the overall wavefunction of the Cooper pair must be antisymmetric under particle exchange. Since the wave functions for the superconducting condensate with s or d wave symmetry are symmetric under particle exchange, the spin component of the wavefunction must be antisymmetric, meaning the spins are anti-aligned forming a spin Singlet with $S = 0$. The vast majority of superconductors are, therefore, singlet superconductors. There are, however, a few examples of superconductors which appear to have a triplet pairing of electrons with the spins aligned with $S = 1$. Two well-known candidates are UPt_3 and UTe_2. UTe_2 is marked by multiple superconducting phases and very large anisotropic upper critical fields exceeding 40 teslas [56]. UPt_3 is also characterized by multiple superconducting phases along with a low-temperature superconducting phase with evidence for time reversal symmetry breaking (TRSB) [60]. In both of these examples the triplet pairing is likely driven by strong electronic correlations from a ferromagnetic instability close to the superconducting phase [44]. TRSB was also observed in the superconducting state of $LaNiGa_2$ by muon spin resonance experiments (μSR) indicating possible triplet su-

perconductivity [25]. Unlike other candidates, the superconducting phase in $LaNiGa_2$ is not near a ferromagnetic instability and there appear to be no strong electronic correlations in the material [65]. This led to the proposal of a novel triplet (INT) state described in 5.2.3. Exploring the pairing in the superconducting state of $LaNiGa_2$ was the motivation for the work presented in the rest of this thesis.

4.2 Introduction to $LaNiGa_2$

$LaNiGa_2$ is an intermetallic superconductor with a transition temperature of $T_c = 2.1K$. It has a non-symmorphic and centrosymmetric crystal structure which results in a non-trivial band topology with band degeneracies at the Fermi level [2]. The space group of the crystal was determined to be C_{mcm} by Single Crystal X-ray Diffraction (SCXRD) with the structure shown below:

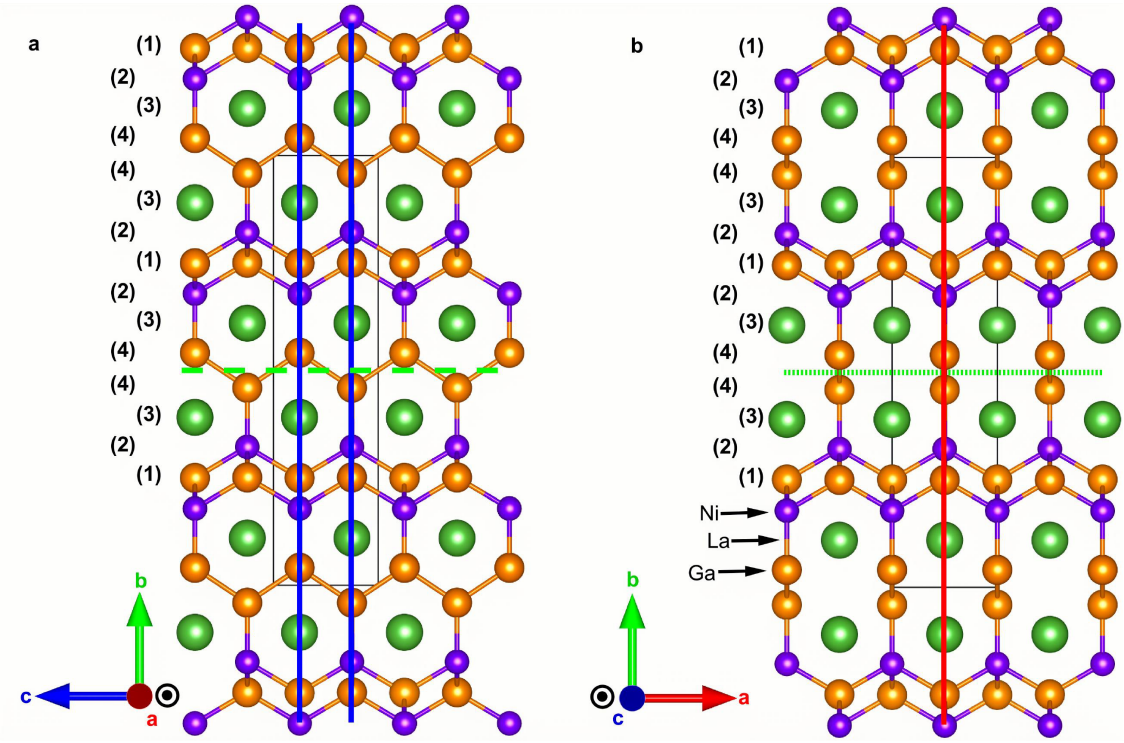


Figure 4.1: Above are two projections of the crystal structure of $LaNiGa_2$, with (**a**) showing the projection along the a-axis and (**b**) showing the projection along the c-axis. The green dashed lines show the c-glide plane perpendicular to the b-axis while the red and blue lines indicate the location of mirror planes. The numbers indicate the layer of a given element with (1) and (4) being Ga planes, (2) Nickel and (3) La [2].

In 2012 μSR experiments performed on polycrystalline samples revealed possible internal fields below T_c indicating possible TRSB in the superconducting state [25]:

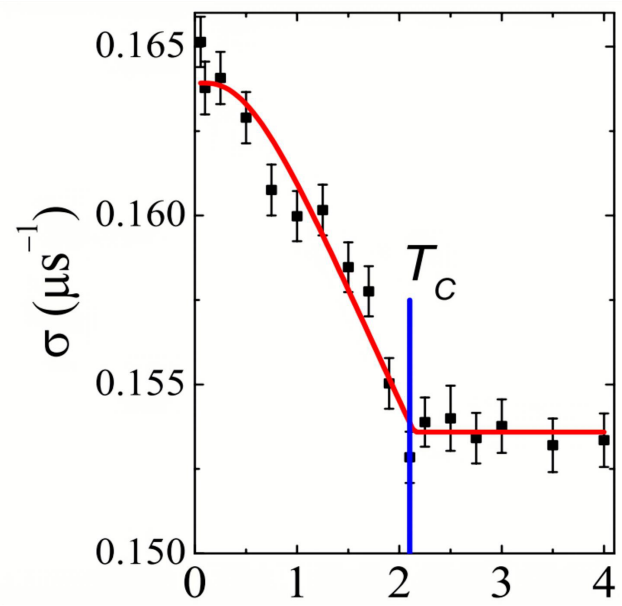


Figure 4.2: This is a plot of the muon spin depolarization rate σ with respect to temperature showing a clear enhancement below T_c [25].

This was a mystery because penetration-depth, μSR, and specific-heat measurements indicated a nodeless superconducting gap which typically cannot be a triplet. The INT model introduces the band degree of freedom, allowing the wave function to be antisymmetric in the band channel while the spin and orbital components remain symmetric [21]. This model gained support due to the non-trivial topology of the Fermi surface allowing for band degeneracies at the Fermi level [2].

The possibility of a novel form of triplet superconductivity made possible by non-trivial topology motivated this work to better understand the normal and superconducting states and determine the nature of the pairing of electrons in the superconducting state.

Chapter 5

NMR in the Superconducting State

5.1 Knight Shift

The spin susceptibility is a key measurement that can be performed in the superconducting state to determine the spin state of the Cooper pairs. Cooper pairs consist of a combination of two spin 1/2 electrons, which can result in an antiparallel alignment of the two spins with a net spin of $S = 0$ (singlet) or a parallel alignment with a net spin of $S = 1$ (triplet). If a superconductor has singlet pairing, then there is a drop in the spin susceptibility going into the superconducting state. If the pairing is a triplet there is no loss in spin susceptibility along the direction in which the spin of the Cooper pairs is aligned. The spin component of the Knight shift (2.16) is an excellent way to measure the local spin susceptibility in the superconducting state. Measuring the spin component of the Knight shift as $T \to 0$ is essential to probing the spin of the Cooper pair wavefunction [5, 30, 52].

The spin shift mediated by the hyperfine coupling is proportional to the static spin susceptibility and in the superconducting state can be written as:

$$K_{s,sc} \propto \chi_{s,sc} = -4\mu_B^2 \int_0^\infty N_{sc}(E) \frac{\partial f(E)}{\partial E} dE, \tag{5.1}$$

where $f(E)$ is the Fermi distribution function and N_{sc} is the density of states in the superconducting state [41]. We can compare this to the normal state by using the Pauli spin susceptibility (2.17) to get the ratio of the susceptibility in the normal state to the superconducting state:

$$\frac{K_{s,sc}}{K_{s,n}} = \frac{\chi_{s,sc}}{\chi_{s,n}} = -2\int_0^\infty \frac{N_{sc}(E)}{N_n(E)}\frac{\partial f(E)}{\partial E}dE \tag{5.2}$$

The density of states $N_n(E)$ can be put into the integrand since it is constant close to the Fermi level. For the case of a BCS superconductor which has singlet pairing with a single isotropic energy gap Δ, the density of states in the superconducting state is given by [4]:

$$\frac{N_{BCS}(E)}{N_n(E)} = \begin{cases} \frac{E}{\sqrt{E^2-\Delta^2}} & \text{for } (E > \Delta) \\ 0 & \text{for } (E < \Delta) \end{cases} \tag{5.3}$$

The behavior of the spin shift in the superconducting state can be derived by combining the equations 5.2 and 5.3. The result given by the Yoshida function is a decrease in the spin shift below T_c which becomes exponential at low temperatures [83]. As $T \to 0$ $K_s \to 0$, indicating the gapping out of quasi-particle states.

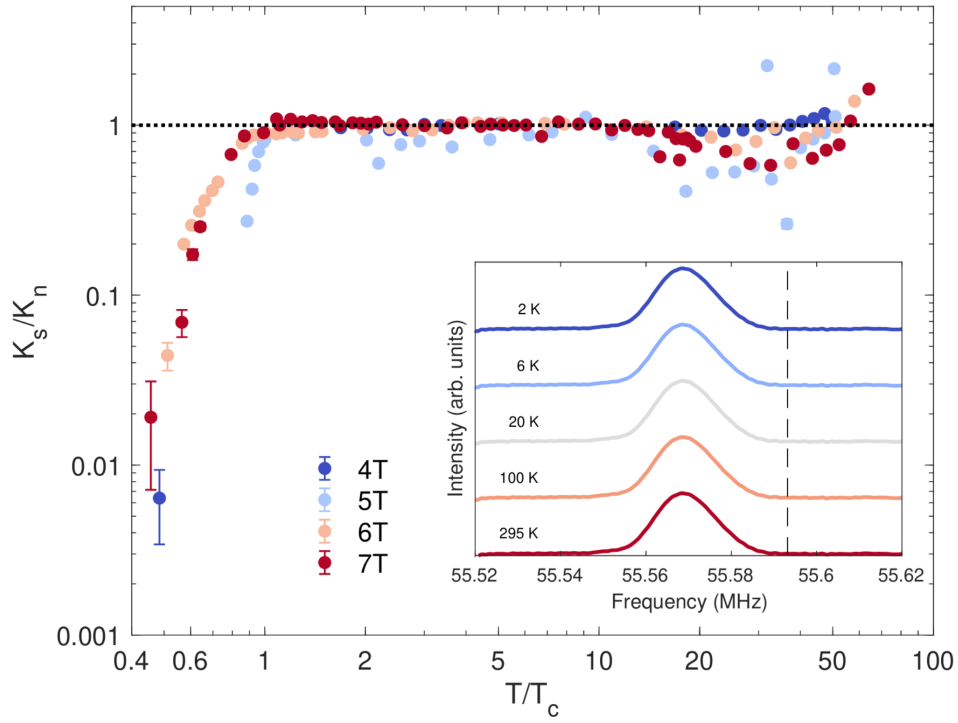


Figure 5.1: The temperature dependence of the Knight shift normalized to the Knight shift in the normal state in s-wave superconductor W_3Al_2C showing the exponential decrease below T_c [75].

For a spin-triplet superconductor, the behavior of the spin susceptibility in the superconducting state depends on the direction. The order parameter in this case is characterized by the $\vec{d}$-vector which describes the orientation of the spin of the cooper pairs and the magnitude of the superconducting gap [12]. The $\vec{d}$-vector defines a direction normal to the plane in which the Cooper pairs are trapped and is usually pinned to one of the crystalline axes by spin-orbit coupling. The spin of the Cooper pairs is confined to a direction perpendicular to the $\vec{d}$-vector. The orientation of the external magnetic field H_0 to the $\vec{d}$-vector therefore determines the behavior of the spin shift in the superconducting state. For example, if the $\vec{d}$-vector were pointed in the $\hat{z}$ direction, the spin of the Cooper pairs would be confined to the xy-plane. If measured with the field parallel to $\hat{z}$, then the spin shift would exhibit the drop as the BCS case described by the Yoshida function [83]. The spin shift measured

with the field along $\hat{x}$ or $\hat{y}$ direction would remain constant across T_c because the χ_s remains constant change across T_c [29]. The kngiht shift below T_c can be challenging to measure with NMR experiments as many superconductors such as $LaNiGa_2$ have very small upper critical fields that destroy the superconducting state. Furthermore, the superconducting state, especially close to T_c where the gap is small, is very sensitive to thermal fluctuations. The heat resulting from currents induced when applying NMR pulses can be enough to destroy the superconducting state. The Knight shift across T_c must therefore be carefully analyzed prior to drawing any conclusions about the pairing mechanism [52].

When performing experiments in real systems the Knight shift of singlet superconductors often does not vanish as $T \to 0$, but rather approaches a constant. The residual shift at low temperatures comes from the orbital component of the Knight shift K_{orb} as described in equation 2.14 which is independent of the temperature and the spin state of the electrons. The constant K_{orb} results in a finite shift as K_s vanishes as $T \to 0$. The relative contribution of K_{orb} depends on the strength of the orbital magnetism in the system with K_{orb} being the dominant term in some systems. In these systems the Knight shift can appear to not change across T_c even for singlet superconductors [49]. Disorder combined with strong spin-orbit coupling can also lead to non zero Knight shift for some singlet superconductors [26]. The orbital component is therefore critical to examine thoroughly before making any determinations about the pairing state of the electrons in a superconductor.

5.1.1 Diamagnetic Shielding

The diamagnetic shielding currents induced in a superconductor by the external field H_0 create an additional contribution to total shift on top of the spin and orbital components [15].

$$K_{total} = K_s(T) + K_{orb} - \frac{\Delta H(T)}{H_0} \tag{5.4}$$

where the demagnetization field ΔH indicates the reduction of the internal field as a result of the screening currents. These are sometimes also referred to as orbital currents and it is important to distinguish between the two effects. The orbital contribution to the Knight shift, K_{orb}, is essentially a local Van Vleck-like effect arising from the electronic orbitals surrounding the nucleus. In contrast, orbital currents are a long-range phenomenon associated with superconducting currents flowing through the material. The diamagnetic shift always leads to a decrease in the observed nuclear resonance frequency accounting for the negative sign in front of the new term and is both temperature and field dependent. Depending on the strength of the diamagnetic shift it can be challenging to properly interpret changes in spin susceptibility from the Knight shift in the superconducting state. Therefore, calculating an estimate of the diamagnetic shift from the demagnetization factors is essential to proper analysis of the Knight shift below T_c [50]. If multiple nuclei with the same spin degree of freedom are present in a sample, the K_{total} of both can be measured and subtracted to remove the diamagnetic shift and get the spin susceptibility scaled by the difference in the hyperfine coupling of the two nuclei. Below is an example with ^{11}B and ^{13}C in doped MgB_2 [11].

$$^{11}K_{total}(T) - ^{13}K_{total}(T) = (A_{11} - A_{13})\chi_s(T) \tag{5.5}$$

5.2 Spin-Lattice Relaxation Rate

5.2.1 BCS model

Historically, the first experimental evidence for the BCS theory of superconductivity came from measuring the spin-lattice relaxation rate in pure ^{27}Al in the superconducting state [4, 23]. We will now explore the proof and the predictions based on [76], starting with the

BCS ground state wave function:

$$|\Psi_{BCS}\rangle = \prod_{\vec{k}} (u_{\vec{k}} + v_{\vec{k}} c^{+}_{\vec{k}\uparrow} c^{+}_{-\vec{k}\downarrow}) \, |\Phi_0\rangle \tag{5.6}$$

where $|\Phi_0\rangle$ is the vacuum state, $c^{+}_{\vec{k}\uparrow}$ and $c^{+}_{-\vec{k}\downarrow}$ are the creation operators for the electron states, with the subscripts denoting the momentum and spin states. $u_{\vec{k}}$ and $v_{\vec{k}}$ are the coherence factors where $|u_{\vec{k}}|^2$ is the probability of finding an unoccupied Cooper pair while $|v_{\vec{k}}|^2$ is the probability of finding an occupied Cooper pair with the given momentum and spin with the constraint $|u_{\vec{k}}|^2 = 1 - |v_{\vec{k}}|^2$. The next step is to introduce the perturbing Hamiltonian in the superconducting state:

$$H_1 = \sum_{\vec{k}\sigma, \vec{k}'\sigma} B_{\vec{k}'\sigma', \vec{k}\sigma} (c^{+}_{\vec{k}'\sigma'} c_{\vec{k}\sigma} \pm c^{+}_{-\vec{k}-\sigma} c_{\vec{k}'-\sigma'}) \tag{5.7}$$

where the $\pm$ is determined by the particular perturbing Hamiltonian. The operators in equation 5.7 can be written in terms of Bogoliubov quasiparticles (Bogoliubons) which are fermionic quasiparticle operators above the BCS condensate defined by the Bogoliubov-Valatin transformation [10, 78]:

$$\begin{aligned} \hat{b}_{\vec{k}\sigma} &= u_{\vec{k}} \hat{c}_{\vec{k}\sigma} - \sigma v_{\vec{k}} \hat{c}^{+}_{-\vec{k}-\sigma} \\ \hat{b}^{+}_{\vec{k}\sigma} &= u_{\vec{k}} \hat{c}^{+}_{\vec{k}\sigma} - \sigma v_{\vec{k}} \hat{c}_{-\vec{k}-\sigma} \end{aligned} \tag{5.8}$$

which allows us to re-write the coherence factors to:

$$(uu' \mp vv')^2 = \frac{1}{2}\left(1 \mp \frac{\Delta^2}{EE'}\right) \tag{5.9}$$

$$(vu' \pm uv')^2 = \frac{1}{2}\left(1 \pm \frac{\Delta^2}{EE'}\right) \tag{5.10}$$

where Eq. 5.9 is for the scattering of quasi-particles and Eq. 5.10 is for the creation and annihilation of quasi-particles. By reversing the sign for Eq. 5.10, the two equations can be combined to rewrite the coherence factors as:

$$C_{\mp} = \frac{1}{2}\left(1 \mp \frac{\Delta^2}{EE'}\right) \tag{5.11}$$

Where the choice of $\mp$ is determined by the nature of the interaction. C_- is used when an interaction has even time reversal symmetry and C_+ is used when an interaction has odd time reversal symmetry. The spin flip process interaction responsible for spin-lattice relaxation is odd in time reversal symmetry and therefore C_+ is used.

The spin-lattice relaxation rate in the superconducting state is determined by the scattering of quasiparticles since the energy scale associated with creation and annihilation is much higher than the energy gap between nuclear spin states. This interaction and the corresponding spin-lattice relaxation rate in the superconducting state α_s is given by the following:

$$\alpha_s \propto |B|^2 \int_{-\infty}^{\infty} C_+(E, E') N_{BCS}(E) f(E) N_{BCS}(E')(1 - f(E'))dE \tag{5.12}$$

where $|B|^2$ is the hyperfine coupling of the nuclear spins and the electrons, $C_+(E, E')$ is the coherence factor from Eq. 5.11, $N_{BCS}(E)$ is the density of states in the superconducting state, and f(E) is the Fermi distribution function. Eq. 5.12 can be reduced when we consider that we only care about scattering between states that are separated by the same energy as the nuclear spin states $E' - E = \hbar\omega$:

$$\alpha_s \propto |B|^2 \int_{-\infty}^{\infty} N_{BCS}(E) N_{BCS}(E + \hbar\omega)[f(E) - f(E + \hbar\omega)]dE \tag{5.13}$$

In the normal state for a metal the relaxation rate is given by [68]:

$$\alpha_n \propto |B|^2 N_n^2(E_f)T \tag{5.14}$$

taking the ratio with Eq. 5.13 and using Eq. 5.3 for the density of states ratio, we can compare the relaxation rate in the superconducting state to the normal state given by [41]:

$$\frac{\alpha_s}{\alpha_n} = 2\int_{\Delta}^{\infty} \frac{E(E+\hbar\omega)+\Delta^2}{\sqrt{(E^2-\Delta^2)[(E+\hbar\omega)^2-\Delta^2]}}[f(E)-f(E+\hbar\omega)]dE \tag{5.15}$$

This can be further reduced when considering that the energy between the nuclear spin states $\hbar\omega$ is much smaller than the gap Δ and E such that $E+\hbar\omega \approx E$. By taking the limit of Eq.5.15 as $\hbar\omega \to 0$ one arrives at:

$$\frac{\alpha_s}{\alpha_n} = 2\int_{\Delta}^{\infty} \frac{E^2+\Delta^2}{(E-\Delta)(E+\Delta)}\left(-\frac{\partial f}{\partial E}\right)dE \tag{5.16}$$

Even without fully evaluating this integral in Eq. 5.16, we can see that there is a logarithmic divergence as $E \to \Delta$. This results in an enhancement of the spin-lattice relaxation rate just below T_c and is responsible for the Hebel-Slichter resonance peak [23]. Deeper in the superconducting state at lower temperatures, Eq. 5.16 results in the relaxation rate decreasing exponentially with $\alpha_s \propto \exp\left(-\frac{\Delta}{k_B T}\right)$ [24]. This can be useful in measuring the size of the superconducting gap of a BCS superconductor from the temperature dependence of the spin-lattice relaxation rate deep in the superconducting state.

Using Eq. 5.16 to estimate the size of the Hebel-Slichter peak results in an overestimation of the singularity at $E = \Delta$. In real systems, $\hbar\omega$ is not zero and there can be anisotropies in the gap due to disorder in the crystal lattice and the lifetime of the quasiparticles must also be considered. This is accounted for by the convolution of a breadth function with the density of states. Hebel and Slichter suggest a rectangular breadth function with height $\frac{1}{2\delta E}$

and width $2\delta E$ to achieve this [24].

Furthermore, it can be useful to rewrite Eq. 5.16 to separate the BCS density of states from the density of states of the quasiparticles due to the coherence terms $M_{BCS}(E)$ which gives [15]:

$$\frac{\alpha_s}{\alpha_n} = \frac{2}{k_B T}\int_{\Delta}^{\infty} \frac{N_{BCS}^2(E) + M_{BCS}^2(E)}{N_n^2(E_f)}\left(-\frac{\partial f}{\partial E}\right)dE \tag{5.17}$$

This new form allows for the introduction of a broadening term into the imaginary component of the density of states to replace the breadth function to correct the overestimation of the divergence at $E = \Delta$.

5.2.2 non-BCS superconductors

For non-BCS superconductors that do not have a nodeless isotropic gap, such as a d-wave superconductor, the $\mathbf{k}$ dependence of the gap and the presence of points where the gap vanishes result in the suppression of the HS peak. The ratio of the relaxation rate in the superconducting state and normal state in Eq. 5.17 for a d-wave superconductor is given by:

$$\frac{\alpha_s}{\alpha_n} = \frac{2}{k_B T}\int_{\Delta}^{\infty} \frac{N_{dsc}^2(E)}{N_n^2(E_f)}\left(-\frac{\partial f}{\partial E}\right)dE \tag{5.18}$$

with $N_{dsc}(E)$ being a new density of states in the superconducting state for a d-wave superconductor. Unlike the BCS superconducting gap, the d-wave superconducting gap is $\vec{k}$ dependent with nodes on the Fermi surface where the gap goes to zero. The nodes reduce the divergence at $E = \Delta$ and cause the low energy density of states to become linear in energy. This results in the absence of a Hebel-Slichter peak below T_c and a change to the temperature dependence of the relaxation rate at low temperatures [15]. Unlike the exponential temperature dependence of the relaxation rate at temperatures well below T_c for a BCS superconductor, a d-wave superconductor has a T^3 dependence, although deviations can occur due to impurities in the crystal which can contribute a residual density of states.

The Hebel-Slichter peak can also be suppressed in s-wave superconductors with strong electron-phonon coupling. Anisotropies in the superconducting gap can also result in a suppression of the Hebel-Slichter peak [69, 70].

The absence of a Hebel-Slichter peak, therefore, needs to be carefully analyzed with additional measurements such as the temperature dependence of the relaxation rate at low temperatures before determining the gap symmetry. Furthermore, although experimentally the HS peak seems to be absent on most unconventional superconductors, the exact origin is still an open question.

5.2.3 INT Triplet Model

Just as the absence of a Hebel-Slichter peak needs to be more carefully analyzed before drawing further conclusions, the presence of a Hebel-Slichter peak should also be explored carefully. We will now explore the case for a novel internally antisymmetric, non-unitary, triplet (INT) state that is fully gapped with s-wave symmetry in momentum space, antisymmetric in the band channel, and symmetric in spin space with triplet pairing [21]. The following calculation of the spin-lattice relaxation in the INT model is based on work by our theoretical collaborator, Dr. Rahul Hingorani with the full derivation given in Appendix C. This model is defined by the BdG Hamiltonian:

$$H_{BdG} = \sum_{\mathbf{k}} \Psi_{\mathbf{k}}^{\dagger} H(\mathbf{k}) \Psi(\mathbf{k}) \tag{5.19}$$

$$\Psi_{\mathbf{k}} = \left(a_{\mathbf{k}\uparrow}, b_{\mathbf{k}\uparrow}, a_{\mathbf{k}\downarrow}, b_{\mathbf{k}\downarrow}, a^{\dagger}_{-\mathbf{k}\uparrow}, b^{\dagger}_{-\mathbf{k}\uparrow}, a^{\dagger}_{-\mathbf{k}\downarrow}, b^{\dagger}_{-\mathbf{k}\downarrow} \right)$$

where

$$H(\mathbf{k}) = \begin{bmatrix} h_0(\mathbf{k}) & \hat{\Delta} \\ \hat{\Delta}^{\dagger} & -h_0(\mathbf{k}) \end{bmatrix} \tag{5.20}$$

and

$$h_0(\mathbf{k}) = \mathbb{1}_2 \otimes (w_{\mathbf{k}} \cdot \mathbf{k}\mathbb{1}_2 + \gamma_{\mathbf{k}} \cdot \mathbf{k}\tau_x) \tag{5.21}$$
$$\Delta = (\mathbf{d} \cdot \sigma) i\sigma_y \otimes i\tau_y$$

where $h_0(\mathbf{k})$ describes a Dirac dispersion from [53] and Δ is the pairing potential combining the Pauli spin matrices of electrons from multiple bands with the triplet gap parameter $\mathbf{d}$. In this model, the dependence on $\mathbf{k}$ reduces to only the component of $\mathbf{k}$ perpendicular to the Fermi surface, as reflected in the dispersion relation and the resulting coherence factors. It is also worth noting that the analogous model in [21] contains an additional τ_z term in $h_0(\mathbf{k})$, which introduces an intrinsic energy splitting between the a and b bands. Here, this term has been set to zero, while the τ_x term, taken to be momentum independent in [21], is instead assigned a linear $\mathbf{k}$ dependence to produce the Dirac-like dispersion described above. Furthermore, the superconducting order parameter is non-unitary, giving rise to a condensate with finite spin polarization, $\mathbf{q} = 2i\mathbf{d} \times \mathbf{d}^*$ [54]. We consider several choices for the pairing vector, $\mathbf{d} = \Delta_0 \boldsymbol{\eta}$, where $\boldsymbol{\eta}$ is a complex unit vector:

(I) $\mathbf{d}_r = \frac{\Delta_0}{\sqrt{1+r^2}}(r, i, 0)$, where r is a real parameter and $\mathbf{q} \propto \frac{r}{1+r^2}\hat{z}$, and $\mathbf{d}_a = \frac{\Delta_0}{\sqrt{1+a^2}}(a, i, 0)$ with $\mathbf{q} \propto \frac{a}{1+a^2}\hat{z}$;

(II) $\mathbf{d}_z = \Delta_0(0, 0, 1)$, for which $\mathbf{q} = 0$;

(III) $\mathbf{d}^{xy}\theta = \frac{\Delta_0}{\sqrt{2}}(1 + i\cos\theta\eta, , i\sin\theta_\eta, , 0)$, with $\mathbf{q} \propto \sin\theta_\eta, \hat{z}$;

(IV) $\mathbf{d}^{yz}\theta = \frac{\Delta_0}{\sqrt{2}}(0, , i\sin\theta\eta, , 1 + i\cos\theta_\eta)$, with $\mathbf{q} \propto \sin\theta_\eta, \hat{x}$.

The first two cases correspond to the symmetry-allowed irreducible representations of a single-band superconductor with weak spin-orbit coupling [1]. In particular, increasing r from zero introduces time-reversal symmetry breaking (TRSB), resulting in a finite $\boldsymbol{\omega} = i(\boldsymbol{\eta} \times \boldsymbol{\eta}^*)$. More generally, the parameter θ_η determines the relative orientation of the real and imaginary components of $\mathbf{d}$ and therefore controls the degree of non-unitarity.

The two superconducting gaps, $\Delta_{1,2}$, are given by:

$$\Delta_{1,2} = \Delta_0 \sqrt{1 - (\gamma_k/w_k)^2} \sqrt{1 \pm |\boldsymbol{\omega}|}. \tag{5.22}$$

A complex order parameter with either $r \neq 0$ or non-parallel real and imaginary components is required for this model to support two distinct superconducting gaps. The Bogoliubov quasiparticle excitations take the form

$$\begin{aligned} \alpha_{\mathbf{k}s} &= v_{\mathbf{k}s}(a_{\mathbf{k}s} - b_{\mathbf{k}s}) - u^*_{\mathbf{k}s}(a^\dagger_{-\mathbf{k}s} + b^\dagger_{-\mathbf{k}s}) \\ \beta^\dagger_{-\mathbf{k}s} &= u_{\mathbf{k}s}(a_{\mathbf{k}s} - b_{\mathbf{k}s}) + v_{\mathbf{k}s}(a^\dagger_{-\mathbf{k}s} + b^\dagger_{-\mathbf{k}s}), \end{aligned} \tag{5.23}$$

where the coherence factors $u_{\mathbf{k}s}$ and $v_{\mathbf{k}s}$ are obtained from the eigenvectors of $\mathcal{H}_{\mathrm{BdG}}$. These quasiparticle operators define a superconducting ground state characterized by equal-spin pairing, in an appropriate basis, which is enabled by the interband pairing terms present in the BdG Hamiltonian. Combining this with the S^+ term of the hyperfine Hamiltonian and using Fermi's golden rule, one can compute the scattering amplitudes and in turn the relaxation rate T_1^{-1} [64].

$$T_1^{-1} \sim \sum_{\substack{\mathbf{k},\mathbf{k'},s,s' \\ i,j=\alpha,\beta}} |A_{is' \to\, js}(\mathbf{k},\mathbf{k'})|^2 g_{ij}(\mathbf{k},\mathbf{k'},s,s'). \tag{5.24}$$

Here, $A_{\alpha/\beta,s' \to \alpha/\beta,s}(\mathbf{k},\mathbf{k}')$ denotes the scattering amplitude between the two types of quasiparticle states. The function $g_{ij}(\mathbf{k},\mathbf{k}',s,s') = f_{j,\mathbf{k},s}\,(1 - f_{i,\mathbf{k}',s'})\,\delta(E_{i,\mathbf{k}',s'} - E_{j,\mathbf{k},s} - \hbar\omega_N)$ accounts for the quasiparticle occupation factors and energy conservation, where $f_{\epsilon\mathbf{k}s}$ is the Fermi-Dirac distribution for a quasiparticle with energy $E_{\epsilon\mathbf{k}s}$, and ω_N is the nuclear resonance frequency. The momentum sums over $\mathbf{k}$ and $\mathbf{k}'$ can be transformed into energy integrals

through the density of states. Additionally, we incorporate the temperature dependence of Δ_0 in Eq. 5.22 using the solution of the self-consistent gap equation from conventional singlet BCS theory [14]. The presence or absence of a Hebel-Slichter peak in the temperature dependence of the relaxation rate T_1^{-1} for this model is strongly dependent on the difference in energy between the two gaps and the orientation of the **d** vector relative to the quantization axis of the nuclear spins [64].

5.2.4 Two-Gap Singlet Model

Another model to consider is the two-band singlet model which is proposed in ref. [73]. This uses a matrix similar to Eq. 5.20 with the Δ term modified to describe singlet pairing of the electrons:

$$\begin{aligned} \Delta &= -\sigma_y \otimes \Delta_0 \left(\cos(\theta_b)\mathbb{1}_2 + \sin(\theta_b)\tau_x\right) \\ \Delta_\pm &= \Delta_0\sqrt{1 \pm \sin(2\theta_b)} \end{aligned} \tag{5.25}$$

with θ_b responsible for the difference in the two gaps. This model also produces two species of Bogoliubov excitations similar to 5.23:

$$\begin{aligned} \alpha(\beta)_{\mathbf{k}\uparrow} &= u_{\mathbf{k}\alpha(\beta)}\left(a_{\mathbf{k}\uparrow} \pm b_{\mathbf{k}\uparrow}\right) + v_{\mathbf{k}\alpha(\beta)}(a^\dagger_{-\mathbf{k}\downarrow} \pm b^\dagger_{-\mathbf{k}\downarrow}) \\ \alpha(\beta)^\dagger_{-\mathbf{k}\downarrow} &= -u^*_{\mathbf{k}\alpha(\beta)}(a^\dagger_{-\mathbf{k}\downarrow} \pm b^\dagger_{-\mathbf{k}\downarrow}) + v_{\mathbf{k}\alpha(\beta)}(a_{\mathbf{k}\uparrow} \pm b_{\mathbf{k}\uparrow}), \end{aligned} \tag{5.26}$$

with $u_{\mathbf{k}\gamma}$ and $v_{\mathbf{k}\gamma}$ determined by diagonalizing the Hamiltonian. The scattering amplitudes are then computed again using the new quasiparticle excitations to obtain Eq.5.24 for the two-band singlet case.

This predicts a large Hebel-Slichter peak below T_c which needs to be suppressed with a broadening term to account for real systems as discussed at the end of section 5.2.1.

Chapter 6

NMR and NQR in the Normal State of $LaNiGa_2$

Unconventional superconductivity, including triplet superconductivity, is conventionally associated with strong electronic correlations which are present in the normal state. Therefore, it is essential to first explore the strength of the electronic correlations in the normal state of $LaNiGa_2$. This chapter will present the NMR and NQR studies performed in the normal state of $LaNiGa_2$.

For the NMR measurements, three single crystals were aligned to form a mosaic with dimensions $1.3 \times 0.5 \times 0.5$ mm^3. The mosaic was mounted inside an NMR coil and placed in an external magnetic field within a cryostat. The resonance frequencies were determined by the Hamiltonian

$$\mathcal{H} = \gamma\hbar\hat{\mathbf{I}} \cdot (1 + \mathbf{K}) \cdot \mathbf{H}_0 + \frac{h\nu_{zz}}{6}\left[3\hat{I}_z^2 - \hat{I}^2 + \eta(\hat{I}_x^2 - \hat{I}_y^2)\right], \tag{6.1}$$

where γ is the nuclear gyromagnetic ratio, h ($\hbar$) is the Planck (reduced Planck) constant, $\hat{\mathbf{I}}$ is the nuclear spin angular momentum operator, $\mathbf{H}0$ is the applied magnetic field, and $\mathbf{K}$ is the NMR shift tensor. The EFG asymmetry parameter is defined as $\eta = (\nu xx - \nu_{yy})/\nu_{zz}$, where

$\nu_{\alpha\alpha} = 3eQV_{\alpha\alpha}/2I(2I-1)h$ are the principal components of the electric field gradient (EFG) tensor $V_{\alpha\beta}$. Here, α and β denote the principal axes of the EFG tensor, I is the nuclear spin quantum number, and Q is the nuclear quadrupole moment. The NMR parameters for each isotope are summarized in Table 6.1.

NMR spectra were obtained by integrating the spin-echo intensity as a function of frequency at either $\mu_0 H_0 = 11.7286$ T or 7.0 T and at a temperature of 5 K, with the applied field oriented both parallel and perpendicular to the crystallographic b axis. The Knight shift and EFG tensor components, $K_{\alpha\alpha}$ and $\nu_{\alpha\alpha}$, were extracted by fitting the complete spectra to numerical solutions obtained from exact diagonalization of Eq. 6.1 for different orientations of $\mathbf{H}_0$.

Zero-field NQR spectra were measured at 4K by integrating the Fourier transform of the spin-echo intensity as a function of frequency.

Table 6.1: NMR parameters of the nuclei measured

Isotope	^{139}La	^{69}Ga	^{71}Ga
Natural abundance	99.1%	60%	40%
Nuclear spin I	7/2	3/2	3/2
$\gamma/2\pi$ (MHz/T)	6.0146	10.219	12.985
Q (barn)	0.21	0.178	0.112

6.1 ^{139}La NMR Spectrum

We begin with the ^{139}La NMR spectrum measured in a $LaNiGa_2$ single crystal at 5 K and $H_0 = 11.7285$ T. Because ^{139}La is a $I = 7/2$ nucleus, seven transitions in the NMR spectrum are expected.

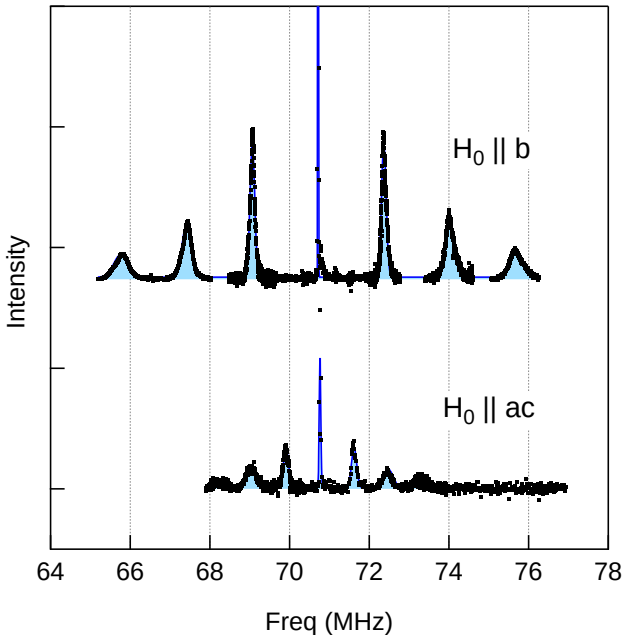


Figure 6.1: The ^{139}La spectrum in $LaNiGa_2$ at 5K with an external field $H_0 = 11.7285$ tesla oriented parallel and perpendicular to the b-axis with the blue areas corresponding to a fit to the results of exact diagonalization of the Hamiltonian.

The sharp central transition and well resolved peaks indicate the high quality of the samples. Seven transitions are clearly resolved. We can also see that the b-axis is the principal axis for this nucleus and the quadrupolar peaks being close to exactly half with the field perpendicular to the b-axis indicates that the asymmetry parameter η is small.

6.2 ^{69}Ga NMR Spectrum

The ^{69}Ga spectrum was taken using a goniometer probe allowing for the continuous measurement of the angular dependence of the spectrum.

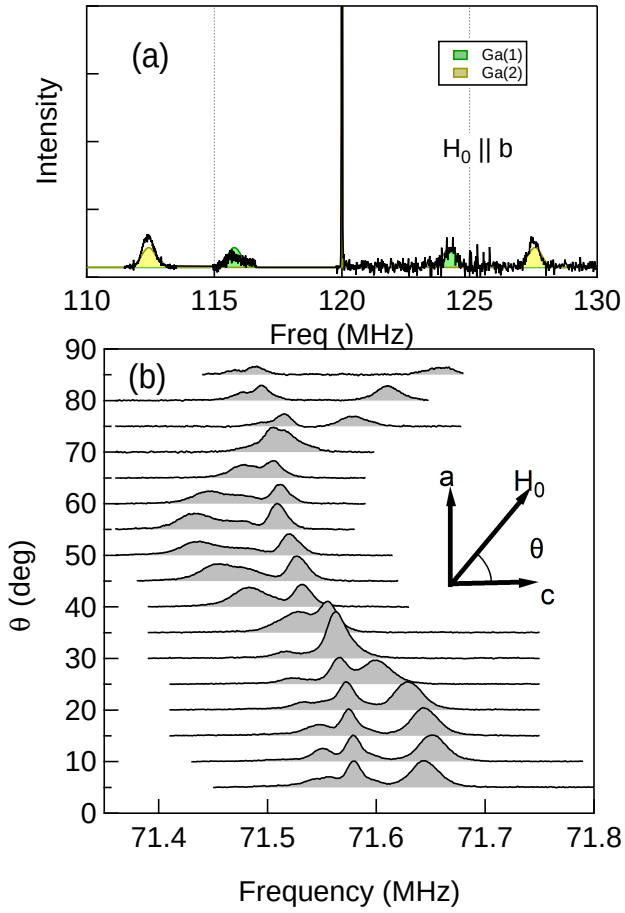


Figure 6.2: Figure (a) shows the ^{69}Ga spectrum at 2.7K with $H_0 = 11.7285$T for both Ga sites in $LaNiGa_2$ along with the fit to exact diagonalization shown in green and yellow. Figure (b) shows the angular dependence of the central transition in the ac plane at 2.7K and 7.0T

^{69}Ga has $I = 3/2$ and should have three transitions, one central transition and two satellites. In Figure 6.2(a) there appears to be one central transition and four satellite transitions. This is due to the fact that there are two different Ga sites in $LaNiGa_2$ with different EFGs resulting in the four satellites and the central transitions are overlapping. The angular dependence shown in the ac-plane in Figure 6.2 (b) reveals the two distinct transitions for the two sites. There appears to be an additional peak of unknown origin which does not appear to have any satellite transitions and its source remains unknown.

In addition, the angular dependence of the satellites for the Ga(2) site was also measured

and used to experimentally extract the values for the EFG tensor:

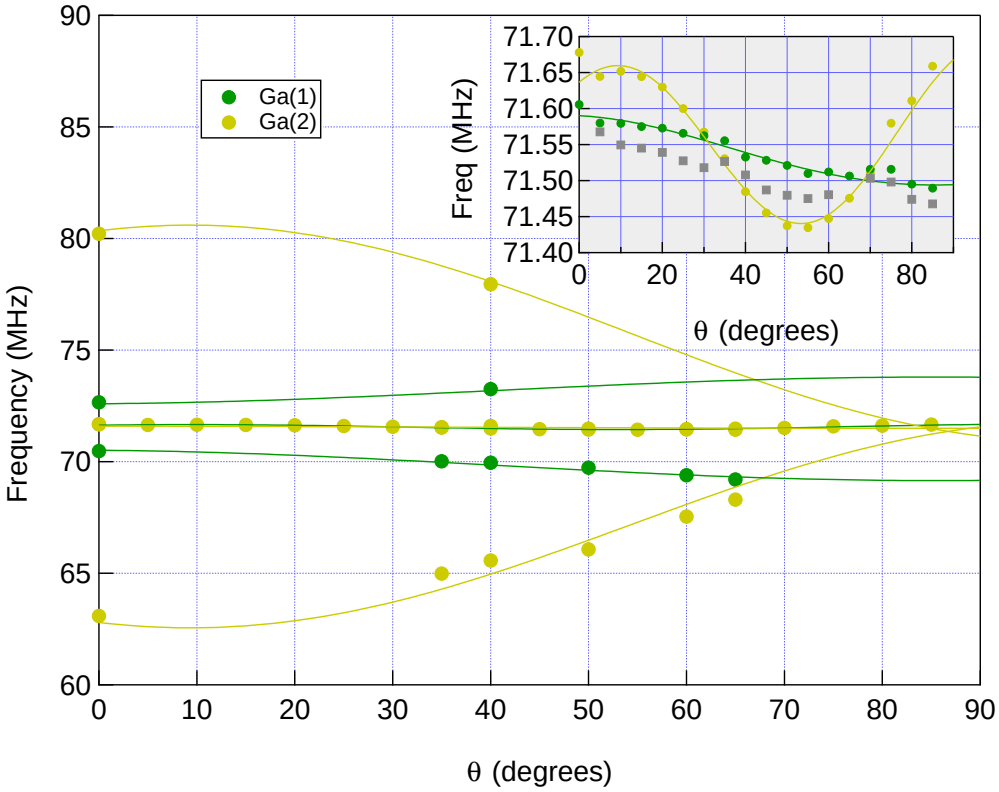


Figure 6.3: The angular dependence of the ^{69}Ga transitions including the satellites. The lines are fits done to extract the EFG tensor elements ν_{aa} and ν_{cc} and the inset shows a zoomed view to emphasize the angular dependence of the central transition.

In addition to these spectra, X-ray Photoemission Spectroscopy studies were also performed, the results of which can be found in the Appendix B.

6.3 NQR Spectrum

In addition to the single crystal measurements, the NQR spectrum of a powdered sample was also measured at 4K.

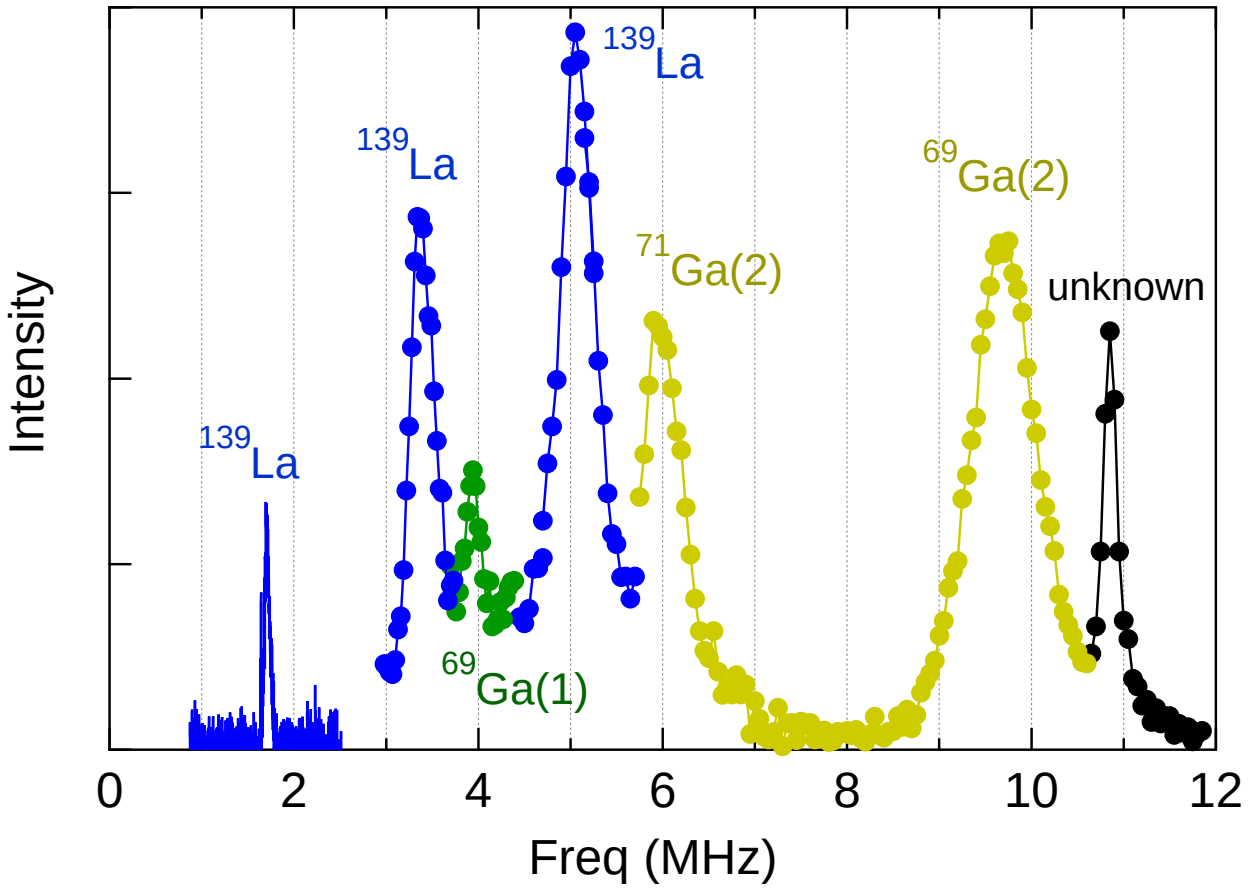


Figure 6.4: The full NQR spectrum of $LaNiGa_2$ measured at 4K excluding the ^{71}Ga(2) transition. The blue corresponds to ^{139}La, the green to Ga(1) and yellow to Ga(2).

We expect three transitions for the spin 7/2 ^{139}La and one transition for the spin 3/2 ^{69}Ga and ^{71}Ga for the two sites, totaling seven peaks in the full spectrum. The ^{71}Ga(2) transition at 2.5MHz was excluded due to the limitations in the tuning range of the NMR tank circuit described in Sec. 3.1. The third transition of ^{139}La was the primary focus of the studies performed in the superconducting state.

6.4 Electric Field Gradient

Figure 6.4 shows the NQR spectrum measured at 4 K. Although several resonance peaks are observed, their site assignments are not immediately apparent. To identify the La resonances,

we first measured the ^{139}La NMR spectrum in an applied magnetic field (Fig.6.1), which exhibits seven transitions separated by $\nu_{\alpha\alpha}$. These splittings uniquely determine the electric field gradient (EFG) tensor at the La site, allowing us to identify the three La resonances (shown in blue) in the NQR spectrum. The fitted EFG tensor elements are listed in Table 6.2. The principal EFG axis, corresponding to the largest eigenvalue of the tensor, is oriented along the b axis. The asymmetry parameter is remarkably small, $\eta = 0.04 \pm 0.01$, indicating an EFG that is nearly axially symmetric. Consequently, the three La resonances in Fig. 6.4 closely correspond to the $I_z = \pm 1/2 \leftrightarrow \pm 3/2$, $I_z = \pm 3/2 \leftrightarrow \pm 5/2$, and $I_z = \pm 5/2 \leftrightarrow \pm 7/2$ transitions, in order of increasing frequency. The measured La NQR frequencies are comparable to those reported for $LaNiC_2$, a structurally similar but non-centrosymmetric compound [32].

The remaining resonances arise from the two crystallographically distinct Ga sites [Ga(1) and Ga(2) in Fig. 4.1]. Each site contains the two spin-3/2 isotopes, ^{69}Ga and ^{71}Ga, giving a total of four $I_z = \pm 1/2 \leftrightarrow \pm 3/2$ NQR transitions. To determine the EFG tensors at these sites, we performed angle-dependent NMR measurements in an applied magnetic field. The resulting EFG parameters are summarized in Table 6.2. Both Ga sites exhibit large asymmetry parameters, reflecting the orthorhombic symmetry of their local electronic environments. While the principal EFG axis at the Ga(1) site is aligned along the b axis, as for the La site, the principal axis at the Ga(2) site is oriented along the c axis.

To assign the observed Ga resonances to their respective crystallographic sites and isotopes, we compare the experimental EFG tensors with density functional theory (DFT) calculations, also listed in Table 6.2. The calculations correctly reproduce the orientations of the principal EFG axes, with the La and Ga(1) sites aligned along b and the Ga(2) site along c, enabling an unambiguous assignment. We identify the lower-frequency resonance, with $^{69}\nu_Q = 3.94 \pm 0.01$ MHz, as originating from the Ga(1) site, while the higher-frequency resonance at $^{69}\nu_Q = 9.70 \pm 0.01$ MHz is assigned to the Ga(2) site. Overall, the calculated EFG values agree with

experiment to within approximately 20%.

Table 6.2: Measured and DFT-calculated electric field gradient tensor components, quadrupolar frequencies, and asymmetry parameters for the inequivalent Ga and La sites.

Site	ν_{aa} (MHz)	ν_{bb} (MHz)	ν_{cc} (MHz)	ν_Q (MHz)	η
Ga(1) measured	-2.61 ± 0.01	3.86 ± 0.01	-1.25 ± 0.01	3.94 ± 0.01	0.35 ± 0.01
Ga(1) computed	-1.091	4.332	-3.241	4.506	0.496
Ga(2) measured	-0.78 ± 0.01	-7.99 ± 0.01	8.77 ± 0.01	9.70 ± 0.01	0.82 ± 0.01
Ga(2) computed	-0.060	-7.011	7.072	8.131	0.983
La measured	-0.86 ± 0.01	1.65 ± 0.01	-0.80 ± 0.01	1.71 ± 0.01	0.04 ± 0.01
La computed	-0.948	1.907	-0.959	1.907	0.005

In addition to these resonances, the NQR spectrum in Fig. 6.4 contains a weaker peak near 11 MHz whose origin remains uncertain. Its frequency is close to that reported for elemental ^{69}Ga metal [27], although it may also originate from a secondary phase such as LaNiGa, which is close to the flux composition and has previously been detected by powder x-ray diffraction [2]. The lower-frequency ^{71}Ga resonance near 2.5 MHz could not be measured because it lies outside the tuning range of the resonance tank circuit.

6.5 Stoner enhancement factor

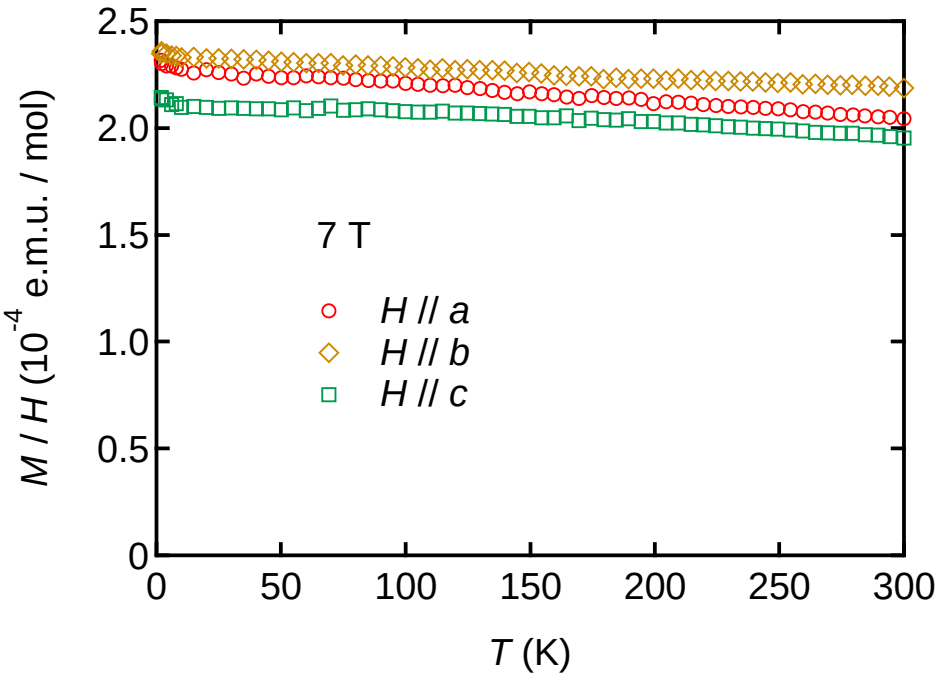


Figure 6.5: The susceptibility of an aligned mosaic of single crystals of $LaNiGa_2$ as a function of temperature with the magnetic field applied along a, b, and c axes.

Figure 6.5 shows the DC magnetic susceptibility of a mosaic of $LaNiGa_2$ single crystals measured in an applied magnetic field of 7T oriented along the crystallographic a, b, and c axes. The susceptibility is nearly temperature independent over the measured range, consistent with Pauli paramagnetic behavior. Averaging over the full temperature range yields susceptibilities of 2.17×10^{-4}, 2.26×10^{-4}, and 2.05×10^{-4} e.m.u./mol along the a, b, and c axes, respectively.

The measured temperature-independent susceptibility, χ_{meas}, consists of two primary contributions: the Pauli paramagnetic response from conduction electrons, χ_P, and the diamagnetic response of the atomic cores, χ_D. According to density functional theory (DFT) calculations, the Ni $3d$ states in LaNiGa2 are fully occupied [53]. Therefore, the Langevin diamagnetic contribution of Ni with a $3d^{10}$ electronic configuration can be estimated by ex-

trapolating from ions with equivalent $3d^{10}$ configurations, including Cu^{+}, Zn^{2+}, Ga^{3+}, and Ge^{4+} [43]. This gives $\chi D, \mathrm{Ni}^{3d^{10}} = -19 \times 10^{-6}$ e.m.u./mol. For La, we use the tabulated value $\chi_{D,\mathrm{La}^{3+}} = -20 \times 10^{-6}$ e.m.u./mol [3].

To determine the Ga contribution to the core diamagnetism, we first used X-ray photoemission spectroscopy (XPS) to establish the Ga valence state. Appendix B shows two distinct components corresponding to neutral Ga(0) (binding energy, BE = 1116.4 eV) [61, 79] and Ga(III) (BE = 1117.8 eV) [61, 79]. The Ga(III) component is substantially reduced after cleaving the sample compared with the air-exposed surface [Fig. B.1(a,b)], while its binding energy agrees well with reported values for Ga_2O_3 [61, 79]. Furthermore, measurements using an Ag L-α in Appendix B show a change in the relative peak intensities consistent with enhanced bulk sensitivity, indicating that the Ga(III) component originates from a surface oxide layer rather than the bulk material [62]. We therefore conclude that Ga is predominantly in the neutral oxidation state in bulk LaNiGa2. Using the corresponding Langevin diamagnetic contribution, $\chi D, \mathrm{Ga}^{0} = -32 \times 10^{-6}$ e.m.u./mol [43], we obtain a total core diamagnetic susceptibility of $\chi_D = -10.3 \times 10^{-5}$ e.m.u./mol for $LaNiGa_2$.

The Pauli susceptibility of a free-electron gas is related to the Sommerfeld coefficient by

$$\chi_P = \left(\frac{3\mu_0 \mu_B^2 10^6}{4\pi^3 k_B^2} \right) \gamma_S, \tag{6.2}$$

where γ_S is the Sommerfeld coefficient. Using $\gamma_S = 14.1$ mJ·mol^{-1}K^{-2} [2], we obtain $\chi_P = 1.93 \times 10^{-4}$ e.m.u./mol. The Stoner enhancement factor, Z, can then be extracted from the measured susceptibility using

$$\frac{1}{1-Z} = \frac{\chi_{\mathrm{meas}} - \chi_D}{\chi_P}. \tag{6.3}$$

The resulting values are $Z = 0.40$, 0.41, and 0.37 along the a, b, and c axes, respectively. These values are well below the Stoner instability limit ($Z = 1$) and are comparable to the estimated value for elemental copper, $Z = 0.26$, obtained using $\gamma_S = 0.505$ mJ·mol^{-1}K^{-2} [36]

and $\chi_0 = -14.85 \times 10^{-6}$ e.m.u./mol [43]. Therefore, the measured susceptibility shows no significant enhancement associated with ferromagnetic interactions.

6.6 Knight Shift and T_1

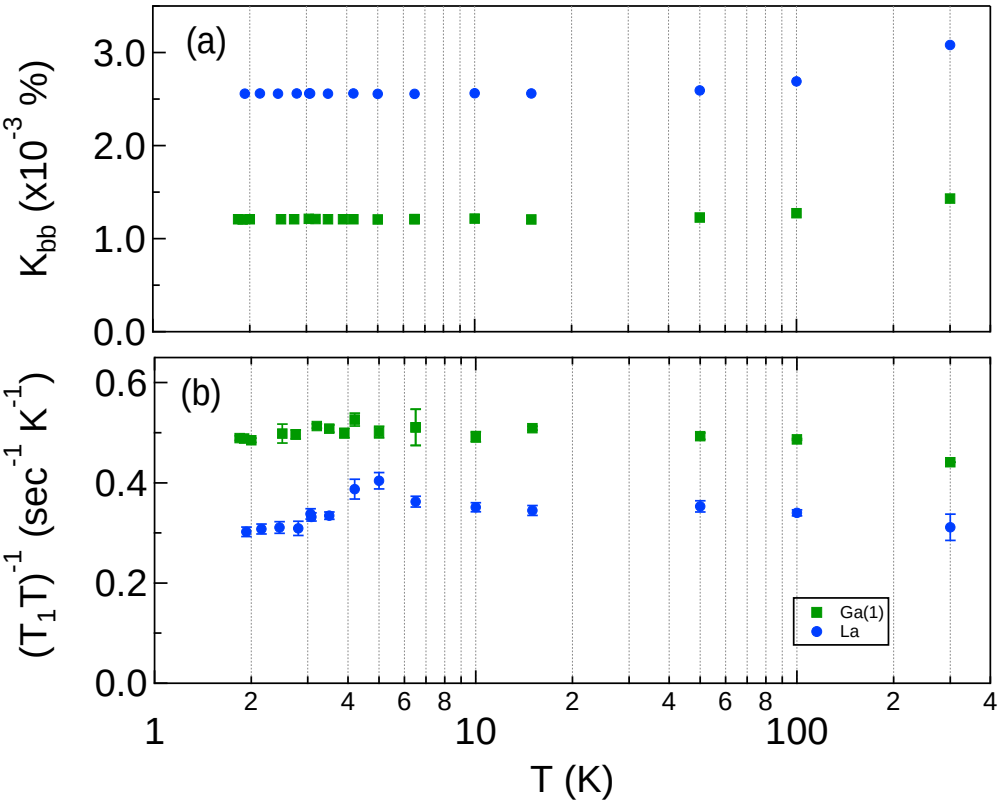


Figure 6.6: (a) and (b) show the temperature dependence of the Knight shift and spin-lattice relaxation rate divided by the temperature for ^{139}La and ^{69}Ga(1) with the magnetic field parallel to the b-axis.

Figure 6.6 (a) shows the temperature dependence of the magnetic Knight shift for ^{139}La and ^{69}Ga(1) along the b-axis. As discussed in section 2.2.1, the Knight shift arises from the interaction of the nuclear spins and the electronic system and is composed of both an orbital and spin component [68]. The components of the Knight shift can be separated by plotting the Knight shift vs the susceptibility in order to extract the spin component. This process

requires a temperature dependence of both the susceptibility and Knight shift and is not possible in this system since both are mostly temperature independent.

Figure 6.6 (b) shows the temperature dependence of the spin-lattice relaxation rate divided by the temperature $(T_1T)^{-1}$ for ^{139}La and ^{69}Ga(1) with respect to the b-axis. The spin-lattice relaxation rate is proportional to the density of states close to the Fermi level using a free electron approximation as shown in Eq. 2.40. The $(T_1T)^{-1}$ values for both ^{139}La and ^{69}Ga(1) are mostly temperature independent indicating that the free electron approximation is a good model and that the electronic correlations are weak. There is a slight enhancement of $(T_1T)^{-1}$ which indicates the possibility of some weak magnetic correlations. This behavior suggests the presence of dilute magnetic impurities that undergo spin freezing at low temperatures, although the bulk magnetic susceptibility shows no evidence of a Curie-like contribution associated with such impurities [19].

6.7 Korringa Relation

The Korringa relation, as discussed in section 2.3.1, is indicative of a conductor with spin-flip scattering between nuclear spins and electronic spins close to the Fermi surface [37]. For an isotropic Fermi-contact type interaction with only a single hyperfine coupling channel we expect Eq. 2.41, where $S_0 = (\gamma_e/\gamma_n)^2\hbar/(4\pi k_B)$, and $\gamma_{e,n}$ is the gyromagnetic ratio of the electron/nucleus.

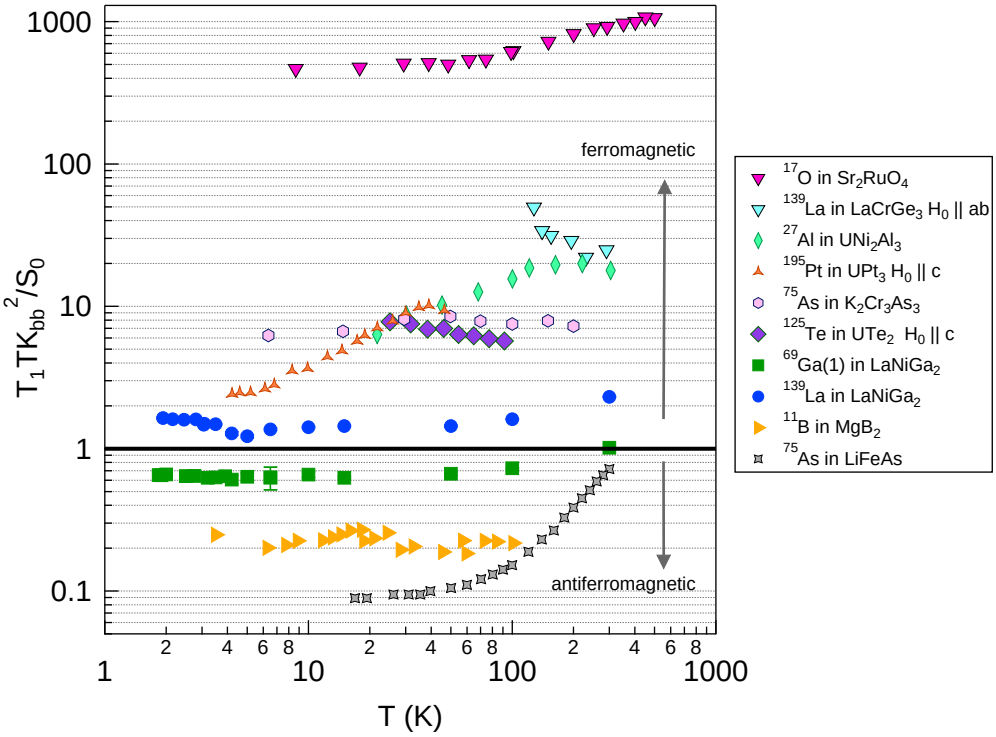


Figure 6.7: The Korringa ratio, T_1TK^2/S_0, versus temperature for $LaNiGa_2$ (for field along the b direction) compared with data for LiFeAs [34], MgB_2 [35], UTe_2 [77], UNi_2Al_3 [31], $LaCrGe_3$ [57], $K_2Cr_3As_3$ [82], UPt_3 [38], and Sr_2RuO_4 [28]

Figure 6.7 shows the Korringa ratio, $T_1TK_{bb}^2/S_0$, for the ^{139}La and ^{69}Ga(1) sites in $LaNiGa_2$ as a function of temperature, together with corresponding data for several materials for comparison. In principle, the spin Knight shift, $K_s = K_{bb} - K_o$, should be used rather than the total shift K_{bb}. However, because the orbital contribution K_o cannot be determined independently, we use the total Knight shift in the analysis due to the temperature independence of the shift. This approximation likely accounts for the deviation of the ratio from unity for the ^{69}Ga(1) and ^{139}La sites.

6.8 Summary

In the presence of exchange enhancements to the conduction electron spin susceptibility, the Korringa ratio can deviate substantially from unity [45,47]. For the idealized case of a single spherical Fermi surface, the magnitude of the Korringa ratio is directly related to the Stoner enhancement factor. As discussed at the end of section 2.3.1, a ratio greater than unity is indicative of dominant ferromagnetic spin fluctuations, whereas a ratio less than unity signals antiferromagnetic fluctuations. This trend is illustrated in Fig. 6.7 for several materials known to exhibit either ferromagnetic order or strong antiferromagnetic correlations, including Sr_2RuO_4, which exhibits time-reversal symmetry (TRS) breaking in the superconducting state, UPt_3, a candidate non-unitary spin-triplet superconductor, and $K_2Cr_3As_3$, which has been proposed to host chiral p-wave superconductivity [38, 40, 82]. Although none of these systems possesses a single spherical Fermi surface, $LaNiGa_2$ is qualitatively different, in that the Korringa ratio remains nearly temperature independent and close to unity for both the ^{139}La and ^{69}Ga sites.

Additional evidence for weak electronic correlations comes from the agreement between the measured electric field gradients and those obtained from density functional theory (DFT). In strongly correlated materials, the experimentally determined EFGs often differ substantially from band-structure calculations [33, 71]. In contrast, the DFT calculations for $LaNiGa_2$, which do not include explicit Coulomb interaction terms, reproduce the measured EFGs to within approximately 20%. This level of agreement suggests that electronic correlations are relatively weak in this compound.

In summary, our measurements provide no evidence for significant Stoner enhancement and indicate that spin fluctuations in $LaNiGa_2$ are weak. Consequently, the unconventional superconducting state, characterized by unequal equal-spin pairing gaps, is unlikely to be driven by the strong electronic correlations that are widely believed to underlie unconventional su-

perconductivity in many correlated materials. Instead, the topological band structure, which features symmetry-protected degenerate bands crossing the Fermi level, provides a natural mechanism for stabilizing equal-spin pairing gaps, as proposed in Refs. [2, 80].

Chapter 7

NQR in the Superconducting State of $LaNiGa_2$

Exploring the spin component of the Knight shift below T_c is one of the key ways to understand the spin state of the Cooper pairs. However, conventional NMR experiments could not be performed in $LaNiGa_2$ due to the small size of the upper critical field.

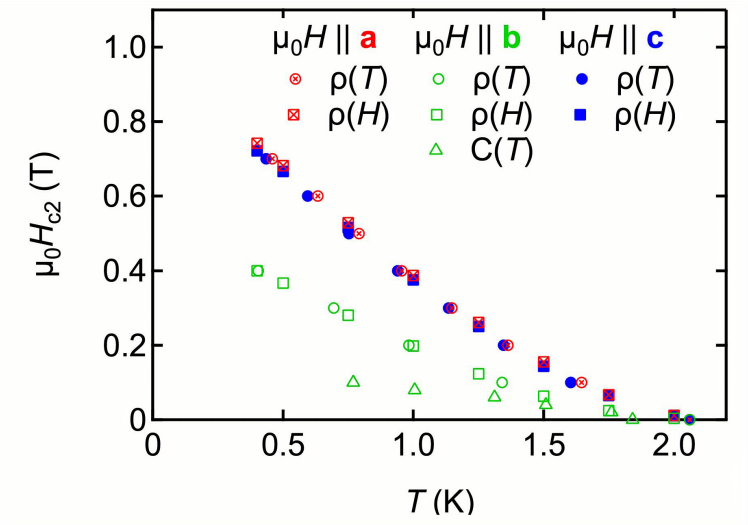


Figure 7.1: The upper critical field in $LaNiGa_2$ as a function of temperature and field orientation [2].

The superconducting state was therefore exclusively studied using NQR measurements of the spin-lattice relaxation rate T_1. All measurements were performed on a finely ground powder sample ($\approx 100mg$) in a top loading Qxford Instruments wet dilution refrigerator. The probe available had only one tuning capacitor which severely limited the tuning range of the NMR tank circuit. The process for inserting and removing the probe was also very time consuming, taking at least full day depending on the desired temperature. The decision was therefore made to focus on the highest NQR $3\nu_Q$ transition of ^{139}La at 5.06MHz as shown in figure 6.4. Although the Ga(2) sites had a higher frequency and signal intensity, their non-zero asymmetry parameter made them unsuitable as the results would be difficult to interpret due to the influence of additional components to the relaxation.

7.1 T_1

$LaNiGa_2$ has one crystallographic La site, shown in the inset of figure 7.2. Its zero-field resonances are determined by the quadrupolar Hamiltonian as discussed in section 2.2.3 with Eq. 2.24. ^{139}La is a spin $I = 7/2$ nucleus with a quadrupolar moment $Q \approx 0.200$ barns. The principal axis lies along the b direction with $\nu_{zz} = 1.65$MHz and $\eta = 0.04$ (Table 6.2). T_1 was measured using the inversion recovery method described in section 2.4.4 on the $3\nu_Q$ transition at 5.06MHz. The inversion recovery curve was fit to the $3\nu_Q$ transition for $I = 7/2$ with magnetic fluctuations:

$$M(t) = M_0(1 - 2f\sum_n A_n e^{-\alpha_n t/T_1}) \tag{7.1}$$

where M_0 is the magnetization at equilibrium and f is the inversion fraction. The summation is over three exponential terms with α_1=3, α_2 =10, and α_3 =21 with their respective relative contributions of A_1 =3/14, A_2 = 50/77, and A_3 = 3/22.

The measurements were performed with the sample fully immersed in the mixing chamber of the dilution refrigerator. T_1 was measured at several different power levels and pulse widths until the T_1 value saturated and we determined there was minimal influence of heating from the applied pulses with a power of 30W and $\pi/2$ pulse length of $30\mu s$. The temperature dependence of T_1^{-1} in Fig. 7.2, shows a clear enhancement in the superconducting state resulting in a Hebel-Slichter peak just below T_c.

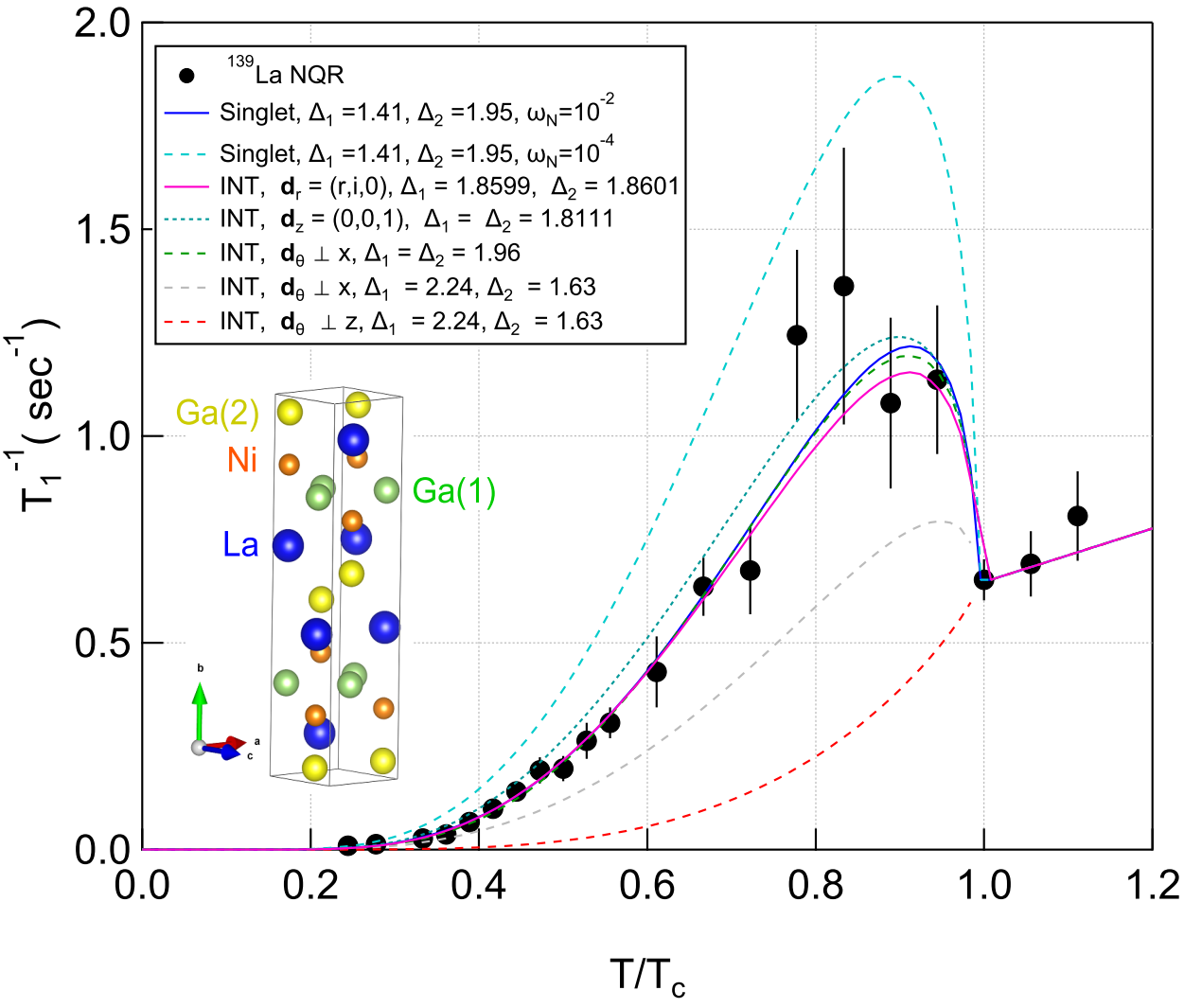


Figure 7.2: The ^{139}La T_1^{-1} as a function of temperature in the superconducting state of $LaNiGa_2$, with $T_c = 1.83$ K. The solid and dashed lines are calculations as discussed in sections 5.2 and 7.2, and the gap values, (Δ_1, Δ_2) and nuclear resonance frequency, ω_N, are given in units of k_BT_c.

There is a change in slope around $T_c/T \approx 3.5$ which can be seen in Fig. 7.3, suggesting the presence of multiple superconducting gaps. From the slopes, the gap values are estimated to be approximately $2\,k_B T_c$ and $< 1.0\,k_B T_c$. The change in slope could be due to an impurity band which can contribute to residual scattering at the lowest temperatures [15].

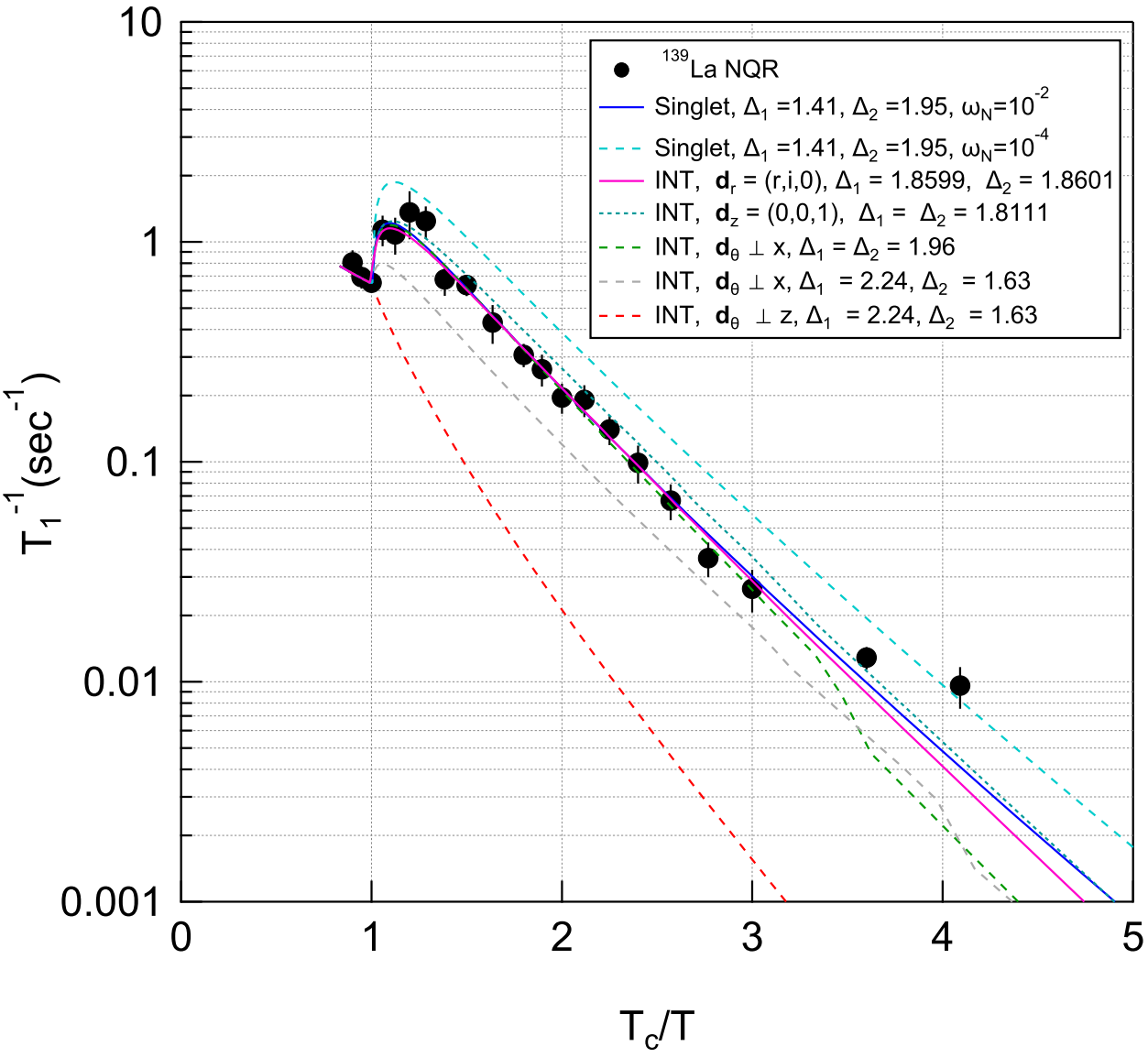


Figure 7.3: The ^{139}La T_1^{-1} relaxation rate as a function of inverse temperature, T_c/T, in the superconducting state. The solid and dashed curves represent calculated values as discussed in Sec. 5.2 and 7.2, with the superconducting gap values expressed in units of $k_B T_c$.

7.2 Hebel-Slichter Peak Discussion

The Hebel-Slichter peak was fitted with two different models for the superconducting state. The first was the INT model as described in Sec. 5.2.3 and the second a two-gap singlet model described in Sec. 5.2.4.

We begin with the INT model as shown in Fig. 7.2. In this model, the quasiparticle scattering rates are strongly suppressed when the two superconducting gaps have different magnitudes, since energy conservation restricts scattering processes between quasiparticles associated with the two gaps. The nuclear resonance frequency is set to $\hbar\omega_N/k_BT_c = 10^{-4}$ and 10^{-6} for the $\mathbf{d} \perp \mathbf{x}$ and $\mathbf{d} \perp \mathbf{z}$ cases, respectively, with no additional broadening included. The model reproduces the coherence peak well when the two gaps are equal. However, this state is unitary and therefore not time-reversal symmetry breaking (TRSB). When TRSB is introduced and the two gaps have different magnitudes, the calculated relaxation rate depends on the orientation of the equal-spin pairing axis relative to the nuclear spin quantization axis. In the limit of weak spin-orbit coupling, the spin pairing axis is not constrained to the crystallographic axes. If $\mathbf{d}$ lies in the xy plane, parallel to the nuclear spin quantization axis, the spin-flip scattering process produces an immediate downturn in T_1^{-1}, precluding the Hebel-Slichter (HS) peak. In contrast, when the equal-spin pairing axis is oriented away from the nuclear spin quantization axis, with $\mathbf{d}$ lying in the yz plane, a weak HS peak can develop through scattering processes that do not require transitions between the two gaps; see Appendix C for further discussion.

The HS peak can be enhanced by reducing the nuclear resonance frequency to an anomalously small value, $\hbar\omega_N/k_BT_c = 10^{-12}$ (0.04 Hz), yielding good agreement with the experimental data, as shown in Appendix C.2. However, such an artificial enhancement is not physically credible, since additional sources of damping are expected to suppress rather than enhance the coherence peak.

The singlet model was also fitted to the data as shown in Fig. 7.2, assuming $\hbar\omega_N/k_BT_c = 10^{-4}$ and 10^{-2}. Quasiparticle scattering must conserve energy, including the Zeeman and/or quadrupolar energy associated with the nuclear spin flip. In the absence of impurity broadening, the coherence peak diverges when this energy is neglected, but is progressively suppressed as the energy difference between the initial and final quasiparticle states increases. A clear coherence peak is observed below T_c; however, for $\hbar\omega_N/k_BT_c = 10^{-4}$ (dashed cyan line in Fig. 7.2), the calculated peak is significantly larger than the experimental data. The coherence peak is commonly modeled by introducing a broadening term that suppresses the divergence [41]. A similar suppression can be obtained by assuming a larger nuclear resonance frequency. The solid blue line in Fig. 7.3 corresponds to $\hbar\omega_N/k_BT_c = 10^{-2}$, two orders of magnitude larger than the lower-frequency case. This larger nuclear frequency substantially suppresses the coherence peak, and the resulting BCS calculation provides good agreement with the experimental data.

The fitted gap values at $T = 0$, listed in Table 7.1, are comparable to those obtained from previous heat-capacity [80] and magnetic-susceptibility measurements [20], although they are somewhat closer to one another than the gap values reported by recent μSR measurements [72]. As shown in Fig. 7.3, these gap values reproduce the slope of the T_1^{-1} versus $1/T$ data reasonably well, except at the lowest temperatures. The saturation of T_1^{-1} at the lowest temperatures suggests the presence of weak residual impurity scattering. The fitted value of $\phi = 0.157$ indicates that the nuclear spins couple to both bands, with one band having a stronger coupling than the other, as discussed in Appendix C.

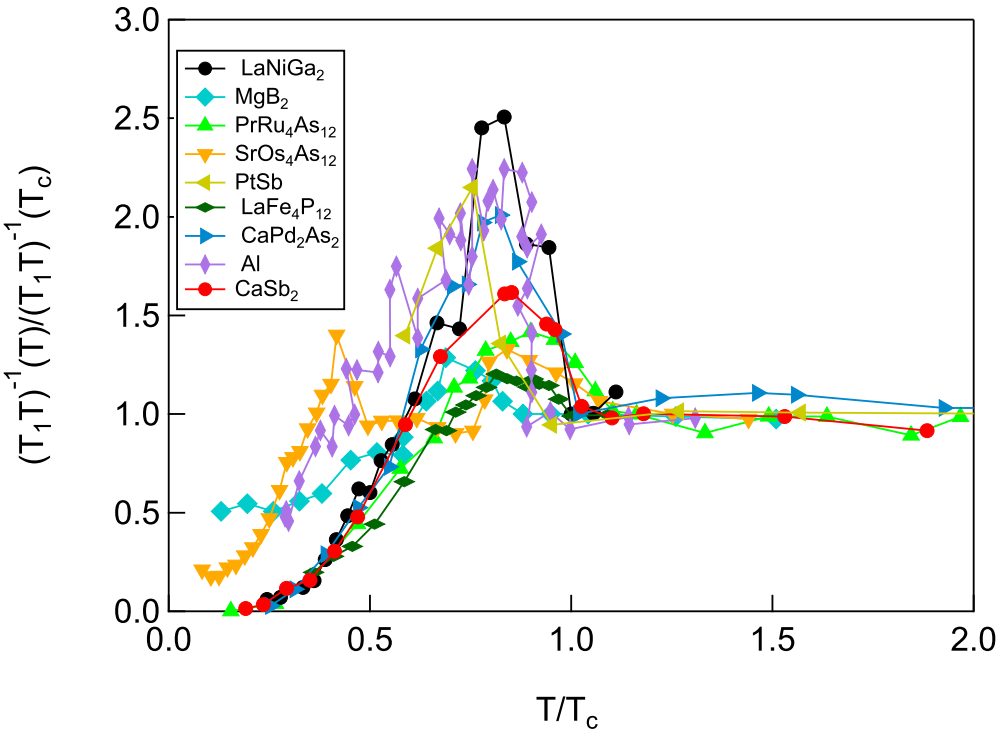


Figure 7.4: Normalized $(T_1T)^{-1}$ versus reduced temperature for several different BCS superconductors, including $LaNiGa_2$ [64], $PrRu_4As_{12}$ [66], $CaPd_2As_2$ [17], $SrOs_4As_{12}$ [16], PtSb [81], $LaFe_4P_{12}$ [46], MgB_2 [35], $CaSb_2$ [74], and Al [42].

Table 7.1: Properties of selected BCS superconductors. Note that measurements in $LaFe_4P_{12}$ and MgB_2 were carried out in an applied field (NMR), and the Al measurements were carried out in zero field via an unusual field-cycling procedure. All others were carried out in zero field (NQR).

Compound	T_c (K)	Δ/k_BT_c	$\hbar\omega_N/k_BT_c$ ($\times10^{-3}$)	Ref.
$PrRu_4As_{12}$	2.3	1.6	1.18	[66]
$LaRu_4As_{12}$	10.3	1.85	2.64	[66]
$CaPd_2As_2$	1.27	1.58	1.57	[17]
$SrOs_4As_{12}$	4.8	1.25	0.62	[16]
PtSb	2.1	1.76	5.83	[81]
$LaFe_4P_{12}$	4.1	1.9	0.13	[46]
MgB_2	39.2	2.5	0.02	[35]
Al	1.178	1.6	–	[42]
$CaSb_2$	1.7	1.52	2.1	[74]
$LaNiGa_2$	1.83	1.41, 1.95	0.11	[64]

The maximum of the Hebel-Slichter peak observed in $LaNiGa_2$ is about 2.5 times the normal

state value, making it large relative to other BCS superconductors as shown in Fig. 7.4. The T_c of the powdered sample was reduced from the single crystal value, likely due to the strain introduced during grinding and possibly some non-magnetic disorder. Normally, the strain and disorder should also result in the suppression of the HS peak making the large size of the peak relative to other materials even more notable. One contribution could be the low frequency at which the measurements were carried out relative to the other superconductors shown in Table 7.1. Regardless, it is clear that there is a robust HS peak in $LaNiGa_2$ relative to the other materials which further supports the conventional pairing.

7.3 Summary

In summary, the zero-field NQR T_1^{-1} data for $LaNiGa_2$ are inconsistent with the INT model unless the two superconducting gaps are identical. In this limiting case, the superconducting state is unitary and therefore does not exhibit time-reversal symmetry breaking (TRSB). In contrast, a two-band BCS model with singlet pairing provides a good description of the data. These results therefore call into question the previously proposed identification of triplet pairing and TRSB in $LaNiGa_2$.

Neither of these scenarios is consistent with the μSR measurements that report TRSB [25]. However, the observed μSR signal is close to the lower limit of experimental sensitivity, and the measurements were performed only on polycrystalline samples. Further μSR measurements on single crystals would therefore be valuable for establishing the intrinsic nature of the observed signal. Independent probes of TRSB, such as optical Kerr rotation measurements [60], would provide an additional test of the proposed TRSB state.

Measurements of the ultrasonic attenuation rate could provide further constraints on the pairing symmetry in $LaNiGa_2$. Ultrasonic attenuation probes a spin-independent relaxation channel and is therefore complementary to NQR measurements. The ultrasonic attenuation

rate, R, arises from the scattering of lattice vibrations by Bogoliubov quasiparticles, providing a relaxation mechanism analogous to that probed by NMR. However, unlike NMR relaxation, which is governed by the spin-dependent interaction, the ultrasonic attenuation rate is governed by the C_- coherence factor in Eq. 5.11, which is even under time reversal. Consequently, the temperature dependence of R in the superconducting state may provide additional information about the superconducting gap structure and pairing symmetry.

Finally, measurements of the NQR relaxation rate at the Ga(2) site could provide further insight into possible asymmetries in the spin fluctuations between different sites in the superconducting state.

Chapter 8

Conclusions

NMR and NQR measurements of $LaNiGa_2$ in the normal state provide no evidence for strong magnetic fluctuations or significant electronic correlations. In particular, the Korringa ratio is close to unity and remains nearly temperature independent at both the ^{139}La and ^{69}Ga sites. Although the Korringa relation is derived under the assumption of a simple, isotropic Fermi surface, the close agreement between the measured Korringa ratios and the uncorrelated value of unity suggests that the magnetic fluctuations in $LaNiGa_2$ are weak. This behavior is consistent with a weakly correlated metallic state in which the electronic contribution to the spin susceptibility is dominated by conventional Pauli paramagnetism. Further evidence for weak electronic correlations is provided by the electric field gradient (EFG). The experimentally determined EFG is in close agreement with DFT calculations performed without explicitly including Coulomb interactions. Since the EFG is sensitive to the local electronic charge distribution, this agreement suggests that the electronic structure of $LaNiGa_2$ can be adequately described without invoking strong electron–electron interactions. Taken together with the nearly temperature-independent magnetic susceptibility and Korringa ratios close to unity, these results provide no evidence for a significant Stoner enhancement of the spin susceptibility or for strong low-energy spin fluctuations.

These observations have important implications for the nature of superconductivity in $LaNiGa_2$. In many unconventional superconductors, strong electronic correlations and associated spin fluctuations are believed to play an important role in mediating or stabilizing unconventional pairing. The absence of significant magnetic fluctuations or other signatures of strong electronic correlations in $LaNiGa_2$ therefore suggests that its superconducting state is unlikely to arise from the same correlation-driven mechanisms commonly attributed to strongly correlated superconductors.

The zero-field NQR T_1^{-1} data for $LaNiGa_2$ provide important constraints on the superconducting pairing state. Within the INT model, the superconducting state is described by two distinct gaps associated with the two components of the triplet order parameter. Our analysis shows that the INT model cannot reproduce the observed temperature dependence of T_1^{-1} when the two gaps have different magnitudes. The model can describe the data only in the limiting case where the two gaps become equal. However, when the two gaps are identical, the resulting superconducting state is unitary and does not exhibit time-reversal symmetry breaking (TRSB). Thus, although the INT model can reproduce the NQR relaxation data under this restrictive condition, it does not simultaneously account for the proposed non-unitary, TRSB triplet state.

In contrast, the zero-field NQR T_1^{-1} data are well described by a two-band BCS model with singlet pairing. In this model, the temperature dependence of the relaxation rate can be understood in terms of quasiparticle excitations from two superconducting bands with different gap magnitudes. The ability of this model to reproduce the experimental data without requiring a triplet order parameter suggests that the NQR relaxation measurements do not support triplet pairing in $LaNiGa_2$. Instead, the data are consistent with a conventional spin-singlet pairing state involving multiple superconducting gaps.

These results therefore call into question the previously proposed interpretation of $LaNiGa_2$ as a triplet superconductor with broken time-reversal symmetry. In particular, the INT

model cannot simultaneously reproduce the observed temperature dependence of T_1^{-1} and retain a non-unitary TRSB state without introducing additional unrealistic assumptions (see Appendix C.2). Although the NQR measurements do not exclude a more complicated unconventional pairing state, they demonstrate that the observed relaxation behavior can be described more naturally by a two-band singlet state without invoking triplet pairing or TRSB. Additional experimental probes that are sensitive to the spin structure and phase of the superconducting order parameter are therefore needed to distinguish between the possible pairing states.

In particular, optical Kerr rotation measurements [60] would provide a direct and independent test for TRSB. A non-zero Kerr signal below T_c would provide evidence for a superconducting state that breaks time-reversal symmetry. Ultrasonic attenuation measurements would provide a complementary probe of the superconducting gap structure and pairing symmetry. Because ultrasonic attenuation involves the scattering of lattice vibrations by Bogoliubov quasiparticles and is governed by a different coherence factor than the NQR relaxation rate, its temperature dependence can provide information that is complementary to that obtained from NQR. In particular, comparing the behavior of the ultrasonic attenuation rate with the NQR T_1^{-1} data could help distinguish between singlet and triplet pairing and place additional constraints on the relative magnitudes and structure of the superconducting gaps. Together, these measurements would provide independent tests of both the proposed TRSB state and the pairing symmetry in $LaNiGa_2$.

Appendix A

^{69}Ga NQR spectrum

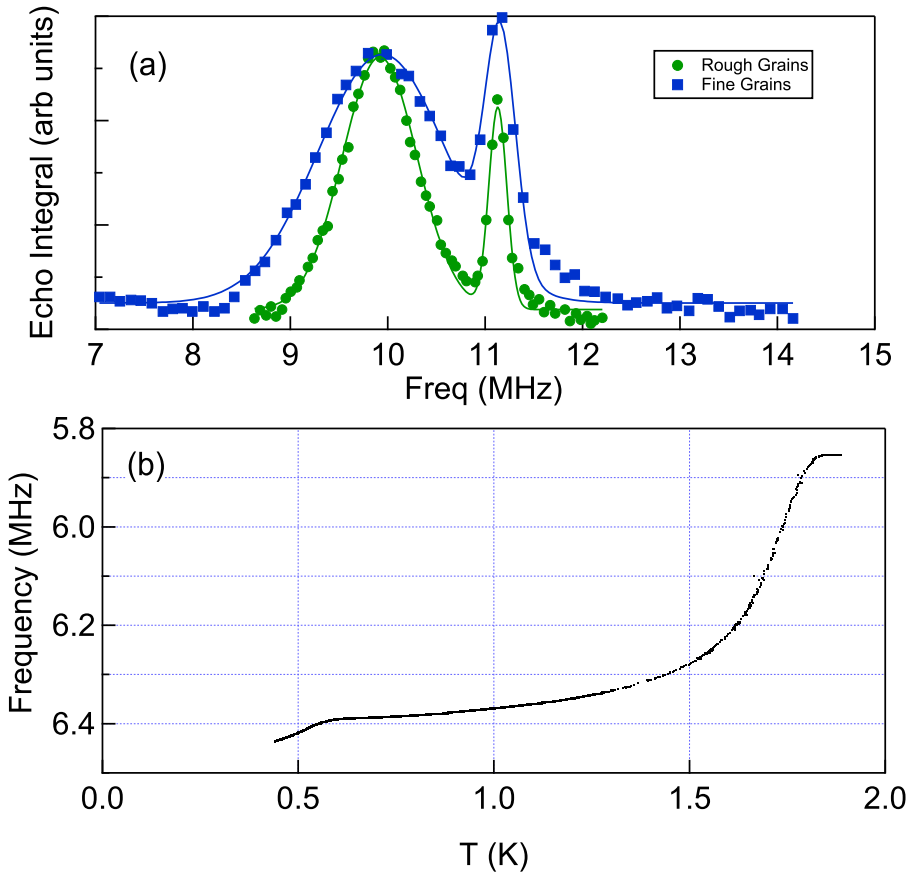


Figure A.1: (a) NQR spectrum of ^{69}Ga(2) before and after grinding the powder to a grain size of 10μm. Solid lines are fits. (b) AC susceptibility of $LaNiGa_2$ as a function of temperature, measured by the resonance frequency of a tuned circuit (note the axis direction is reversed).

Appendix B

XPS

Fig. B.1 displays a series of Ga $2p_{3/2}$ core level spectra under different conditions with different degrees of surface versus bulk sensitivity. The spectra were then fit with a Shirley background [67] and two Voigt line shapes, each corresponding to surface and bulk species. The binding energies across data sets (air-exposed vs freshly cleaved vs Ag source) were kept consistent. The binding energies were calibrated to a reference gold $4f$ spectrum. The Lorentzian and Gaussian widths of the gold reference were found to be 0.385 eV and 0.339 eV, respectively.

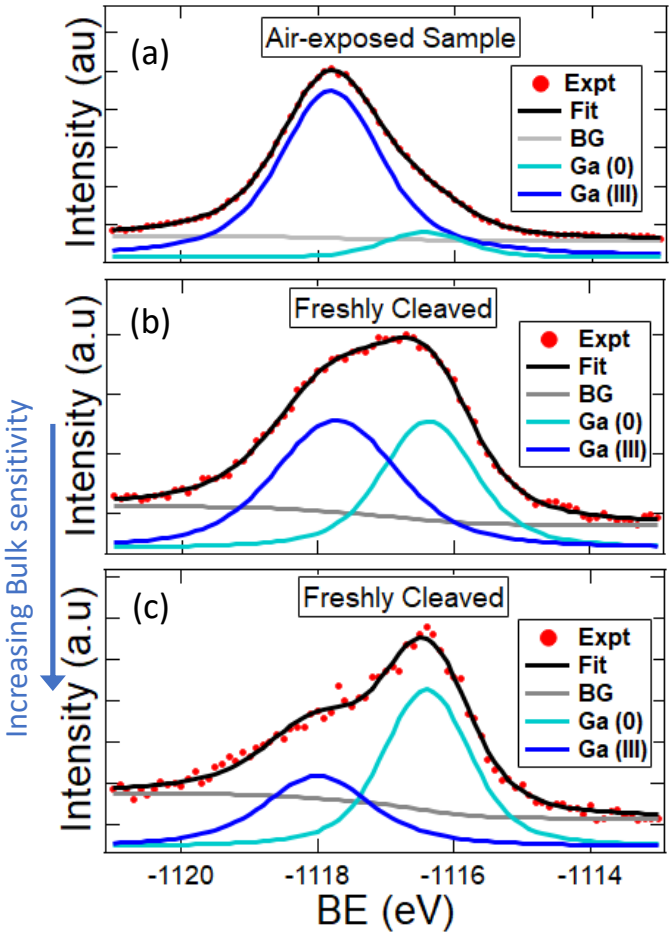


Figure B.1: X-ray Photoemission Spectroscopy of Ga-$2p_{3/2}$ in $LaNiGa_2$. (a) Air-exposed spectrum; (b) Spectrum of the same sample cleaved ex-situ before measurement; and (c) Spectrum of the sample as in (b) but with Ag L-α source.

Appendix C

Computation and fitting of spin-lattice relaxation rate

The computations in Appendix C were performed by Dr. Rahul Hingorani.

C.1 Coherence Factors

We begin by introducing the BdG Hamiltonian governing the electrons in terms of their free Dirac-type dispersion as well as the pairing potential. This acts on an 8-dimensional space that we can think of as the tensor product of three spin-$\frac{1}{2}$ Hilbert spaces corresponding to particle/hole, spin up/down, and band A/B with associated Pauli matrices λ_i, σ_i, and τ_i

respectively. Using this construction, we have

$$H_{BdG} = \sum_{\mathbf{k}} \Psi_{\mathbf{k}}^{\dagger} H(\mathbf{k}) \Psi_{\mathbf{k}}, \tag{C.1}$$

$$H(\mathbf{k}) = \begin{bmatrix} h_0(\mathbf{k}) & \hat{\Delta} \\ \hat{\Delta}^{\dagger} & -h_0(\mathbf{k}) \end{bmatrix},$$

$$h_0(\mathbf{k}) = \mathbb{1}_2 \otimes \left(w_{\mathbf{k}} \cdot \mathbf{k} \mathbb{1}_2 + \gamma_{\mathbf{k}} \cdot \mathbf{k} \tau_x \right),$$

$$\Delta = (\mathbf{d} \cdot \sigma) i\sigma_y \otimes i\tau_y,$$

$$\Psi_k = \left(a_{\mathbf{k}\uparrow}, b_{\mathbf{k}\uparrow}, a_{\mathbf{k}\downarrow}, b_{\mathbf{k}\downarrow}, a^{\dagger}_{-\mathbf{k}\uparrow}, b^{\dagger}_{-\mathbf{k}\uparrow}, a^{\dagger}_{-\mathbf{k}\downarrow}, b^{\dagger}_{-\mathbf{k}\downarrow} \right).$$

Here we use parameters $w_{\mathbf{k}}$ and $\gamma_{\mathbf{k}}$ introduced in [53]. Note, as mentioned in the main text, that dependence on $\mathbf{k}$ will be solely on its component perpendicular to the Fermi surface, so for brevity we suppress the vectorial notation and refer to the perpendicular component by k. The vector $\mathbf{d} = \Delta \boldsymbol{\eta}$, where Δ is a scalar and $\boldsymbol{\eta}$ a unit vector, describes the mechanism through which electrons pair up by spin. We use the basis of electron creation and annihilation operators with momentum and spin labels associated with the A and B bands respectively. At this stage, we elect to consider vectors $\mathbf{d}$ that lie either in the $x-y$ plane or the $y-z$ plane in $\mathbb{C}^3$; i.e. $\mathbf{d} = (d_{x,r} + id_{x,i}, d_{y,r} + id_{y,i}, 0)$ or $\mathbf{d} = (0, d_{y,r} + id_{y,i}, d_{z,r} + id_{z,i})$. The r and i indices denote real and imaginary parts. With this choice, H_{BdG} can be diagonal in the spin (σ) subspace with respect to either the σ_z or the σ_x eigenbasis. Additionally, note that with this choice, the pairing potential $\hat{\Delta}$ can be written as $(\Delta_r(\sigma) - i\Delta_i(\sigma)) \otimes \tau_y$, where:

$$\hat{\Delta}_r(\sigma) = c_j d_{j,i} \sigma_p - d_{y,r} \mathbb{1}_2; \ \hat{\Delta}_i(\sigma) = c_j d_{j,r} \sigma_p + d_{y,i} \mathbb{1}_2, \tag{C.2}$$

and $j = x$ or z with $c_j = \begin{cases} 1 & \text{if } j = x,\ p = z \\ -1 & \text{if } j = z,\ p = x \end{cases}$. Evidently, this pairing potential is diagonal. From here, we work in the $\lambda \otimes \tau$ subspace, which gives us an effective 4×4 model. We replace the operators $\Delta_r(\sigma)$ and $\Delta_i(\sigma)$ with their eigenvalues which we shall denote by $\delta_{jr,\pm} = \pm c_j d_{j,i} - d_{y,r}$ and $\delta_{ji,\pm} = \pm c_j d_{j,r} + d_{y,i}$, leading to:

$$H_{\text{eff}}(k) = w_k k \lambda \otimes \mathbb{1}_2 + \gamma_k k \lambda_z \otimes \tau_x + \delta_{jr,\pm} \lambda_x \otimes \tau_y + \delta_{ji,\pm} \lambda_y \otimes \tau_y. \tag{C.3}$$

Here, one can check that $\lambda_z \otimes \tau_x$ commutes with $H_{\text{eff}}(k)$, so we now change basis from the standard basis to one consisting of eigenvectors of $\lambda_z \otimes \tau_x$, which are of the form $\frac{1}{\sqrt{2}} \begin{pmatrix} 1 \\ 0 \end{pmatrix} \otimes \begin{pmatrix} 1 \\ \pm 1 \end{pmatrix}$ and $\frac{1}{\sqrt{2}} \begin{pmatrix} 0 \\ 1 \end{pmatrix} \otimes \begin{pmatrix} 1 \\ \pm 1 \end{pmatrix}$. In changing basis, we obtain the following Hamiltonian, which we shall denote by $\tilde{H}(k)$, where the Pauli matrices also carry a tilde to emphasize the basis change.

$$\tilde{H}(k) = -\gamma_k k \tilde{\lambda}_z \otimes \mathbb{1}_2 + w_k k \mathbb{1}_2 \otimes \tilde{\tau}_z + \tilde{\lambda}_z \otimes (\delta_{jr,\pm} \tilde{\tau}_y - \delta_{ji,\pm} \tilde{\tau}_x) \tag{C.4}$$

$$= \mp \gamma_k k \mathbb{1}_2 + w_k k \tilde{\tau}_z \pm \delta_{jr,\pm} \tilde{\tau}_y \mp \delta_{ji,\pm} \tilde{\tau}_x \tag{C.5}$$

Equation (C.4) reveals that our transformed Hamiltonian is now diagonal in the $\tilde{\lambda}$ subspace, which means that we can reduce to an effective 2×2 model in $\tilde{\tau}$ space. We now rewrite (C.4) in a manner that suggests how to diagonalize the 2×2 system.

$$\tilde{H}(k) \pm \gamma_k k \mathbb{1}_2 = V_\pm \left(\nu_{\pm\pm} \cdot \tilde{\tau} \right) \tag{C.6}$$

In the line above, we introduce the constant $V_\pm = \sqrt{(w_k k)^2 + \Delta^2 (1 \pm |\boldsymbol{\omega}|)}$. The $\pm$ here distinguishes between spin up$(+)$ and spin down$(-)$, and $\boldsymbol{\omega} = i \boldsymbol{\eta} \times \boldsymbol{\eta}^*$. This precise dependence

of $\Delta^2(1 \pm |\boldsymbol{\omega}|)$ can be obtained by explicitly calculating the normalization factor $V_\pm$ from equation (C.6). The unit vector $\nu_{\pm\pm}$ takes the form $\nu_{\pm\pm} = \frac{1}{V_\pm}(\mp\delta_{ji,\pm}, \pm\delta_{jr,\pm}, w_k k)$. We now define spherical coordinates $\theta_\pm = \arccos\left(\frac{w_k k}{V_\pm}\right)$ and $\varphi_{\pm\pm} = \mathrm{sgn}(\pm\delta_{jr,\pm}) \arccos\left(\frac{\mp\delta_{ji,\pm}}{\Delta}\right)$. In terms of these angular parameters, the eigenvectors of (8) with energies $E_{\mp\pm\pm}(k) = \mp\gamma_k k \pm V_\pm$ are as written below.

$$|t_{\pm\pm-}\rangle = \begin{pmatrix} -e^{-i\varphi_{\pm\pm}} \sin\left(\frac{\theta_\pm}{2}\right) \\ \cos\left(\frac{\theta_\pm}{2}\right) \end{pmatrix} \tag{C.7}$$

$$|t_{\pm\pm+}\rangle = \begin{pmatrix} \cos\left(\frac{\theta_\pm}{2}\right) \\ e^{i\varphi_{\pm\pm}} \sin\left(\frac{\theta_\pm}{2}\right) \end{pmatrix}. \tag{C.8}$$

To generate the eigenvectors of the initial 8×8 model, we first let $|+\rangle = \begin{pmatrix} 1 \\ 0 \end{pmatrix}$ and $|-\rangle = \begin{pmatrix} 0 \\ 1 \end{pmatrix}$, and the color will denote these as eigenvectors of the $\tilde{\lambda}$ subspace (black) or the σ subspace (cyan).

$$|T_{\pm\pm\pm}\rangle_j = |\pm\rangle \otimes |\pm\rangle_j \otimes |t_{\pm\pm\pm}\rangle \tag{C.9}$$

We use the notation here that the subscript j denotes $|\pm\rangle_j$ to be the eigenvectors of σ_j with $j = x$ or z. We will now use these eigenvectors $|T_{\pm\pm\pm}\rangle_j$ to express the Bogoliubov quasiparticle creation and annihilation operators in terms of a and b electron creation and annihilation operators, and we will drop the j subscript for brevity of notation. Letting $u_{k\pm} = -e^{-i\varphi_{+\pm}} \sin\left(\frac{\theta_\pm}{2}\right)$ and $v_{k\pm} = \cos\left(\frac{\theta_\pm}{2}\right)$ be the so-called coherence factors (note the switched convention compared to standard BCS Theory), we are able to derive the following

expressions:

$$\alpha_{\mathbf{k}\pm} = v_{\mathbf{k}\pm}(a_{\mathbf{k}\pm} - b_{\mathbf{k}\pm}) - u^*_{\mathbf{k}\pm}(a^\dagger_{-\mathbf{k}\pm} + b^\dagger_{-\mathbf{k}\pm}) \tag{C.10}$$

$$\beta^\dagger_{-\mathbf{k}\pm} = u_{\mathbf{k}\pm}(a_{\mathbf{k}\pm} - b\mathbf{k}\pm) + v_{\mathbf{k}\pm}(a^\dagger_{-\mathbf{k}\pm} + b^\dagger_{-\mathbf{k}\pm}) \tag{C.11}$$

One can check that these operators satisfy the fermionic anticommutation relations. Note that the general form of these quasiparticle operators is close to the standard BCS form, barring the presence of two bands A and B. However, the basis change we implemented causes a and b electrons to mix, a consequence of the $\gamma_k k$ term in the Hamiltonian. The electron operators may now be expressed in terms of the Bogoliubov operators:

$$a_{\mathbf{k}\pm} = u^*_{\mathbf{k}\pm}\beta^\dagger_{-\mathbf{k}\pm} + v_{\mathbf{k}\pm}\alpha_{\mathbf{k}\pm} - u^*_{-\mathbf{k}\pm}\alpha^\dagger_{-\mathbf{k}\pm} + v_{-\mathbf{k}\pm}\beta_{\mathbf{k}\pm} \tag{C.12}$$

$$b_{\mathbf{k}\pm} = -u^*_{-\mathbf{k}\pm}\alpha^\dagger_{-\mathbf{k}\pm} + v_{-\mathbf{k}\pm}\beta_{\mathbf{k}\pm} - u^*_{\mathbf{k}\pm}\beta^\dagger_{-\mathbf{k}\pm} - v_{\mathbf{k}\pm}\alpha_{\mathbf{k}\pm} \tag{C.13}$$

With these operator expressions, we now move on to computing the nuclear relaxation rate, T_1^{-1}, with reference to the S^+ term of the Hyperfine Hamiltonian. In this calculation, the nuclear wavefunction is approximated as constant, so calculating T_1^{-1} effectively involves using Fermi's Golden Rule to calculate scattering amplitudes associated with electron states. Towards this end, we introduce the operator,

$$S^+_{\mathbf{k},\mathbf{k}'}(\phi) = (\cos(\phi)a^\dagger_{\mathbf{k}\downarrow} + \sin(\phi)b^\dagger_{\mathbf{k}\downarrow})(\cos(\phi)a_{\mathbf{k}'\uparrow} + \sin(\phi)b_{\mathbf{k}'\uparrow}). \tag{C.14}$$

This operator describes electron scattering from momentum **k'** to **k** where spin is flipped, and the parameter ϕ is introduced to allow us to vary the relative weight of a versus b electrons in the scattering process. This angle is given by $\tan\phi = 2A_aA_b/(A_a^2 + A_b^2)$, where $A_{a,b}$ are the hyperfine couplings to the two bands. As mentioned before, we invoke Fermi's

Golden Rule and T_1^{-1} involves calculating $\sum_{i,f} \left|\langle f|S^{+}_{\mathbf{k},\mathbf{k}'}(\phi)|i\rangle\right|^2$, where i and f are the initial and final states of the scattering process which both correspond to states with only one Bogoliubov quasiparticle present. Thus, we sum over initial states featuring an $\alpha_{\mathbf{k}'\pm}$ or a $\beta_{\mathbf{k}'\pm}$ excitation and final states featuring an $\alpha_{\mathbf{k}\pm}$ or a $\beta_{\mathbf{k}\pm}$ excitation. Before proceeding however, we now need to acknowledge the role played by the choice of $j = x$ or z. In the case that $j = z$, we may directly write (C.14) in terms of (S13) and (S14). This lets us calculate the scattering amplitudes directly, and this is presented in the next section. Remark again that we will express the dependence of these expressions on $\mathbf{k}$ as dependence on its component perpendicular to the Fermi surface, denoted as just k.

C.1.1 $j = z$

By direct computation, we express the electron creation and annihilation operators in (C.14), and then read off the scattering amplitudes to obtain,

$$
\begin{aligned}
A_{\alpha\uparrow\to\alpha\downarrow}(k,k') &= v_{k\downarrow}v_{k'\uparrow}\,(1-\sin(2\phi)) \\
A_{\alpha\downarrow\to\alpha\uparrow}(k,k') &= u^{*}_{k\uparrow}u_{k'\downarrow}\,(1+\sin(2\phi)) \\
A_{\beta\uparrow\to\beta\downarrow}(k,k') &= v_{-k\downarrow}v_{-k'\uparrow}\,(1+\sin(2\phi)) \\
A_{\beta\downarrow\to\beta\uparrow}(k,k') &= u^{*}_{-k\uparrow}u_{-k'\downarrow}\,(1-\sin(2\phi)) \\
A_{\alpha\uparrow\to\beta\downarrow}(k,k') &= v_{-k\downarrow}v_{k'\uparrow}\cos(2\phi) \\
A_{\alpha\downarrow\to\beta\uparrow}(k,k') &= u^{*}_{-k\uparrow}u_{k'\downarrow}\cos(2\phi) \\
A_{\beta\uparrow\to\alpha\downarrow}(k,k') &= v_{k\downarrow}v_{-k'\uparrow}\cos(2\phi) \\
A_{\beta\downarrow\to\alpha\uparrow}(k,k') &= u^{*}_{k\uparrow}u_{-k'\downarrow}\cos(2\phi)
\end{aligned}
\tag{C.15}
$$

The next section outlines the differences imposed by the condition $j = x$.

C.1.2 $j = x$

The reason that the calculation of these scattering elements becomes trickier now is that they involve transitions from up spin to down spin particles while our Bogoliubov quasiparticles are labeled by S_x eigenvalues. We make use of the relation:

$$c_{k,\uparrow} = \frac{1}{\sqrt{2}}\left(c_{k,+} + c_{k,-}\right) \tag{C.16}$$

$$c_{k,\downarrow} = \frac{1}{\sqrt{2}}\left(c_{k,+} - c_{k,-}\right), \tag{C.17}$$

where the c_k operator here can be either a_k or b_k. With this transformation, we can write $S^+_{k,k'}(\phi)$, but first note the forms of the operators $S^-_{k,k'}$ and $S^z_{k,k'}$:

$$\begin{aligned} S^-_{k,k'}(\phi) &= (\cos(\phi)a^\dagger_{k\uparrow} + \sin(\phi)b^\dagger_{k\uparrow})(\cos(\phi)a_{k'\downarrow} + \sin(\phi)b_{k'\downarrow}), \\ S^z_{k,k'}(\phi) &= \frac{1}{2}\sum_s s(\cos(\phi)a^\dagger_{ks} + \sin(\phi)b^\dagger_{ks})(\cos(\phi)a_{k's} + \sin(\phi)b_{k's}), \end{aligned} \tag{C.18}$$

where $s = \pm 1$ denotes up/down spin. In this case where our natural spin basis is that of σ_x, we can express $S^+_{k,k'}(\phi)$ in the following way.

$$\begin{aligned} S^{+,\uparrow\backslash\downarrow}_{k,k'}(\phi) &= S^{z,\pm}_{k,k'}(\phi) + \frac{1}{2}\left(S^{-,\pm}_{k,k'}(\phi) - S^{+,\pm}_{k,k'}(\phi)\right) \\ &= S^{z,\pm}_{k,k'}(\phi) - iS^{y,\pm}_{k,k'}(\phi) \end{aligned} \tag{C.19}$$

The notation for the S operators in the equation above is as follows. Those operators with $\uparrow \backslash \downarrow$ as a superscript involve spin matrices written in the usual z-basis. Those with $\pm$ in the superscript involve the exact same matrices, elementwise, except the "z-basis" here actually corresponds to the x-basis. Consequently, the scattering amplitudes associated with $S^{+,\uparrow\backslash\downarrow}_{k,k'}(\phi)$ can be calculated by considering scattering between $\alpha_\pm$ particles and $\beta_\pm$ particles. Furthermore, we can use the same scattering amplitudes found in the previous section, except

the $\uparrow\rightarrow\downarrow$ scattering and vice versa will refer to $+\rightarrow-$ scattering and vice versa. With this in mind, we have the following amplitudes that will contribute to our calculation of T_1^{-1}.

$$A_{\alpha\pm\rightarrow\alpha\pm}(k,k') = \frac{1}{2}\left(v_{k\pm}v_{k'\pm}(1-\sin(2\phi)) - u^*_{k\pm}u_{k'\pm}(1+\sin(2\phi))\right) \tag{C.20}$$

$$A_{\beta\pm\rightarrow\beta\pm}(k,k') = \frac{1}{2}\left(v_{-k\pm}v_{-k'\pm}(1+\sin(2\phi)) - u^*_{-k\pm}u_{-k'\pm}(1-\sin(2\phi))\right)$$

$$A_{\alpha\pm\rightarrow\beta\pm}(k,k') = \frac{1}{2}\cos(2\phi)\left(u^*_{-k\pm}u_{k'\pm} - v_{-k\pm}v_{k'\pm}\right)$$

$$A_{\beta\pm\rightarrow\alpha\pm}(k,k') = \frac{1}{2}\cos(2\phi)\left(u^*_{k\pm}u_{-k'\pm} - v_{k\pm}v_{-k'\pm}\right)$$

$$A_{\alpha+\rightarrow\alpha-}(k,k') = \frac{1}{2}\left(u^*_{k-}u_{k'+}(1+\sin(2\phi)) - v_{k-}v_{k'+}(1-\sin(2\phi))\right)$$

$$A_{\alpha-\rightarrow\alpha+}(k,k') = \frac{1}{2}\left(v_{k+}v_{k'-}(1-\sin(2\phi)) - u^*_{k+}u_{k'-}(1+\sin(2\phi))\right)$$

$$A_{\beta+\rightarrow\beta-}(k,k') = \frac{1}{2}\left(u^*_{-k-}u_{-k'+}(1-\sin(2\phi)) - v_{-k-}v_{-k'+}(1+\sin(2\phi))\right)$$

$$A_{\beta-\rightarrow\beta+}(k,k') = \frac{1}{2}\left(v_{-k+}v_{-k'-}(1+\sin(2\phi)) - u^*_{-k+}u_{-k'-}(1-\sin(2\phi))\right)$$

$$A_{\alpha+\rightarrow\beta-}(k,k') = \frac{1}{2}\cos(2\phi)\left(u^*_{-k-}u_{k'+} - v_{-k-}v_{-k'+}\right)$$

$$A_{\alpha-\rightarrow\beta+}(k,k') = \frac{1}{2}\cos(2\phi)\left(v_{-k+}v_{k'-} - u^*_{-k+}u_{k'-}\right)$$

$$A_{\beta+\rightarrow\alpha-}(k,k') = \frac{1}{2}\cos(2\phi)\left(u^*_{k-}u_{-k'+} - v_{k-}v_{-k'+}\right)$$

$$A_{\beta-\rightarrow\alpha+}(k,k') = \frac{1}{2}\cos(2\phi)\left(v_{k+}v_{-k'-} - u^*_{k+}u_{-k'-}\right)$$

These amplitudes can be decomposed into two subsets of scattering processes: those which preserve the x component of spin and those which flip this. The first four equations involve the processes that preserve spin, and these are in fact the same amplitudes that appear in the calculation of ultrasonic attenuation for either orientation of $\mathbf{d}$ that we have considered. The existence of spin-preserving, i.e. gap preserving, scattering is what distinguishes the behavior of quasiparticle scattering when $\mathbf{d}$ has a component along the z-axis.

C.1.3 Relaxation Rate

With these amplitudes in hand, we may now proceed to calculate the nuclear relaxation rate using Fermi's Golden Rule. Following the notes of Arovas and Wu, we sum over **k**, **k'**, and spins $s, s' = \pm 1$ of the following (where s, s' can correspond to either the z or x bases):

$$\sum_{\mathbf{k},\mathbf{k'},s,s'} |A_{\alpha s' \to \alpha s}(\mathbf{k},\mathbf{k'})|^2 f_{\alpha,\mathbf{k},s}(1 - f_{\alpha,\mathbf{k'},s'})\delta(E_{\alpha,\mathbf{k'},s'} - E_{\alpha,\mathbf{k},s} - \hbar\omega) + \tag{C.21}$$

$$|A_{\beta s' \to \beta s}(\mathbf{k},\mathbf{k'})|^2 f_{\beta,\mathbf{k},s}(1 - f_{\beta,\mathbf{k'},s'})\delta(E_{\beta,\mathbf{k'},s'} - E_{\beta,\mathbf{k},s} - \hbar\omega)$$

where $f_{\alpha,\mathbf{k},s}$ and $f_{\beta,\mathbf{k},s}$ denote the Fermi-Dirac functions corresponding to alpha and beta particles respectively with momentum **k** and spin s. This labeling convention is also used to index the energies in the argument of the delta function. Note that the strongest enhancement of the relaxation rate will occur due to processes that do not require quasiparticles to hop across the two gaps, i.e. the spin component is preserved. These are more energetically favorable and are only possible if **d** is perpendicular to the **x** direction (see the first four equations of Eq. C.20). To introduce temperature dependence into the formation of a superconducting gap, we let $\Delta(T) = \Delta_0(T)\sqrt{1 - \left(\frac{\gamma_k}{w_k}\right)^2}\sqrt{1 \pm |\sin\theta_\eta|}$, where $\Delta_0(T)$ has the temperature dependence given by the solution to the self-consistency equation for the singlet BCS Theory gap,

$$\int_0^\infty d\epsilon \left[\frac{\tanh\left(\sqrt{\epsilon^2 + \Delta^2}/2T\right)}{\sqrt{\epsilon^2 + \Delta^2}} - \frac{1}{\sqrt{\epsilon^2 + \Delta(0)^2}}\right], \tag{C.22}$$

where $\Delta(0)$ is the $T = 0$ value of the parameter such that $T_c = 1$. $\Delta_0(T)$ is then obtained by scaling the solution to the equation above such that $\Delta_0(0)$ takes on any given value.

C.2 Variation with nuclear frequency

Figure C.1 shows the calculated T_1^{-1} for several different values of the nuclear resonance frequency within the INT model for $\mathbf{d} \perp \mathbf{x}$. Smaller frequencies enhance the coherence peak, but the experimental measurement frequency is $\omega_N = 10^{-4}$. Note that in the INT model, with two distinct gaps it is still possible to have enhancement of T_1^{-1} below T_c due to scattering processes that preserve the spin component, so reducing the nuclear frequency enables this enhancement to increase to a point where it can fit the experimental data more closely. However, such a fit requires an unphysical nuclear frequency of $\hbar\omega_N/k_BT_c = 10^{-12}$ to achieve good agreement with the data (the experimental value is 10^{-4}). This suggests a very sensitive peak with notable time reversal symmetry breaking, as discussed in the main text.

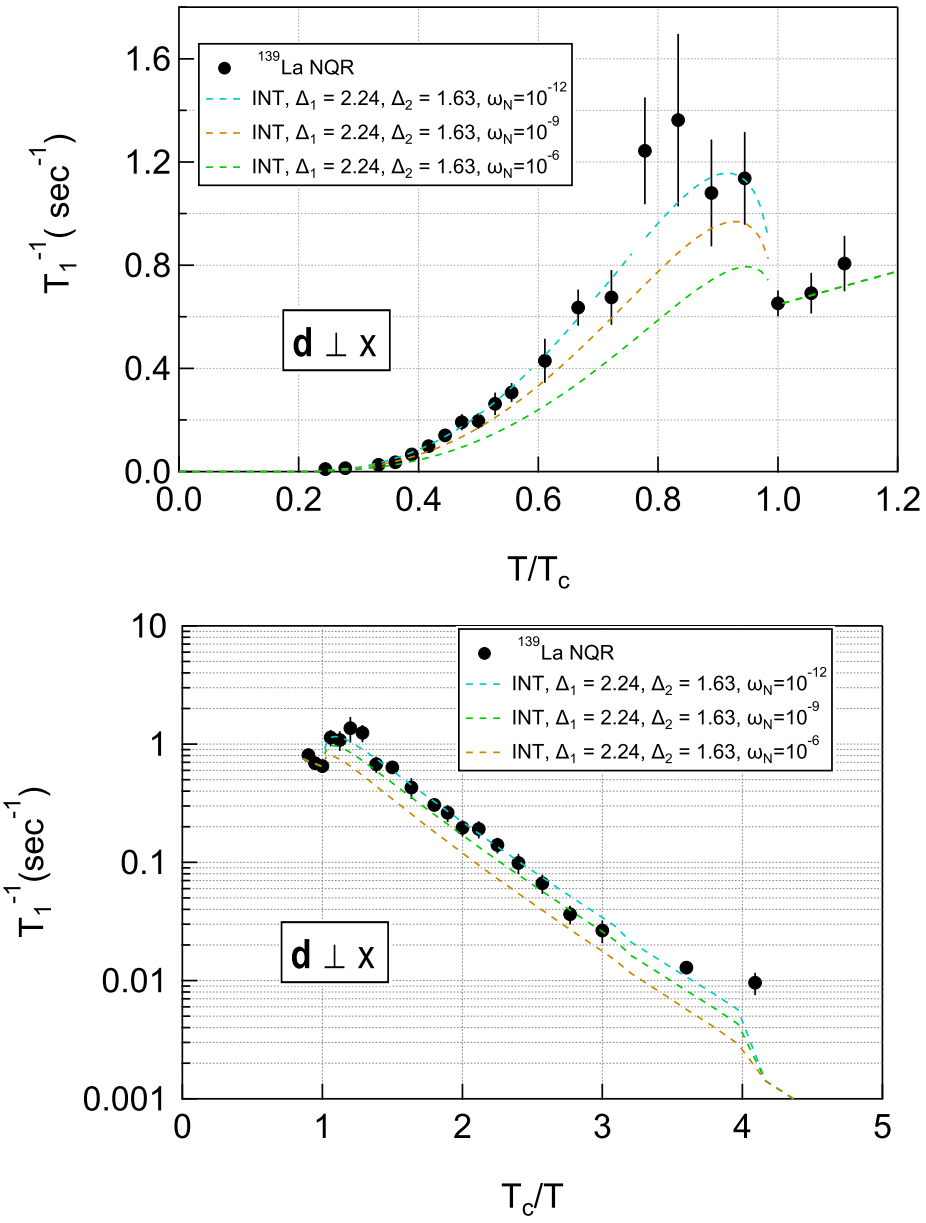


Figure C.1: Calculated T_1^{-1} versus temperature and inverse temperature within the INT model for various values of the measurement frequency, ω_N. The solid points are the experimental measurements.

C.3 d-vector of form $(r, i, 0)$

As described in the main text, one class of pairing vector $\mathbf{d}$ we consider is of the form $\mathbf{d}_r = \frac{\Delta_0}{\sqrt{1+r^2}}(r, i, 0)$. With the parameter ϕ from the scattering operator $S(\phi)$ set to 0.05π and nuclear frequency set to $\omega_N = 10^{-4}$, we find best fit parameters $\Delta_0 = 1.9$, $r = 5 \times 10^{-5}$, indicated by the hexagon in Fig. C.2(a). The fitting was performed by calculating the reduced χ^2, comparing theoretical calculations with experimental data. Note that we restrict the temperature range, in units of T/T_c, to $T > 0.4$ to emphasize the fitting of the peak of $(T_1)^{-1}$. Furthermore, these best fit parameters yield two superconducting gaps of 1.8599 and 1.8601, which are nearly identical. As one deviates from $\Delta_0 = 1.9$, $r = 5 \times 10^{-5}$, the fit quality worsens, and Fig. C.2(b) illustrates examples of this. If one were to consider plots of $(T_1)^{-1}$ generated by parameters outside the blue envelope in the heat map of Fig. C.2(a), the fit to the peak would deteriorate noticeably in comparison to even the curve with $\chi^2 = 2.4$. Importantly, the heat map illustrates that for larger Δ_0, which scales the two gaps of the model, better fits arise from using smaller r, causing the splitting of the two gaps to be reduced. This behavior is also illustrated in Fig. C.3, which reveals a steep minimum in χ^2 when the two gaps are identical. As one decreases Δ_0, increasing r beyond 0 has a smaller effect on the difference in the two gaps, i.e. time reversal symmetry breaking. Thus, the r values that fit the experiment up to $\chi^2 < 4$ get larger as Δ_0 decreases. However, as Δ_0 reaches below 1.7, not only does the fit of the INT model worsen, but the range of "better fitting" r values becomes narrower as well. Ultimately, aside from these details, the range of r studied here induces minimal TRSB, which is the important takeaway from solving the INT model.

Changing the relative sizes of the hyperfine couplings to the two bands, characterized by the parameter ϕ, does not change this conclusion. Figures C.4 and C.5 show heat maps of χ^2 in $r - \phi$ and $\Delta_0 - \phi$ space, respectively. The quality of the fits are not improved by changing

the relative size of these hyperfine couplings.

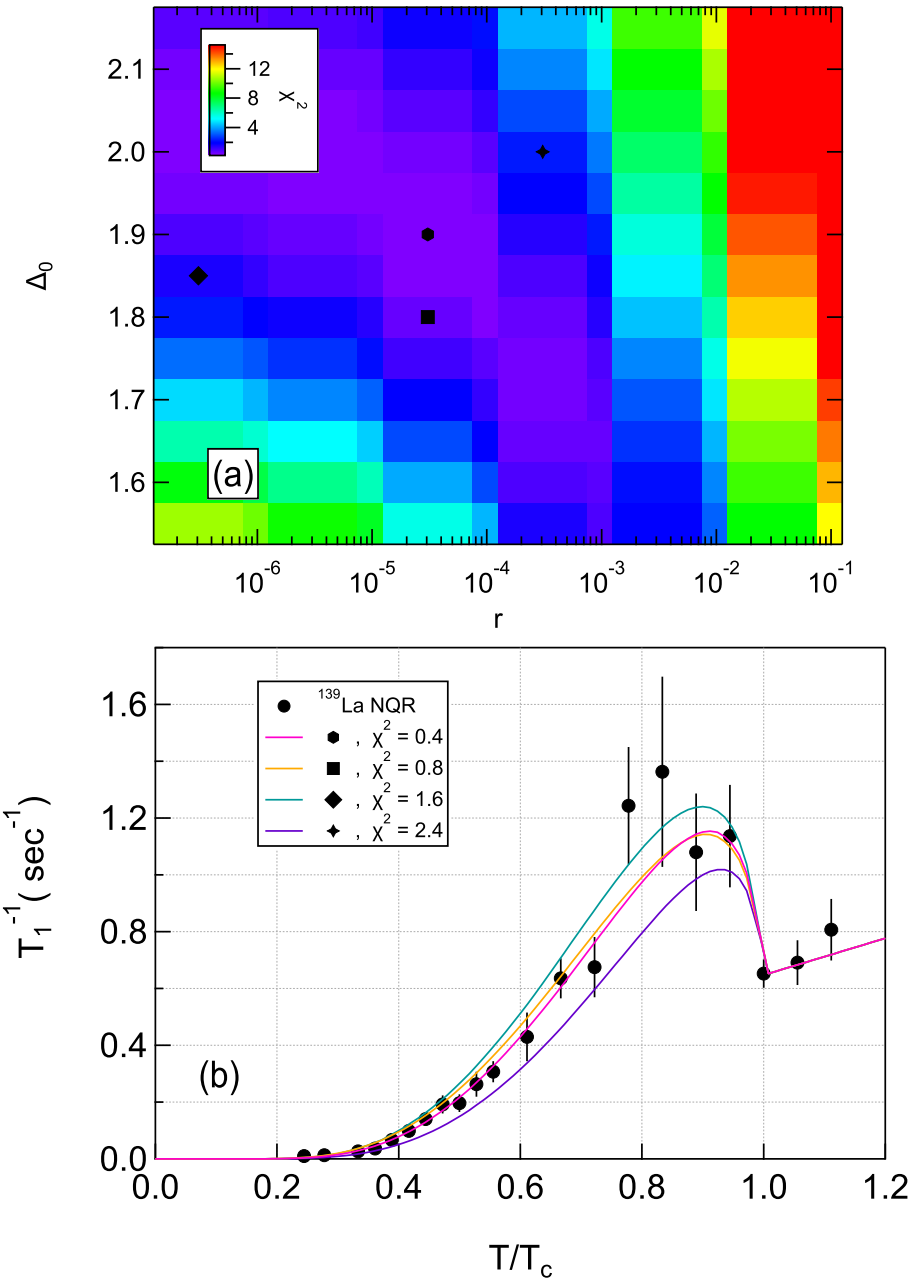


Figure C.2: Panel (a) shows χ^2 as a function of fitting parameters r and Δ_0 as a heat map. The four points correspond to different curves in panel (b). The best fit is given by the solid hexagon (magenta curve).

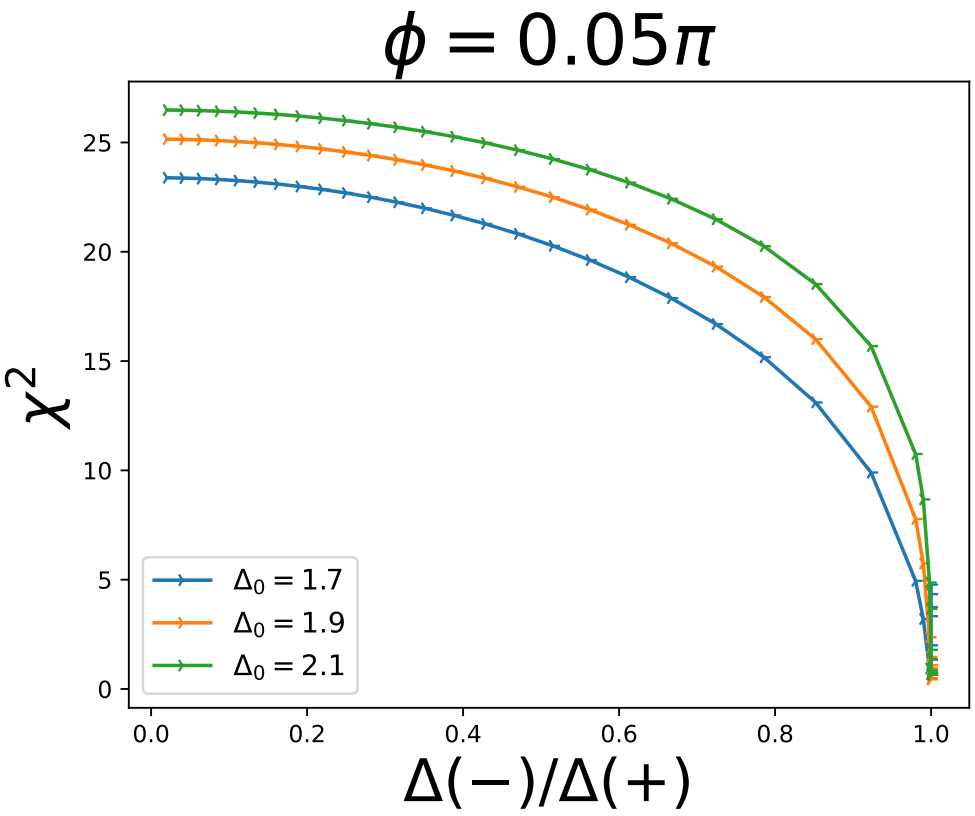


Figure C.3: χ^2 versus the gap ratio Δ_-/Δ_+ (see Eq. (5.22) in main text) for several different values of Δ_0 and fixed parameter ϕ. There is a steep minimum at $\Delta_- = \Delta_+$, reflecting the fact that the coherence factor is quickly suppressed when the gaps are not equal.

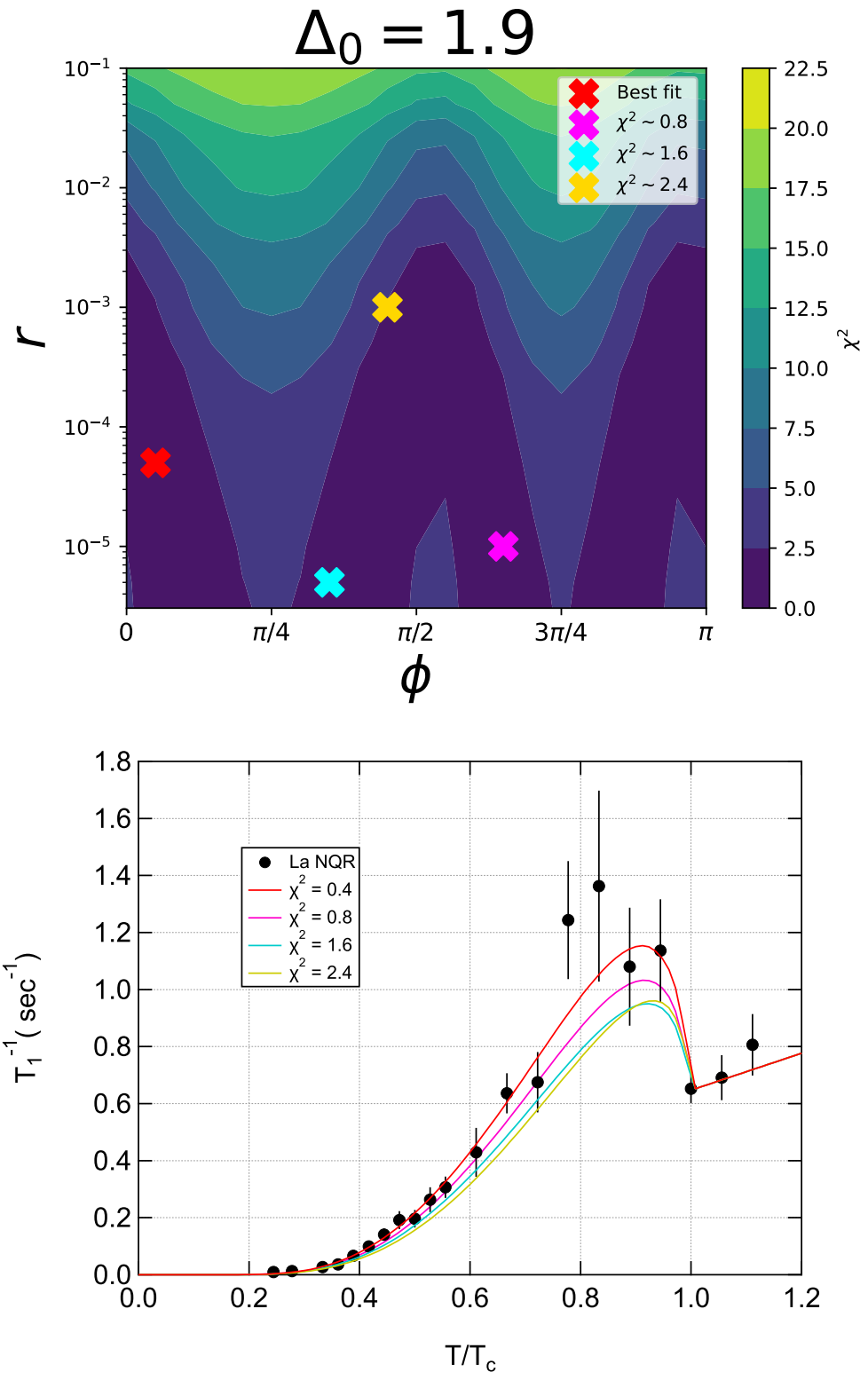


Figure C.4: The upper panel shows χ^2 as a function of fitting parameters r and ϕ as a heat map. The four points correspond to different curves in the lower panel.

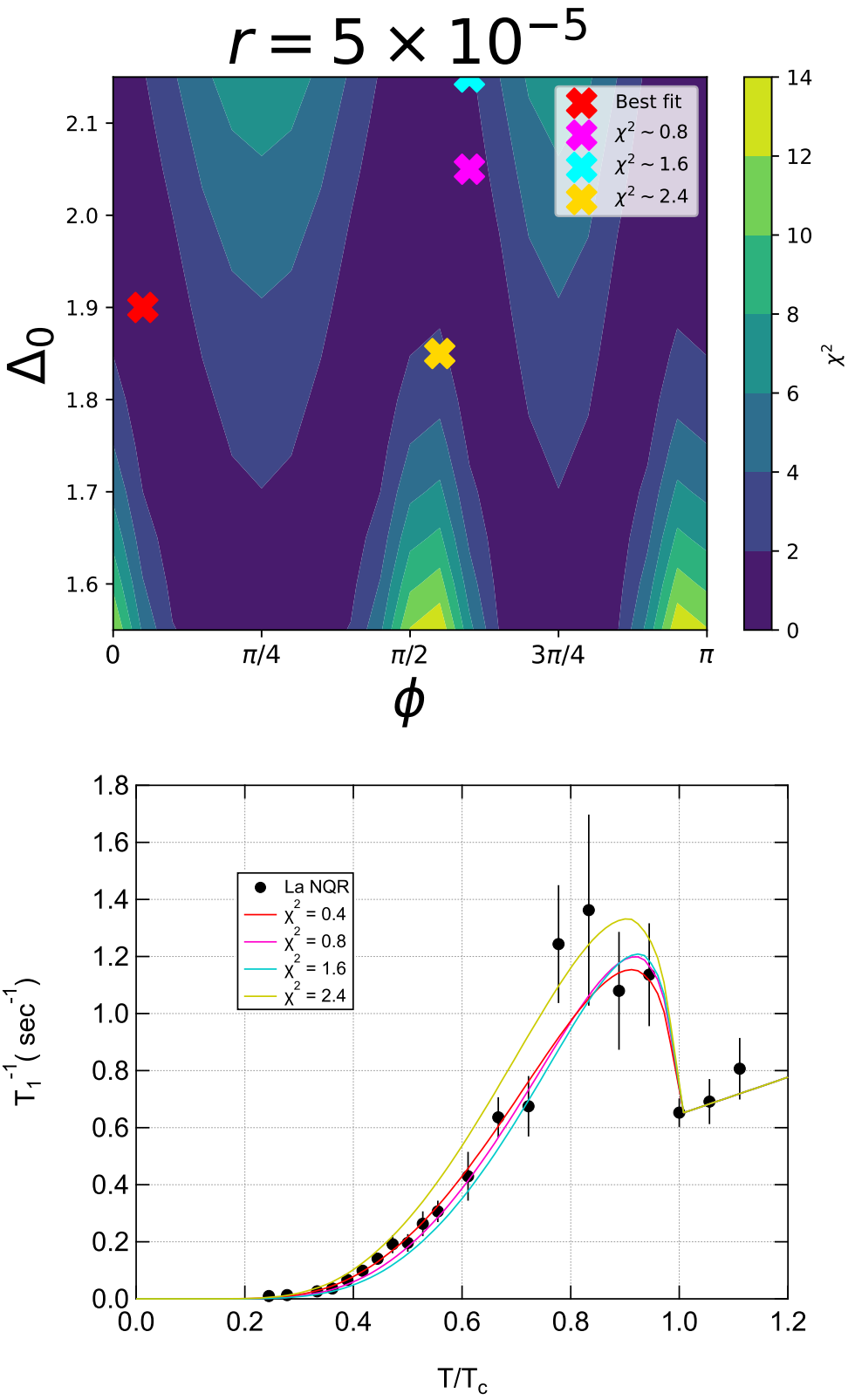


Figure C.5: The upper panel shows χ^2 as a function of fitting parameters Δ_0 and ϕ as a heat map. The four points correspond to different curves in the lower panel.

Bibliography

[1] J. F. Annett, *Symmetry of the order parameter for high-temperature superconductivity*, Advances in Physics, 39 (1990), pp. 83–126.

[2] J. R. Badger, Y. Quan, M. C. Staab, S. Sumita, A. Rossi, K. P. Devlin, K. Neubauer, D. S. Shulman, J. C. Fettinger, P. Klavins, et al., *Dirac lines and loop at the fermi level in the time-reversal symmetry breaking superconductor* $laniga_2$, Communications Physics, 5 (2022).

[3] G. A. Bain and J. F. Berry, *Diamagnetic corrections and pascal's constants*, Journal of Chemical Education, 85 (2008), pp. 532–532.

[4] J. Bardeen, L. N. Cooper, and J. R. Schrieffer, *Theory of superconductivity*, Phys. Rev., 108 (1957), pp. 1175–1204.

[5] S. E. Barrett, D. J. Durand, C. H. Pennington, C. P. Slichter, T. A. Friedmann, J. P. Rice, and D. M. Ginsberg, ^{63}Cu *knight shifts in the superconducting state of* $yba_2cu_3o_{7-\delta}$ *(t_c=90 k)*, Phys. Rev. B, 41 (1990), pp. 6283–6296.

[6] B. Blaisse, A. Cooke, and R. Hull, *On the attainment of low temperatures by pumping liquid helium ii*, Physica, 6 (1939), pp. 231–239.

[7] F. Bloch, *Nuclear induction*, Phys. Rev., 70 (1946), pp. 460–474.

[8] N. Bloembergen, E. M. Purcell, and R. V. Pound, *Relaxation effects in nuclear magnetic resonance absorption*, Phys. Rev., 73 (1948), pp. 679–712.

[9] G. Blumberg, P. Littlewood, A. Gozar, B. S. Dennis, N. Motoyama, H. Eisaki, and S. Uchida, *Sliding density wave in $sr_{14}cu_{24}o_{41}$ ladder compounds*, Science, 297 (2002), pp. 584–587.

[10] N. N. Bogoliubov, *On a new method in the theory of superconductivity*, Il Nuovo Cimento, 7 (1958), pp. 794–805.

[11] R. W. Bounds, E. Pavarini, M. Paolella, E. Young, I. Heinmaa, R. Stern, and M. Carravetta, *Study of* ^{11}B *and* ^{13}C *nmr on doped* $\mathrm{mgb_2}$ *in the normal and in the superconducting state*, Phys. Rev. B, 97 (2018), p. 014509.

[12] J.-P. Brison, *p-wave superconductivity and d-vector representation*, in Magnetism and Accelerator-Based Light Sources, H. Bulou, L. Joly, J.-M. Mariot, and F. Scheurer, eds., Cham, 2021, Springer International Publishing, pp. 165–204.

[13] R. Chandra and V. S. Nanda, *Thermodynamic properties of he3 and he4 solutions. ii. temperatures above the superfluid transition in solution*, The Physics of Fluids, 7 (1964), pp. 15–19.

[14] P. Coleman, *Introduction to Many-Body Physics*, Cambridge University Press, Cambridge, UK, 2015.

[15] J. L. Curro N.J, Sarrao, L. A. Morales, J. D. Thompson, B. L. Scott, G. R. Stewart, F. Wastin, J. M. Rebizant, P. Boulet, E. Colineau, and G. H. Lander, *Unconventional superconductivity in pucoga5*, Nature, 434 (2005), pp. 648–650.

[16] Q.-P. Ding, K. Nishine, Y. Kawamura, J. Hayashi, C. Sekine, and Y. Furukawa, *Suppression of ferromagnetic spin fluctuations in the filled skutterudite superconductor* $\mathrm{sros_4as_{12}}$ *revealed by* ^{75}As *nmr-nqr measurements*, Phys. Rev. B, 100 (2019), p. 054516.

[17] Q.-P. Ding, P. Wiecki, V. K. Anand, N. S. Sangeetha, Y. Lee, D. C. Johnston, and Y. Furukawa, *Volovik effect and fermi-liquid behavior in the s-wave superconductor* $\mathrm{capd_2as_2}$:^{75} As *nmr-nqr measurements*, Phys. Rev. B, 93 (2016), p. 140502(R).

[18] R. D. Evans, *The Atomic Nucleus*, TATA McGraw-Hill, tmh ed., 1980.

[19] M. Frachet, I. Vinograd, R. Zhou, S. Benhabib, S. Wu, H. Mayaffre, S. Krämer, S. K. Ramakrishna, A. P. Reyes, J. Debray, T. Kurosawa, N. Momono, M. Oda, S. Komiya, S. Ono, M. Horio, J. Chang, C. Proust, D. LeBoeuf, and M.-H. Julien, *Hidden magnetism at the pseudogap critical point of a cuprate superconductor*, Nature Physics, 16 (2020), pp. 1064–1068.

[20] S. Ghimire, K. R. Joshi, E. H. Krenkel, M. A. Tanatar, Y. Shi, M. Kończykowski, R. Grasset, V. Taufour, P. P. Orth, M. S. Scheurer, and R. Prozorov, *Electron irradiation reveals robust fully gapped superconductivity in* $\mathrm{laniga_2}$, Phys. Rev. B, 109 (2024), p. 024515.

[21] S. K. Ghosh, G. Csire, P. Whittlesea, J. F. Annett, M. Gradhand, B. Újfalussy, and J. Quintanilla, *Quantitative theory of triplet pairing in the unconventional superconductor* $\mathrm{laniga_2}$, Phys. Rev. B, 101 (2020), p. 100506(R).

[22] H.-J. Grafe, D. Paar, G. Lang, N. J. Curro, G. Behr, J. Werner, J. Hamann-Borrero, C. Hess, N. Leps, R. Klingeler, and B. Büchner, ^{75}As *nmr studies of superconducting* $\mathrm{LaFeAso_{0.9}f_{0.1}}$, Phys. Rev. Lett., 101 (2008), p. 047003.

[23] L. C. Hebel and C. P. Slichter, *Nuclear relaxation in superconducting aluminum*, Phys. Rev., 107 (1957), pp. 901–902.

[24] ——, *Nuclear spin relaxation in normal and superconducting aluminum*, Phys. Rev., 113 (1959), pp. 1504–1519.

[25] A. D. Hillier, J. Quintanilla, B. Mazidian, J. F. Annett, and R. Cywinski, *Nonunitary triplet pairing in the centrosymmetric superconductor $LaNiGa_2$*, Phys. Rev. Lett., 109 (2012), p. 097001.

[26] W. A. Hines and W. D. Knight, *Spin-orbit coupling and nuclear magnetic resonance in superconducting metals*, Phys. Rev. B, 4 (1971), pp. 893–903.

[27] J. Hwang, P. Canepa, and T. Scott, *Pressure dependence of the electric field gradient and knight shift tensors of single crystal gallium*, Journal of Physics and Chemistry of Solids, 38 (1977), pp. 1403–1409.

[28] T. Imai, A. W. Hunt, K. R. Thurber, and F. C. Chou, *^{17}o nmr evidence for orbital dependent ferromagnetic correlations in* $\mathrm{sr_2ruo_4}$, Phys. Rev. Lett., 81 (1998), pp. 3006–3009.

[29] K. Ishida, H. Mukuda, Y. Kitaoka, K. Asayama, Z. Q. Mao, Y. Mori, and Y. Maeno, *Spin-triplet superconductivity in Sr_2RuO_4 identified by ^{17}O knight shift*, Nature, 396 (1998), pp. 658–660.

[30] K. Ishida, H. Mukuda, Y. Kitaoka, Z. Q. Mao, H. Fukazawa, and Y. Maeno, *Ru nmr probe of spin susceptibility in the superconducting state of* $\mathrm{sr_2ruo_4}$, Phys. Rev. B, 63 (2001), p. 060507(R).

[31] K. Ishida, D. Ozaki, T. Kamatsuka, H. Tou, M. Kyogaku, Y. Kitaoka, N. Tateiwa, N. K. Sato, N. Aso, C. Geibel, and F. Steglich, *Spin-triplet*

superconductivity in $\mathrm{uni_2al_3}$ *revealed by the* ^{27}*al knight shift measurement*, Phys. Rev. Lett., 89 (2002), p. 037002.

[32] Y. Iwamoto, Y. Iwasaki, K. Ueda, and T. Kohara, *Microscopic measurements in 139la-nqr of the ternary carbide superconductor lanic2*, Physics Letters A, 250 (1998), pp. 439–442.

[33] S. Jalali Asadabadi, *Electronic structure and electric-field gradient analysis in* $\mathrm{Cein_3}$, Phys. Rev. B, 75 (2007), p. 205130.

[34] P. Jeglič, A. Potočnik, M. Klanjšek, M. Bobnar, M. Jagodič, K. Koch, H. Rosner, S. Margadonna, B. Lv, A. M. Guloy, and D. Arčon, ^{75}*As nuclear magnetic resonance study of antiferromagnetic fluctuations in the normal state of lifeas*, Phys. Rev. B, 81 (2010), p. 140511(R).

[35] M. Karayanni, G. Papavassiliou, M. Pissas, M. Fardis, K. Papagelis, K. Prassides, T. Takenobu, and Y. Iwasa, *11b nmr study of pure and lightly carbon-doped mgb2 superconductors*, Journal of Superconductivity, 18 (2005), p. 521–528.

[36] C. Kittel, *Introduction to Solid State Physics*, John Wiley & Sons, Hoboken, NJ, 8th ed., 2004.

[37] J. Korringa, *Nuclear magnetic relaxation and resonnance line shift in metals*, Physica, 16 (1950), pp. 601–610.

[38] M. Lee, G. F. Moores, Y.-Q. Song, W. P. Halperin, W. W. Kim, and G. R. Stewart, ^{195}Pt *spin dynamics and knight shift in single crystals of* $\mathrm{upt_3}$, Phys. Rev. B, 48 (1993), pp. 7392–7398.

[39] F. London and H. London, *The electromagnetic equations of the supraconductor*, Proceedings of The Royal Society A: Mathematical, Physical and Engineering Sciences, 149 (1935), pp. 71–88.

[40] G. M. Luke, Y. Fudamoto, K. M. Kojima, M. I. Larkin, J. Merrin, B. Nachumi, Y. J. Uemura, Y. Maeno, Z. Q. Mao, Y. Mori, H. Nakamura, and M. Sigrist, *Time-reversal symmetry-breaking superconductivity in sr_2ruo_4*, Nature, 394 (1998), pp. 558–561.

[41] D. E. MacLaughlin, *Magnetic resonance in the superconducting state*, in Solid State Physics, H. Ehrenreich, F. Seitz, and D. Turnbull, eds., vol. 31 of Solid State Physics, Academic Press, 1976, pp. 1–69.

[42] Y. Masuda and A. G. Redfield, *Nuclear spin-lattice relaxation in superconducting aluminum*, Physical Review, 125 (1962), pp. 159–166.

[43] L. B. Mendelsohn, F. Biggs, and J. B. Mann, *Hartree-fock diamagnetic susceptibilities*, Phys. Rev. A, 2 (1970), pp. 1130–1134.

[44] P. Monthoux, D. Pines, and G. G. Lonzarich, *Superconductivity without phonons*, Nature, 450 (2007), pp. 1177–1183.

[45] T. Moriya, *The effect of electron-electron interaction on the nuclear spin relaxation in metals*, Journal of the Physical Society of Japan, 18 (1963), pp. 516–520.

[46] Y. Nakai, K. Ishida, D. Kikuchi, H. Sugawara, and H. Sato, *Evidence for s-wave superconductivity with antiferromagnetic fluctuations in filled skutterudite lafe4p12: 139la and 31p-nmr studies*, Journal of the Physical Society of Japan, 74 (2005), pp. 3370–3374.

[47] A. Narath and H. T. Weaver, *Effects of electron-electron interactions on nuclear spin-lattice relaxation rates and knight shifts in alkali and noble metals*, Phys. Rev., 175 (1968), pp. 373–382.

[48] K. Narita, J. Umeda, and H. Kusumoto, *Nuclear magnetic resonance powder patterns of the second-order nuclear quadrupole interaction in solids with asymmetric field gradient*, The Journal of Chemical Physics, 44 (1966), pp. 2719–2723.

[49] R. J. NOER and W. D. KNIGHT, *Nuclear magnetic resonance and relaxation in superconducting vanadium*, Rev. Mod. Phys., 36 (1964), pp. 177–185.

[50] J. A. Osborn, *Demagnetizing factors of the general ellipsoid*, Phys. Rev., 67 (1945), pp. 351–357.

[51] J. Owen and J. H. M. Thornley, *Covalent bonding and magnetic properties of transition metal ions*, Reports on Progress in Physics, 29 (1966), p. 675.

[52] A. Pustogow, Y. Luo, A. Chronister, Y.-S. Su, D. A. Sokolov, F. Jerzembeck, A. P. Mackenzie, C. W. Hicks, N. Kikugawa, S. Raghu, E. D. Bauer, and S. E. Brown, *Constraints on the superconducting order parameter in sr_2ruo_4 from oxygen-17 nuclear magnetic resonance*, Nature, 574 (2019), pp. 72–75.

[53] Y. Quan, V. Taufour, and W. E. Pickett, *Nonsymmorphic band sticking in a topological superconductor*, Phys. Rev. B, 105 (2022), p. 064517.

[54] A. Ramires, *Nonunitary superconductivity in complex quantum materials*, Journal of Physics: Condensed Matter, 34 (2022), p. 304001.

[55] N. F. Ramsey and E. M. Purcell, *Interactions between nuclear spins in molecules*, Phys. Rev., 85 (1952), pp. 143–144.

[56] S. Ran, C. Eckberg, Q.-P. Ding, Y. Furukawa, T. Metz, S. R. Saha, I.-L. Liu, M. Zic, H. Kim, J. Paglione, and N. P. Butch, *Nearly ferromagnetic spin-triplet superconductivity*, Science, 365 (2019), pp. 684–687.

[57] K. Rana, H. Kotegawa, R. R. Ullah, J. S. Harvey, S. L. Bud'ko, P. C. Canfield, H. Tou, V. Taufour, and Y. Furukawa, *Magnetic fluctuations in the itinerant ferromagnet $LaCrGe_3$ studied by ^{139}La NMR*, Phys. Rev. B, 99 (2019), p. 214417.

[58] A. G. Redfield, *Nuclear magnetic resonance saturation and rotary saturation in solids*, Phys. Rev., 98 (1955), pp. 1787–1809.

[59] M. A. Ruderman and C. Kittel, *Indirect exchange coupling of nuclear magnetic moments by conduction electrons*, Phys. Rev., 96 (1954), pp. 99–102.

[60] E. R. Schemm, W. J. Gannon, C. M. Wishne, W. P. Halperin, and A. Kapitulnik, *Observation of broken time-reversal symmetry in the heavy-fermion superconductor upt¡sub¿3¡/sub¿*, Science, 345 (2014), pp. 190–193.

[61] G. Schön, *Auger and direct electron spectra in x-ray photoelectron studies of zinc, zinc oxide, gallium and gallium oxide*, Journal of Electron Spectroscopy and Related Phenomena, 2 (1973), pp. 75–86.

[62] M. P. Seah and W. A. Dench, *Quantitative electron spectroscopy of surfaces: A standard data base for electron inelastic mean free paths in solids*, Surface and Interface Analysis, 1 (1979), pp. 2–11.

[63] B. S. Shastry and E. Abrahams, *What does the korringa ratio measure?*, Phys. Rev. Lett., 72 (1994), pp. 1933–1936.

[64] P. Sherpa, R. Hingorani, A. Menon, I. Vinograd, C. Chaffey, A. P. Dioguardi, R. Yamamoto, M. Hirata, F. Ronning, J. R. Badger, P. Klavins, R. R. P. Singh, V. Taufour, and N. J. Curro, *Observation of a pronounced hebel-slichter peak in the spin-lattice relaxation rate and implications for gap and pairing symmetry in* laniga$_2$, Phys. Rev. Lett., 136 (2026), p. 186001.

[65] P. Sherpa, I. Vinograd, Y. Shi, S. A. Sreedhar, C. Chaffey, T. Kissikov, M.-C. Jung, A. S. Botana, A. P. Dioguardi, R. Yamamoto, M. Hirata, G. Conti, S. Nemsak, J. R. Badger, P. Klavins, I. Vishik, V. Taufour, and N. J. Curro, *Absence of strong magnetic fluctuations or interactions in the normal state of $LaNiGa_2$*, Phys. Rev. B, 109 (2024), p. 125113.

[66] M. Shimizu, H. Amanuma, K. Hachitani, H. Fukazawa, Y. Kohori, T. Namiki, C. Sekine, and I. Shirotani, *75as-nqr studies of superconducting filled skutterudites prru4as12 and laru4as12*, Journal of the Physical Society of Japan, 76 (2007), p. 104705.

[67] D. A. Shirley, *High-resolution x-ray photoemission spectrum of the valence bands of gold*, Phys. Rev. B, 5 (1972), pp. 4709–4714.

[68] C. P. Slichter, *Principles of Nuclear Magnetic Resonance*, Springer-Verlag, 3rd ed., 1992.

[69] B. W. Statt, *Anisotropic gap and quasiparticle-damping effects on nmr measurements of high-temperature superconductors*, Phys. Rev. B, 42 (1990), pp. 6805(R)–6808(R).

[70] V. A. Stenger, C. H. Pennington, D. R. Buffinger, and R. P. Ziebarth, *Nuclear magnetic resonance of A_3C_{60} superconductors*, Phys. Rev. Lett., 74 (1995), pp. 1649–1652.

[71] E. P. Stoll, P. F. Meier, and T. A. Claxton, *Electric field gradients from first-principles and point-ion calculations*, Phys. Rev. B, 65 (2002), p. 064532.

[72] S. Sundar, M. Yakovlev, N. Azari, M. Abedi, D. M. Broun, H. U. Ozdemir, S. R. Dunsiger, D. Zackaria, H. Bowman, P. Klavins, Y. Shi, V. Taufour, and J. E. Sonier, *Gap structure of the non-symmorphic superconductor laniga2 probed by musr*, 2024.

[73] ——, *Gap structure of the non-symmorphic superconductor laniga2 probed by musr*, 2024.

[74] H. Takahashi, S. Kitagawa, K. Ishida, M. Kawaguchi, A. Ikeda, S. Yonezawa, and Y. Maeno, *S-wave superconductivity in the dirac line-nodal material casb2*, Journal of the Physical Society of Japan, 90 (2021), p. 073702.

[75] D. Tay, T. Shang, Y. P. Qi, T. P. Ying, H. Hosono, H.-R. Ott, and T. Shiroka, *s-wave superconductivity in the noncentrosymmetric w3al2c superconductor: an nmr study*, Journal of Physics: Condensed Matter, 34 (2022), p. 194005.

[76] M. Tinkham, *Introduction to Superconductivity*, McGraw-Hill, New York, 2 ed., 1996.

[77] Y. Tokunaga, H. Sakai, S. Kambe, T. Hattori, N. Higa, G. Nakamine, S. Kitagawa, K. Ishida, A. Nakamura, Y. Shimizu, Y. Homma, D. Li, F. Honda, and D. Aoki, *125te-nmr study on a single crystal of heavy fermion superconductor ute2*, Journal of the Physical Society of Japan, 88 (2019), p. 073701.

[78] J. G. Valatin, *Comments on the theory of superconductivity*, Il Nuovo Cimento, 7 (1958), pp. 843–857.

[79] C. D. Wagner, *Chemical shifts of auger lines, and the auger parameter*, Faraday Discussions of the Chemical Society, 60 (1975), pp. 291–300.

[80] Z. F. Weng, J. L. Zhang, M. Smidman, T. Shang, J. Quintanilla, J. F. Annett, M. Nicklas, G. M. Pang, L. Jiao, W. B. Jiang, Y. Chen, F. Steglich, and H. Q. Yuan, *Two-gap superconductivity in $LaNiGa_2$ with nonunitary triplet pairing and even parity gap symmetry*, Phys. Rev. Lett., 117 (2016), p. 027001.

[81] Y. Yamada, S. Kitagawa, T. Ihara, K. Ishida, N. Uematsu, D. Hirai, and K. Takenaka, *Uniform electronic states and s-wave superconductivity in a strongly disordered high-entropy compound $X_{0.6}\mathrm{pt}_{0.4}\mathrm{Sb}$ (x = ru, rh, pd, ir)*, Phys. Rev. B, 112 (2025), p. L020508.

[82] J. Yang, J. Luo, C. Yi, Y. Shi, Y. Zhou, and G. qing Zheng, *Spin-triplet superconductivity in k¡sub¿2¡/sub¿cr¡sub¿3¡/sub¿as¡sub¿3¡/sub¿*, Science Advances, 7 (2021), p. eabl4432.

[83] K. Yosida, *Paramagnetic susceptibility in superconductors*, Phys. Rev., 110 (1958), pp. 769–770.